



**INSTITUTO POTOSINO DE INVESTIGACIÓN
CIENTÍFICA Y TECNOLÓGICA, A.C.**

POSGRADO EN NANOCIENCIAS Y MATERIALES

**Construction of 3D self-supported electrodes of
amorphous Ni(OH)₂ with rationally nanostructured
architecture for supercapacitor applications**

Tesis que presenta

Wei Ge

Para obtener el grado de

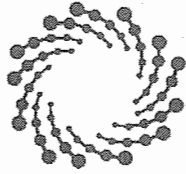
Doctor en Nanociencias y Materiales

Director (Codirectores) de la Tesis:

Dr. Armando Encinas Oropesa

Dr. Shaoxian Song

San Luis Potosí, S.L.P., 19 de Noviembre de 2019



IPICYT

Constancia de aprobación de la tesis

La tesis "***Construction of 3D self-supported electrodes of amorphous Ni(OH)₂ with rationally nanostructured architecture for supercapacitor applications***" presentada para obtener el Grado de Doctor en Nanociencias y Materiales fue elaborada por **Wei Ge** y aprobada el **diecinueve de noviembre de dos mil diecinueve** por los suscritos, designados por el Colegio de Profesores de la División de Materiales Avanzados del Instituto Potosino de Investigación Científica y Tecnológica, A.C.

Dr. Armando Encinas Oropesa
Director de la tesis

Dr. Florentino López Urias
Miembro del Comité Tutorial

Dr. Emilio Muñoz Sandoval
Miembro del Comité Tutorial

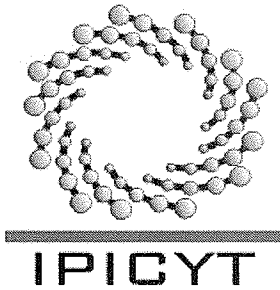
Dr. Shaoxian Song
Miembro del Comité Tutorial



Créditos Institucionales

Esta tesis fue elaborada en el Laboratorio de Nanoestructuras magnéticas de la División de Materiales Avanzados del Instituto Potosino de Investigación Científica y Tecnológica, A.C., bajo la dirección del Dr. Armando Encinas Oropesa y el Dr. Shaoxian Song.

Durante la realización del trabajo el autor recibió una beca académica del Consejo Nacional de Ciencia y Tecnología (No. 785987) y del Instituto Potosino de Investigación Científica y Tecnológica, A. C.



Instituto Potosino de Investigación Científica y Tecnológica, A.C.

Acta de Examen de Grado

El Secretario Académico del Instituto Potosino de Investigación Científica y Tecnológica, A.C., certifica que en el Acta 014 del Libro Primero de Actas de Exámenes de Grado del Programa de Doctorado en Nanociencias y Materiales está asentado lo siguiente:

En la ciudad de San Luis Potosí a los 19 días del mes de noviembre del año 2019, se reunió a las 12:00 horas en las instalaciones del Instituto Potosino de Investigación Científica y Tecnológica, A.C., el Jurado integrado por:

Dr. Florentino López Urías	Presidente	IPICYT
Dr. Emilio Muñoz Sandoval	Secretario	IPICYT
Dr. Armando Encinas Oropesa	Sinodal	IPICYT
Dra. Elsie Evelyn Araujo Palomo	Sinodal externo	ITESO

a fin de efectuar el examen, que para obtener el Grado de:

DOCTOR EN NANOCIENCIAS Y MATERIALES

sustentó el C.

Wei Ge

sobre la Tesis intitulada:

Construction of 3D self-supported electrodes of amorphous Ni(OH)₂ with rationally nanostructured architecture for supercapacitor applications

que se desarrolló bajo la dirección de

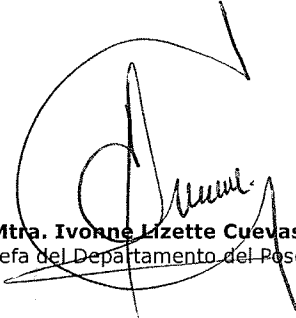
Dr. Armando Encinas Oropesa
Dr. Shaoxian Song (Wuhan University)

El Jurado, después de deliberar, determinó

APROBARLO

Dándose por terminado el acto a las 13:15 horas, procediendo a la firma del Acta los integrantes del Jurado. Dando fe el Secretario Académico del Instituto.

A petición del interesado y para los fines que al mismo convengan, se extiende el presente documento en la ciudad de San Luis Potosí, S.L.P., México, a los 19 días del mes de noviembre de 2019.


Mtra. Ivonne Lizette Cuevas Vélez
Jefa del Departamento del Posgrado


Dr. Marcial Bonilla Marín
Secretario Académico



Acknowledgements

Many thanks to the Consejo Nacional de Ciencia y Tecnología (CONACYT) of Mexico for offering me the scholarships (No. 785987) during my Ph.D study. The financial support from the National Natural Science Foundation of China (No. 51674183) is also gratefully acknowledged.

I am grateful to Dr. Carolina Martínez Sánchez, Dr. Vicente Rodríguez González and the Laboratorio de Nuevos Materiales y Catálisis Heterogénea Ambiental, IPICYT for the electrochemical tests, and also to LINAN (Laboratorio Nacional de Investigaciones en Nanociencias y Nanotecnología, IPICYT), as well as to M.C. Beatriz Adriana Rivera and M.C. Ana Iris Peña Maldonado for their technical support with the XRD and SEM, respectively. I would also like to thank the support from the lab of Dr. Florentino López Urías and Dr. Emilio Muñoz Sandoval.

I am particularly grateful to Dr. Armando Encinas and Dr. Shaoxian Song as excellent supervisors. They offered me the chance to study in IPICYT for a Ph.D degree, guided my research work, and provided financial support. I would like to express my sincere gratitude to them again.

I really appreciate our team members for providing me so much help in both life and research work. María Fernanda Ruiz Villegas, Elizabeth Alvarado Gómez, Elsie Evelyn Araujo Palomo, Daniel Esteban Camacho Martínez, Jesús Aníbal Montenegro ríos, Rosa Selene Osorio Velázquez, Jorge Alfonso Rangel Castillo, Elia Estefanía Oliva Moreno and Kevin Hintze Maldonado taught me experimental techniques and solved the problems I met in the lab. Especially, Kevin lived with me for almost two years, and thanks him very much.

I also appreciate Juan Luis Fajardo Díaz, Margarita López Medina and Fernando Hernández Navarro. I am grateful for the friendliness and hospitality that I received from them.

At last, I want to express my grate gratitude to my parents, my brother and my wife. They gave me spiritual and financial support so that I can concentrate on my studies.

Contenido

Constancia de aprobación de la tesis.....	II
Créditos Institucionales	III
Acknowledgements	V
Contenido.....	VI
Lista de figuras.....	VIII
Abstract.....	XI
Chapter I . Introduction	1
1.1 Justification	1
1.2 Hypothesis	4
1.3 Objectives	4
1.3.1 General objective	4
1.3.2 Goals.....	4
References.....	4
Chapter II. Background.....	8
2.1 Principle of supercapacitors	8
2.2 Evaluation of supercapacitor performance	10
2.3 Key factors of supercapacitors	12
2.3.1 Materials	12
2.3.2 Active material structure in electrode	13
2.3.3 Electrode structure of supercapacitors.....	14
2.3.4 Electrolytes.....	16
2.3.5 Equivalent series resistance	17
2.4 Electrode of Ni(OH) ₂ on 3D conductive scaffold.....	18
2.4.1 3D Ni(OH) ₂ electrode based on nanoporous nickel.....	18
2.4.2 3D Ni(OH) ₂ core-shell hybrid electrode	20
References.....	24
Chapter III. Experimental	29
3.1 Materials.....	29
3.2 Preparation method.....	30
3.2.1 Preparation of nanoporous and nickel nanowire arrays.	30
3.2.2 Preparation of amorphous Ni(OH) ₂ @NPN/USNWA/INWA	31
3.3 Material characterization	31
3.4 Electrochemical measurements	31
References.....	33
Chapter IV. Facile fabrication of amorphous Ni(OH) ₂ @nanoporous nickel with rational pore structure	34
4.1 Material characterization	34
4.2 Electrochemical characterization.....	41
4.3 Conclusions.....	47
References.....	47
Chapter V . Fabrication of amorphous Ni(OH) ₂ @upright self-supported nickel nanowire array with rational architecture.....	49

5.1 Material characterization	49
5.2 Electrochemical characterization.....	57
5.3 Conclusions.....	63
References.....	63
Chapter VI. Fabrication of amorphous Ni(OH) ₂ @interconnected nickel nanowire array with rational architecture	65
6.1 Material characterization	65
6.2 Electrochemical characterization.....	73
6.3 Conclusions.....	84
References.....	85
Chapter VII. Conclusions.....	88
Appendix I	89
Articles published during the Ph.D study.....	89
Appendix II	90
Experimental data of rGO.....	90

Lista de figuras

Fig. 2. 1 Schematic illustration of supercapacitor structure.	8
Fig. 2. 2 Schematics of energy-storage mechanisms for (a) EDLC, (b–c) Pseudocapacitance, (d) Battery-type behavior.	9
Fig. 3. 1 Schematic diagram of electrodeposition device.	30
Fig. 4. 1 Schematic illustration of the fabrication of Ni(OH) ₂ @NPN through a template-directed electrodeposition and surface conversion process.	34
Fig. 4. 2 Micrographs of the NC membrane: (a) Surface morphology; (b) Cross-section morphology.	35
Fig. 4. 3 SEM images of the NPN: (a) Surface morphology; (b) Cross-section morphology.	36
Fig. 4. 4 SEM and TEM images of Ni(OH) ₂ @NPN: (a) Surface morphology; (b) Cross-section morphology; (c) TEM image of Ni(OH) ₂ ; (d) HRTEM image of Ni(OH) ₂ and the corresponding SAED pattern.	38
Fig. 4. 5 (a) XRD patterns of NPN and Ni(OH) ₂ @NPN; (b) Ni 2p XPS spectrum of Ni(OH) ₂ @NPN.	40
Fig. 4. 6 (a) CV curves of Ni(OH) ₂ @NPN at different scan rates from 5 to 200 mV s ⁻¹ ; (b) Discharge curves at different current densities; (c) Specific capacitance of Ni(OH) ₂ @NPN as a function of current density; (d) Electrochemical impedance spectroscopy of Ni(OH) ₂ @NPN.	42
Fig. 4. 7 (a) Cyclic performance of Ni(OH) ₂ @NPN at a current density of 20 A g ⁻¹ ; (b) Morphology of Ni(OH) ₂ @NPN after cycle test.	45
Fig. 4. 8 Schematic illustration of the structure and advantages of Ni(OH) ₂ @NPN.	46
Fig. 5. 1 Schematic illustration of the fabrication process of Ni(OH) ₂ @USNWA.	49
Fig. 5. 2 Micrographs of PC membrane: (a) Surface morphology; (b) Cross-section morphology.	50
Fig. 5. 3 Microstructure of USNWA and Ni(OH) ₂ @USNWA: (a) Surface morphology of USNWA, (b-c) Cross-section morphology of USNWA, (d) SEM image of Ni(OH) ₂ @USNWA, (e) TEM image of Ni(OH) ₂ @USNWA, (f) HRTEM image of Ni(OH) ₂ @USNWA.	54
Fig. 5. 4 (a) Ni 2p XPS result of Ni(OH) ₂ @USNWA; (b) XRD patterns of USNWA and Ni(OH) ₂ @USNWA.	56
Fig. 5. 5 Electrochemical performance of Ni(OH) ₂ @USNWA: (a) CV curves measured at different scan rates; (b) Discharge curves at different current densities; (c) Specific capacitance as a function of current density; (d) EIS result measured in the frequency range of 10 ⁵ -10 ⁻² Hz.	59
Fig. 5. 6 (a) Cyclic performance of Ni(OH) ₂ @USNWA at a current density of 20 A g ⁻¹ ; (b) Morphology of Ni(OH) ₂ @USNWA after cycling test.	61
Fig. 5. 7 Schematic illustration of the structural advantages of Ni(OH) ₂ @USNWA.	62
Fig. 6. 1 Schematic illustration of the fabrication process of Ni(OH) ₂ @INWA through template-directed electrodeposition and surface conversion.	65

Fig. 6. 2 Micrographs of the PETE membrane: (a) Surface morphology; (b) Cross-section morphology.	66
Fig. 6. 3 SEM images of INWA: (a) Surface morphology, (b-c) Cross-section morphology. (d) SEM image of Ni(OH) ₂ @INWA; (e) TEM image of Ni(OH) ₂ @INWA; (f) HRTEM image of Ni(OH) ₂ @INWA.	70
Fig. 6. 4 (a) Ni 2p XPS spectrum of Ni(OH) ₂ @INWA; (b) XRD patterns of INWA and Ni(OH) ₂ @INWA.	71
Fig. 6. 5 Electrochemical performance of Ni(OH) ₂ @INWA. (a) CV curves at different scan rates; (b) Discharge curves at different current densities; (c) Specific capacitance as a function of discharge current density; (d) EIS result measured in the frequency range of 10 ⁵ -10 ⁻² Hz.	75
Fig. 6. 6 (a) Cyclic performance of Ni(OH) ₂ @INWA at a constant current density of 20 A g ⁻¹ ; (b-c) SEM images of Ni(OH) ₂ @INWA after cycling test.	78
Fig. 6. 7 Schematic illustration of the material and structural advantages of Ni(OH) ₂ @INWA.....	79
Fig. 6. 8 (a) CV curves of Ni(OH) ₂ @INWA and rGO electrodes. Electrochemical performance of Ni(OH) ₂ @INWA//rGO; (b) CV curves at different scan rates; (c) Discharge curves at different current densities; (d) Specific capacitance as a function of current density; (e) Ragone plot; (f) Cyclic stability at a current density of 2 A g ⁻¹ ; (g) Nyquist plot.....	83

Abreviaturas

1	NPN	Nanoporous nickel	XI
2	NC	Nitrocellulose	XI
3	USNWA	Upright self-supported nickel nanowire array	XI
4	INWA	Interconnected nickel nanowire array	XI
5	PC	Polycarbonate	XI
6	PETE	Polyester	XI
7	rGO	Reduced graphene oxide	XI
8	LIBs	Lithium-ion batteries	1
9	SCs	Supercapacitors	1
10	3D	Three-dimensional	2
11	EDLC	Electrical double-layer capacitance	9
12	CV	Cyclic voltammetry	9
13	GCD	Galvanostatic charge/discharge	9
14	ESR	Equivalent series resistance	10
15	EIS	Electrochemical impedance spectroscopy	10
16	ASCs	Asymmetric supercapacitors	16
17	LDH	Layered double hydroxide	20
18	DMF	N, N-Dimethylformamide	30

Abstract

Amorphous Ni(OH)₂ coating on nanostructured nickel scaffolds with rational architecture have been successfully fabricated by a facile process of templated-directed electrodeposition and surface oxidation treatment. Nitrocellulose membrane with interconnected fibers and fiber diameter of a few hundred nanometers was used to fabricate nanoporous nickel (NPN) at low cost. The as-prepared NPN has interconnected pore channels with pore diameter of a few hundred nanometers providing enough inner space for the formation of Ni(OH)₂ nanosheets and short pathways for fast diffusion of electrolyte ions. Upright self-supported nickel nanowire array (USNWA) and self-supported nickel nanowire array (INWA) were fabricated with porous polycarbonate template and porous polyester template, respectively. Both of USNWA and INWA can be used as miniature conductive scaffolds ensuring excellent electrical/ionic conductivity, and providing large surface area. The amorphous Ni(OH)₂ nanosheets coating on the miniature nickel scaffold was converted from the metallic surface by oxidation treatment. The conversion of metallic surface to amorphous Ni(OH)₂ nanosheets creates a stable core-shell structure, a low contact resistance and guarantees a high utilization of Ni(OH)₂. Because of the material and architecture advantages, the Ni(OH)₂@NPN/USNWA/INWA show enhanced electrochemical performance of ultrahigh specific capacities more than 3500 F g⁻¹ at a current density of 5 A g⁻¹, remarkable rate capability and excellent cycling stability. The asymmetric supercapacitor of Ni(OH)₂@INWA/rGO delivers a high energy density of 53 Wh kg⁻¹ at a power density of 395 W kg⁻¹, and an energy density of 31 Wh kg⁻¹ can be maintained at a power density of 4973 W kg⁻¹. It also shows long-term stability with 91 % retention of the initial capacitance after 10000 cycles at a current density of 2 A g⁻¹. The excellent electrochemical performance of Ni(OH)₂@NPN/USNWA/INWA makes them promising for supercapacitor applications.

Título de la tesis: Construction of 3D self-supported electrodes of amorphous Ni(OH)₂ with rationally nanostructured architecture for supercapacitor applications

Key words: Amorphous nickel hydroxide; Nanoporous nickel; Self-supported nickel nanowire array; rational architecture, Supercapacitor.

Chapter I . Introduction

1.1 Justification

Due to the increasingly global warming and seriously environmental pollutions caused by large consumption of fossil fuels, exploiting and utilizing renewable energy sources have become more and more urgent (Jacobson, 2009; Sharma, 2014). Solar, wind, tidal and geothermic energies are abundant and green energy sources. However, their discontinuities and low energy densities make efficient utilization difficult (Bhowmik et al., 2017; From, 2014). Therefore, high-performance energy storage/conversion devices are necessary to enhance the utilization efficiency of clean energy. Lithium-ion batteries (LIBs) and supercapacitors (SCs) are two main energy storage devices. Because of high energy density ($\sim 180 \text{ Wh kg}^{-1}$), LIBs have been applied as power supplies for portable devices and electric vehicles. The low power density of LIBs inhibits its widespread application where high power devices are required such as elevators, cranes and regenerative braking in electric and hybrid cars (Marom et al., 2011). Compared to LIBs, supercapacitors, also known as electrochemical capacitors, have high power density ($>10 \text{ kW kg}^{-1}$), superfast charge/discharge rate ranging from a few seconds to minutes and long cycle life ($>10^5$ cycles). Therefore, SCs have been applied in energy management, memory back-up systems, and electrical/hybrid automobile starters (Ko and Carlen, 2000; Miller, 2016; Portet et al., 2005). Current commercial SCs are mainly based on activated carbon material because of its low cost. Other carbon-based materials such as porous carbon, graphene and carbon nanotube also have been widely investigated as electrode materials (Borenstein et al., 2017; Ke and Wang, 2016). Nevertheless, the low specific capacitances of carbon materials hinder their practical applications in long endurance equipment (Borchardt et al., 2014; Candelaria et al., 2012; Inagaki et al., 2010).

Because of high specific capacitance, transitional metal-based materials (oxides/hydroxides/sulfides) have been extensively studied as supercapacitor electrode materials (Ghosh et al., 2018; Shi et al., 2014; Sk et al., 2016; Yu et al.,

2015). Among them, Ni(OH)₂ has been deemed as high-performance electrode material owing to its well-defined electrochemical redox activity, ultrahigh theoretical capacitance (~3750 F g⁻¹), low cost, abundant reserve and environmental benignity (Dong et al., 2017; Yang et al., 2008; Zhu et al., 2014). Unfortunately, the same as other transitional metal-based materials, Ni(OH)₂ suffers from low power density and unsatisfied cycling stability, which jeopardize their practical applications (González et al., 2016; Zhang et al., 2009). The former originates from its poor electrical conductivity confining fast electron transport, while the latter is related to the readily damage of the electrode fabricated by slurry-coating method, which is caused by its undesirable volume swelling during long charge/discharge process (Bakker et al., 2012; Kate et al., 2018). Moreover, the redox reactions mainly take place at the surface/near surface of Ni(OH)₂, especially at high charge/discharge rates. Therefore, the unsatisfactory rate capability and cycling stability are the two key bottlenecks that limit the practical application of Ni(OH)₂ in SCs.

To achieve excellent electrochemical performance, rich accessible electroactive-sites, short ion diffusion pathways and superior electron transfer efficiency of electrode are generally essential (Wang et al., 2019; Wu and Cao, 2018). Fabrication of nanoporous nickel (NPN) with oxidized surface and construction of Ni(OH)₂ electrodes with core-shell heterostructure on three-dimensional (3D) conductive scaffolds have been considered as promising strategies (Kang et al., 2017; Lu et al., 2013; Yan et al., 2014; Zhao et al., 2017). Ni(OH)₂ as the shell covers the core materials or nanoporous nickel. The core made of transitional metal-based materials with good electrical conductivity directly connected to the 3D conductive scaffolds provide charge transfer pathways and high surface area to load Ni(OH)₂. Both of the two strategies significantly improve the electrochemical performance of Ni(OH)₂. However, some shortcomings still exist in the two strategies, which restrict the further improvement in electrochemical performance of Ni(OH)₂.

Currently, the NPN applied in supercapacitors is prepared by dealloying method. The alloys are usually fabricated by a high energy consumption and time-consuming process, which involves melting mixed metal particles at high temperature, followed by annealing under the protection of inert gas atmosphere over ten hours (Lang et

al., 2014, 2011; Zhang et al., 2014). In addition, the appropriate pore size distribution of NPN for supercapacitor application is tens to a few hundred nanometers, which is difficult to obtain by dealloying method.

As for the 3D core-shell hybrid on conductive scaffolds, the specific capacitance of Ni(OH)₂ core-shell hybrid is still much lower than the highest value of Ni(OH)₂ that has been reported, and the rate capability is limited at high current densities, which may result from the battery-type behavior of Ni(OH)₂ and some architecture deficiencies existing in the core-shell electrode. First, the core materials coated with Ni(OH)₂ cannot participate in or fully participate in the Faradic redox reactions resulting in low utilization of the core-shell hybrid, and the diffusion-controlled redox reactions of Ni(OH)₂ lead to sluggish reaction kinetics at high current densities. Second, the core materials may not efficiently transfer charges at high current densities. Even though the core materials have better electrical conductivities than Ni(OH)₂, the electrical conductivity of the core materials is still poor due to the limited conductivity of semiconducting materials. In addition, 3D conductive scaffold is necessary for the preparation of self-supported electrode to enhance the ion/charge transfer. However, the 3D conductive scaffolds normally possess large pores, large fibers or wires (Mai et al., 2014; Shell, 2016; Yu et al., 2018). For example, 3D graphene has a large pore size distribution from a few tens to several hundred micrometers, the fiber diameters of carbon fabric are more than tens of micrometers, and nickel foam has a wire diameter of 60 micrometers and pore sizes of several hundred micrometers. The unnecessary volume and weight of current 3D conductive scaffold lead to relative low volumetric/gravimetric energy densities, making the 3D core-shell electrodes inadequate for practical applications. These deficiencies restrict the further improvement in electrochemical performance of Ni(OH)₂.

Amorphous Ni(OH)₂ has been demonstrated to be suitable for electrode material of SCs. Disordered structure and isotropy of Ni(OH)₂ result in isotropic ion diffusion pathways, which contributes to the migration of electrolyte ion in Ni(OH)₂ and the increase in ionic conductivity (Li et al., 2013; Liu et al., 2017; Su et al., 2014).

1.2 Hypothesis

Since the electrochemical performance of a supercapacitor electrode is closely related to the active material, the electrical conductivity and ionic conductivity, we hypothesize that the electrochemical performance of $\text{Ni}(\text{OH})_2$ can be further improved by using amorphous $\text{Ni}(\text{OH})_2$ as active material closely coating on nanoporous nickel with a rational pore structure or self-supported nickel nanowire arrays with rational structure.

1.3 Objectives

1.3.1 General objective

The general objective is to develop a cost-effective method to prepare nanoporous nickel with rational pore structure, and to further improve the electrochemical performance of $\text{Ni}(\text{OH})_2$ by using amorphous $\text{Ni}(\text{OH})_2$ coating on porous nickel with rational pore structure or coating on nickel nanowire arrays with rational structure.

1.3.2 Goals

- 1) To prepare nanoporous nickel with rational pore structure at low cost and self-supported nickel nanowire arrays with high wire density.
- 2) To prepare amorphous $\text{Ni}(\text{OH})_2$ coats on nanoporous nickel metal and self-supported nickel nanowires, respectively.
- 4) To investigate the structures and electrochemical performance of amorphous $\text{Ni}(\text{OH})_2$ electrode.

References

Bakker, M.G., Frazier, R.M., Burkett, S., Bara, J.E., Chopra, N., Spear, S., Pan, S., Xu, C., 2012. Perspectives on supercapacitors, pseudocapacitors and batteries. *Nanomater. Energy* 1, 136–158.

- Bhowmik, C., Bhowmik, S., Ray, A., Pandey, K.M., 2017. Optimal green energy planning for sustainable development: A review. *Renew. Sustain. Energy Rev.* 71, 796–813.
- Borchardt, L., Oschatz, M., Kaskel, S., 2014. Tailoring porosity in carbon materials for supercapacitor applications. *Mater. Horizons* 1, 157–168.
- Borenstein, A., Hanna, O., Attias, R., Luski, S., 2017. Carbon-based composite materials for supercapacitor electrodes: a review. *J. Mater. Chem. A* 5, 12653–12672.
- Candelaria, S.L., Shao, Y., Zhou, W., Li, X., Xiao, J., Zhang, J.G., Wang, Y., Liu, J., Li, J., Cao, G., 2012. Nanostructured carbon for energy storage and conversion. *Nano Energy* 1, 195–220.
- Dong, B., Li, M., Chen, S., Ding, D., Wei, W., Gao, G., Ding, S., 2017. Formation of g-C₃N₄@Ni(OH)₂ Honeycomb Nanostructure and Asymmetric Supercapacitor with High Energy and Power Density. *ACS Appl. Mater. Interfaces* 9, 17890–17896.
- From, C., 2014. Powering Mobile Networks With Green Energy. *EEE Wirel. Commun.* 90–96.
- Ghosh, S., Jeong, S.M., Polaki, S.R., 2018. A review on metal nitrides/oxynitrides as an emerging supercapacitor electrode beyond oxide. *Korean J. Chem. Eng.* 35, 1389–1408.
- González, A., Goikolea, E., Barrena, J.A., Mysyk, R., 2016. Review on supercapacitors: Technologies and materials. *Renew. Sustain. Energy Rev.* 58, 1189–1206.
- Inagaki, M., Konno, H., Tanaike, O., 2010. Carbon materials for electrochemical capacitors. *J. Power Sources* 195, 7880–7903.
- Jacobson, M.Z., 2009. Review of solutions to global warming, air pollution, and energy security. *Energy Environ. Sci.* 2, 148–173.
- Kang, J., Zhang, S., Zhang, Z., 2017. Three-Dimensional Binder-Free Nanoarchitectures for Advanced Pseudocapacitors 1700515, 1–12.
- Kate, R.S., Khalate, S.A., Deokate, R.J., 2018. Overview of nanostructured metal oxides and pure nickel oxide (NiO) electrodes for supercapacitors: A review. *J. Alloys Compd.* 734, 89–111.
- Ke, Q., Wang, J., 2016. Graphene-based materials for supercapacitor electrodes-A review. *J Mater.* 2, 37–54.
- Ko, R., Carlen, M., 2000. Principles and Applications of Electrochemical Capacitors. *Electrochim. Acta* 45, 2493–2498.
- Lang, X., Hirata, A., Fujita, T., Chen, M., 2014. Three-dimensional hierarchical nanoporosity for ultrahigh power and excellent cyclability of electrochemical pseudocapacitors. *Adv. Energy Mater.* 4, 2–7.

- Lang, X., Hirata, A., Fujita, T., Chen, M., 2011. Nanoporous metal/oxide hybrid electrodes for electrochemical supercapacitors. *Nat. Nanotechnol.* 6, 232–236.
- Li, H.B., Yu, M.H., Wang, F.X., Liu, P., Liang, Y., Xiao, J., Wang, C.X., Tong, Y.X., Yang, G.W., 2013. Amorphous nickel hydroxide nanospheres with ultrahigh capacitance and energy density as electrochemical pseudocapacitor materials. *Nat. Commun.* 4, 1894.
- Liu, S., Lee, S.C., Patil, U., Shackery, I., Kang, S., Zhang, K., Park, J.H., Chung, K.Y., Chan Jun, S., 2017. Hierarchical MnCo-layered double hydroxides@Ni(OH)₂ core-shell heterostructures as advanced electrodes for supercapacitors. *J. Mater. Chem. A* 5, 1043–1049.
- Lu, Q., Chen, J.G., Xiao, J.Q., 2013. Nanostructured electrodes for high-performance pseudocapacitors. *Angew. Chemie - Int. Ed.* 52, 1882–1889.
- Mai, L., Tian, X., Xu, X., Chang, L., Xu, L., 2014. Nanowire Electrodes for Electrochemical Energy Storage Devices. *Chem. Rev.* 114, 11828–11862.
- Marom, R., Amalraj, S.F., Leifer, N., Jacob, D., Aurbach, D., 2011. A review of advanced and practical lithium battery materials. *J. Mater. Chem.* 21, 9938–9954.
- Miller, J.R., 2016. Engineering electrochemical capacitor applications. *J. Power Sources* 326, 726–735.
- Portet, C., Taberna, P.L., Simon, P., Flahaut, E., Laberty-Robert, C., 2005. High power density electrodes for Carbon supercapacitor applications. *Electrochim. Acta* 50, 4174–4181.
- Sharma, A., 2014. Environmental Pollution and Global Warming. *Int. J. Interdiscip. Multidiscip. Stud.* 1, 88–96.
- Shell, H.O.C., 2016. High-Performance One-Body Core/Shell Nanowire Supercapacitor Enabled by Conformal Growth of Capacitive 2D WS₂ Layers. *ACS Nano* 10, 10726–10735.
- Shi, F., Li, L., Wang, X.L., Gu, C.D., Tu, J.P., 2014. Metal oxide/hydroxide-based materials for supercapacitors. *RSC Adv.* 4, 41910–41921.
- Sk, M., Yue, C.Y., Ghosh, K., Jena, R.K., 2016. Review on advances in porous nanostructured nickel oxides and their composite electrodes for high-performance supercapacitors. *J. Power Sources* 308, 121–140.
- Su, Y.Z., Xiao, K., Li, N., Liu, Z.Q., Qiao, S.Z., 2014. Amorphous Ni(OH)₂@three-dimensional Ni core-shell nanostructures for high capacitance pseudocapacitors and asymmetric supercapacitors. *J. Mater. Chem. A* 2, 13845–13853.
- Wang, T., Chen, H.C., Yu, F., Zhao, X.S., Wang, H., 2019. Boosting the cycling stability of transition metal compounds-based supercapacitors. *Energy Storage Mater.* 16, 545–573.
- Wu, Y., Cao, C., 2018. The way to improve the energy density of supercapacitors: Progress and perspective. *Sci. China Mater.* 1–10.

- Yan, J., Wang, Q., Wei, T., Fan, Z., 2014. Recent advances in design and fabrication of electrochemical supercapacitors with high energy densities. *Adv. Energy Mater.* 4.
- Yang, G.W., Xu, C.L., Li, H.L., 2008. Electrodeposited nickel hydroxide on nickel foam with ultrahigh capacitance. *Chem. Commun.* 2, 6537–6539.
- Yu, K., Pan, X., Zhang, G., Liao, X., Zhou, X., Yan, M., Xu, L., Mai, L., 2018. Nanowires in Energy Storage Devices: Structures, Synthesis, and Applications. *Adv. Energy Mater.* 1802369-1802388.
- Yu, Z., Tetard, L., Zhai, L., Thomas, J., 2015. Supercapacitor electrode materials: Nanostructures from 0 to 3 dimensions. *Energy Environ. Sci.* 8, 702–730.
- Zhang, J., Zhan, Y., Bian, H., Li, Z., Tsang, C.K., Lee, C., Cheng, H., Shu, S., Li, Y.Y., Lu, J., 2014. Electrochemical dealloying using pulsed voltage waveforms and its application for supercapacitor electrodes. *J. Power Sources* 257, 374–379.
- Zhang, Y., Feng, H., Wu, X., Wang, L., Zhang, A., Xia, T., Dong, H., Li, X., Zhang, L., 2009. Progress of electrochemical capacitor electrode materials: A review. *Int. J. Hydrogen Energy* 34, 4889–4899.
- Zhao, H., Liu, L., Vellacheri, R., Lei, Y., 2017. Recent Advances in Designing and Fabricating Self-Supported Nanoelectrodes for Supercapacitors. *Adv. Sci.* 4.
- Zhu, Y., Cao, C., Tao, S., Chu, W., Wu, Z., Li, Y., 2014. Ultrathin Nickel Hydroxide and Oxide Nanosheets: Synthesis, Characterizations and Excellent Supercapacitor Performances. *Sci. Rep.* 4, 1–7.

Chapter II. Background

2.1 Principle of supercapacitors

A typical supercapacitor consists of three essential components : a pair of working electrodes composed of active materials embedded in current collectors, electrolyte, and separator as shown in Fig. 2.1. The positive electrode and negative electrode are soaked in an electrolyte and separated by a porous and insulating separator that prevents the direct flow of electrons between the two electrodes and facilitates the ion diffusion. In the charge/discharge process, electrons flow out of one electrode into the other electrode through the external circuit, and at the same time, counter ions travel from one electrode or its vicinity into the other electrode.

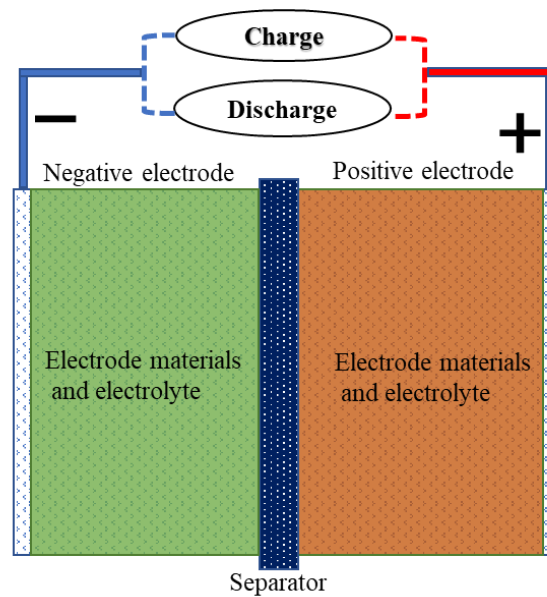


Fig. 2. 1 Schematic illustration of supercapacitor structure.

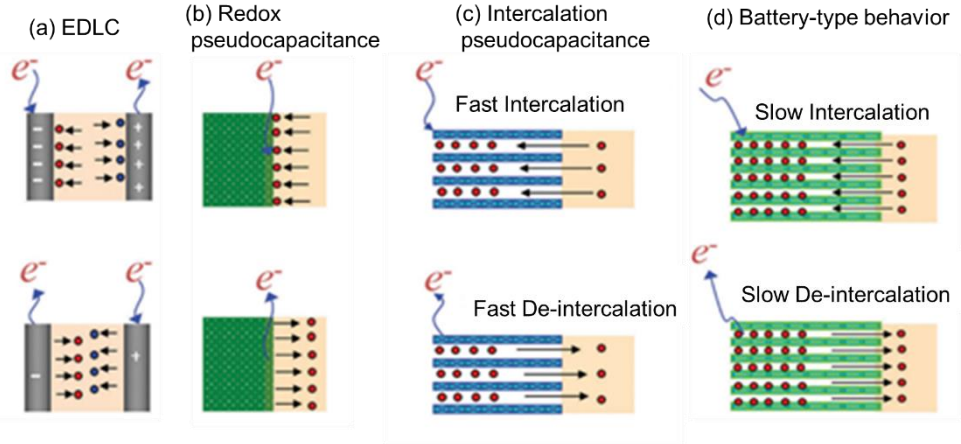


Fig. 2. 2 Schematics of energy-storage mechanisms for (a) EDLC, (b–c) Pseudocapacitance, (d) Battery-type behavior (Wang et al., 2016).

The energy storage mechanisms of the supercapacitor electrode materials are normally identified as electrical double-layer capacitance (EDLC), pseudo-capacitance and battery-type behavior (Shao et al., 2018; Wang et al., 2016). Carbonaceous materials normally store energy through EDLC, which arises from the accumulation of electrostatic charges at the electrode/electrolyte interface in the electrical-double layer, as shown in Fig. 2.2(a). The capacitance mainly depends on accessible surface area of the active materials in the electrode. The adsorption/desorption of electrolyte ions at the interface are purely physical processes, and there is no charge transfer between the interface.

In contrast to EDLC, Pseudo-capacitance is based on fast Faradic redox reactions at the surface or near surface of the active materials, resulting in high charge storage capacity. It is normally classified into two types: pseudo-capacitance controlled by reversible surface redox reaction and pseudo-capacitance dominated by intercalation (Fig. 2.2 (b-c)) (Augustyn et al., 2014). The former normally stores charges through adsorption of electrolyte cations and anions on the surface of active material. Therefore, the faradaic redox reactions occur only on the active material surface. Materials such as RuO_2 , MnO_2 , Mn_3O_4 and FeOOH , have surface redox pseudo-capacitance, and display similar cyclic voltammetry (CV) and galvanostatic charge/discharge (GCD) curves as that of EDLC based materials (Wang et al., 2016). The capacitance arises from intercalation process involving reversible

intercalation/de-intercalation of electrolyte cations (Na⁺, K⁺, Li⁺, H⁺, etc.) into the crystal structure of active materials (Wang et al., 2016). The common materials storing energy with this mechanism are sulphides and oxides of V, W, Mo and Ti. It is worth noting that no material phase change occurs in these materials. However, some intercalation process show battery-type behaviors (Fig. 2(d)), which has phase-transformation and/or alloying reactions besides the intercalation reaction during the charge/discharge process (Wang et al., 2016). The redox reactions of metal ions within the crystalline structure of active materials are controlled by the intercalation/de-intercalation of cations (H⁺ or Li⁺) within the crystalline structure. The CV plot shows pronounced oxidation and reduction peaks, and the GCD plot shows oxidation and reduction plateaus regions. Ni, Co, Cu and Cd based oxides, hydroxides, sulfides, selenides and phosphides are battery-type materials.

2.2 Evaluation of supercapacitor performance

The performance of SCs is mainly evaluated by energy density, power density and cycling stability. Energy density (E , Wh kg⁻¹) determines how much energy can be stored; and power density (P , kW kg⁻¹) assesses how fast the stored energy can be released. In a supercapacitor, E and P can be calculated according to the following equations (Raza et al., 2018):

$$E = \frac{CV^2}{2 \times 3.6} \quad (2-1)$$

$$P = \frac{3.6E}{\Delta t} \quad (2-2)$$

$$P_{max} = \frac{V^2}{4ESR} \quad (2-3)$$

where C (F g⁻¹) is the specific capacitance, V (V) is operational voltage window of the cell excluding the IR voltage, Δt (s) is the discharge time, P_{max} (kW kg⁻¹) is the maximum power density, respectively, and ESR (Ω) is the equivalent series resistance.

Cyclic voltammetry (CV), galvanostatic charge/discharge (GCD) test, and electrochemical impedance spectroscopy (EIS) are the mostly common used techniques to characterize the electrochemical performance of a single electrode or

a full device (Zhang and Pan, 2015). For a single electrode, the electrochemical performances are investigated using a three-electrode system containing working electrode, reference electrode and counter electrode. The specific capacitance characterizes the charge-storage capability of active materials within a specific voltage, and can be calculated from the results of CV and GCD measurements, respectively. The equations are as follows (Faraji and Ani, 2015):

$$C = \frac{\int_{V_i}^{V_f} I(V) dV}{mv(V_f - V_i)} \quad (2-4)$$

where C ($F\ g^{-1}$) is the specific capacitance, m (g) is the mass of the active material in the electrode, v ($V\ s^{-1}$) is the scan rate of CV curves, and $V_f - V_i$ (V) is the potential window.

$$C = \frac{I\Delta t}{m\Delta V} \quad (2-5)$$

where I (A) is the discharge current, Δt (t) is the discharge time, m (g) is the mass of active materials, and ΔV is the voltage drop upon discharging excluding the IR voltage drop caused by the internal resistance. Because the GCD measurement is more closely to reflect the real working behavior of a working supercapacitor. Thus, the GCD measurement is the mostly used to calculate the specific capacitance.

For a supercapacitor device, the electrochemical performance are tested using a two-electrode system. The specific capacitance of SCs can also be calculated according to equations (2-5). But the m is the total mass of the active materials in both electrodes. The obtained specific capacitance can be applied to calculate energy density according Equation (1). In order to achieve optimal performance, there should be a charge balance ($Q^+ = Q^-$) between the positive and the negative electrodes (Shao et al., 2018). The specific capacitance, the active mass (m) and the potential window of each electrode (ΔV) determine the total stored charges in each electrode. Herein, the specific capacitance is measured and calculated using three-electrode system. The stored charges can be obtained by $Q = Cm\Delta V$, from which the mass ratio of m_+/m_- can be calculated.

The ESR of an electrode is evaluated by EIS test that show a Nyquist plot, which exhibits a semicircle at the high-frequency range and a sloping line at the low-frequency range. The point of intersection on the real axis in the high-frequency range represents the internal resistance (R_s), which contains the intrinsic electronic resistance of the electrode material, the ohmic resistance of the electrolyte, and the interfacial resistance between the electrode material and current collector. The semicircle at lower frequencies represents the charge-transfer resistance (R_{ct}). At low frequency, the inclined long line represents the mass capacitance and the inclined angle suggests the diffusion resistance of the electrolyte ions.

2.3 Key factors of supercapacitors

The energy and power densities of a supercapacitor are influenced by the specific capacitance, operating voltage window and ESR. These parameters are determined by the electrode materials, electrode structure and electrolytes used in SCs (T. Wang et al., 2019).

2.3.1 Materials

Carbonaceous materials and transitional metal-based materials are the two main kinds of electrode materials for SCs (Yu and Chen, 2016). Because of different material properties, their electrochemical performance vary greatly. Carbonaceous materials such as graphene, nanotube, porous carbon and active carbon, store energy through ion adsorption in the electronic double layers formed at the electrode-electrolyte interface, which is a non-faradic process with no charge transfer across the interface (Chen and Dai, 2013). Due to good electrical conductivity, carbonaceous materials have excellent rate capability. The carbonaceous materials also exhibit long cycle life, which can be attributed to a few factors (Yan et al., 2012). One of the most important factor is their chemical stability in electrolyte. The other is due to the nature of energy storage mechanism of carbon materials. The physical charge transfer process makes the charge storage highly reversible and no volume change of the materials, which results in excellent cycling stability. However, because of the low specific capacitance (normally $< 200 \text{ F g}^{-1}$)

and low operating-potential range (≤ 1.0 V), the SCs of carbon materials have low energy densities (<10 Wh kg^{-1}) (Borenstein et al., 2017).

Transitional metal-based materials store energy through reversible redox reactions between the active species and the electrolyte (Cheng et al., 2014). Therefore, their specific capacitances are much higher than carbon materials. Unfortunately, transitional metal-based materials usually suffer from low power density and poor cycling stability, which seriously restrict their practical applications. The poor electrical conductivity of transitional metal-based materials confines the fast electron transport within itself, resulting in a low power density. The poor cycling stability can be attributed to the fragile crystal structure and poor electrical conductivity. The buildup of charge on the surface of transitional metal-based materials produces electrostatic stresses and leads to the volume expansion/collapse, resulting in rapid capacitance fading during the charge/discharge process. The dissolution of transition metal-based materials in the electrolyte solution further reduces their cycling stability.

2.3.2 Active material structure in electrode

The energy density of SCs depends on the specific capacitance of the electrode, and the specific capacitance is strongly dependent on the accessible surface area of the active materials (Yan et al., 2014). Porous carbon materials with high specific surface area have been prepared as electrode materials. Moreover, many approaches have been developed to further increase the specific capacitance by increasing the surface area, including heat treatment, alkaline treatment, physical or chemical activation, and plasma surface treatment (Chen et al., 2013). Besides the specific surface area, pore size distribution is another important factor that affects the specific capacitance. Larger pore size can significantly reduce the specific surface area, and smaller pore size can increase the specific surface area. However, it has been demonstrated that micropores with diameter of less than 0.4 nm are too small to form the electrical double-layer. Thus, both larger and smaller pores can lead to a drop in the specific capacitance.

As for transitional metal-based materials, the specific surface area is determined by its particle size and morphology. Nanosized electroactive materials with porous morphology can provide increased specific surface area for faradic reactions. Thereby porous transitional metal-based materials such as coral-like shapes, flowerlike microspheres, mesoporous nanowires and nanobundles have been synthesized for SCs applications (Cheng et al., 2014). The composite of carbon material and transitional metal-based material can achieve improved electrochemical performance. Carbon materials such as mesoporous carbon, carbon fibers, carbon foam, CNTs and graphene are used as substrates to load transitional metal materials, which can improve the electrical conductivity and increase the utilization (Zhang et al., 2009).

Besides, the porous structure of active material provides short diffusion and transport pathways for fast ion diffusion/transportation within the particles, facilitating the transport of electrolyte ions, accordingly improving the electrochemical utilization of active materials and high rate capability (Bakker et al., 2011).

2.3.3 Electrode structure of supercapacitors

1) Single electrode structure

The electrode structure determines the mass and surface area of active material, electrical conductivity and the diffusion of electrolyte ions, which have influence on the overall electrochemical performance. Nanostructured particles of active materials with porous structure have large electroactive surface area to store energy. In general, these nanoparticles need to be mixed with conductive additive and polymer binder to make a paste, and then pressed into a current collector for practical application. This kind of slurry-coating electrode has several drawbacks (Cao et al., 2015). The aggregation of the particles results in dead surface and prevents the diffusion of electrolyte ions onto the active material surface, reducing the specific capacitance and rate capability. Because the carbonaceous material as conductive substrate is non-continuous, the electrical conductivity is still limited. The polymer binder and additive drastically decrease both the volumetric and gravimetric capacitance of the electrode. Moreover, the polymer binder is insulating, and greatly

increases the internal resistance hindering the fast charge transportation. When the active material contains transitional metal-based material, the volume swelling of transitional metal-based material during the charge-discharge process can destroy the electrode structure and causes capacitance degradation.

Fabrication of binder-free electrode is an effective strategy to obtain high utilization of active materials, low internal resistance and short pathways for electrolyte ion diffusion (Kang et al., 2017; Yu et al., 2018). The nanostructured active material direct grow on a 3D conductive scaffold without using conductive additives and polymer binders. 3D conductive scaffold has large surface area to load active materials, and porous channels for fast diffusion of electrolyte ions, and can avoid the structure destroy caused by volume change. Nickel foam, 3D graphene, carbon cloth and porous metal are the common used 3D conductive scaffolds (Kang et al., 2017). Nanosheets/nanowires with core-shell structure on 3D conductive scaffolds can achieve enlarged surface area of active material without decreasing the utilization and electrical conductivity. Transitional metal-based materials with better electrical conductivity than the shell materials are used as core materials. The core material in the form of nanosheet/nanowire directly loads the shell materials and connects to the 3D conductive scaffold providing charge transfer pathways for the shell materials. This kind of electrode significantly reduces the internal resistance and improves the power density.

2) Structure of electrode pairs

Since energy density of a supercapacitor is proportional to the square of the operating voltage, the energy density can be increased by achieved by enlarging the operating voltage which can be realized by selecting a proper pair of electrode. Symmetric capacitor utilizes a pair of the same electrodes, such as electrical double layer capacitor and pseudocapacitor (Ke and Wang, 2016). The electrodes of electrical double layer capacitor are made of carbonaceous materials, and pseudocapacitor contains two electrodes made of transitional metal-based materials. Symmetric supercapacitor has narrow operating voltage. Asymmetric supercapacitors (ASCs) can extend the operating voltage by reasonable combining

two dissimilar electrodes with different potential windows (Wu and Cao, 2018). Capacitive materials such as graphene, carbon nanotube and activated carbon are used to prepare negative electrode. Pseudocapacitive materials such as RuO₂, MnO₂, and Ni(OH)₂ are used to prepare positive electrode. This asymmetric configuration makes full use of the different operating voltages of the two different electrodes and enlarge the potential window higher than 1.5 V, which significantly increase the energy density.

2.3.4 Electrolytes

Electrolyte is also a key factor determining the operating voltage of SCs. It also affects the rate capability and cycling performance. The electrolytes used in SCs can be classified into three types: aqueous electrolyte, organic electrolyte and ionic liquid electrolyte (Wang et al., 2016).

1) Aqueous electrolyte

There are three kinds of aqueous electrolytes: acid electrolyte (H₂SO₄), alkali electrolyte (KOH, NaOH), and neutral electrolyte (Na₂SO₄). They usually have high ionic conductivity (up to ~1 S cm⁻¹), low cost, ease of handling, and nonflammability. Transitional metal-based materials are usually employed in aqueous electrolyte. Due to their better electronic conductivity, higher dielectric constant, and smaller ionic radius, supercapacitors with aqueous electrolytes display higher capacitances and power densities than those with the same electrodes in organic electrolyte. However, for symmetrical SCs using aqueous solution, the accessible voltage cannot exceed 1.23 V, which is restricted by the electrolytic decomposition of water. The concentration of electrolyte ions also have effect on the performance of SCs. The Warburg resistance, the charge transfer resistance and the ESR decrease with increasing concentration of electrolyte ions.

2) Organic electrolyte

The advantage of an organic electrolyte is the higher attainable voltage (2.5~3.0 V) with electric double layer capacitive electrode materials. The most widely used solvents are acetonitrile and propylene carbonate. The salts used in organic

electrolyte are tetraethylammonium, tetrafluoroborate, tetraethylphosphonium, tetrafluoroborate, triethylmethylammonium, and tetrafluoroborate. However, the organic electrolytes usually are more expensive, flammable, toxic and less conductive than aqueous electrolytes. The poor ionic conductivity results in high ESR and leads to a reduced rate capability.

3) Ionic electrolyte

Ionic liquid electrolytes are defined as salts with melting points below 100°C. They consist of an organic ion and an inorganic counter-ion, or of two organic ions. Because of no water contained, they have larger operating voltages than aqueous electrolytes and higher ion concentrations than organic solvents. The electrochemical potential can reach the range from 2 to 6 V, typically 4.5 V. The main drawback of ionic liquid electrolyte is their low electrical conductivity, which is typically less than 10 mS cm⁻¹, and is at least one order of magnitude lower than that of aqueous electrolytes. Thus, the capacitance of a supercapacitor using ionic liquid electrolyte usually has low specific capacitance and exhibits relatively poor power density. Meanwhile, ionic liquid electrolyte often has prohibitive cost and require stringent conditions for drying carbon material to ensure water-free environment in the cell.

2.3.5 Equivalent series resistance

ESR has great influence on the power and energy densities of SCs. It contains a number of resistances: the intrinsic resistance of the electroactive materials and the current collector, the contact resistance between the electroactive materials and the current collector, the ion diffusion resistance of ions in the electrode material and through the separator, and the electrolyte ionic resistance (Shao et al., 2018). Therefore, ESR is determined by the electrode material, electrode structure and electrolyte. There are two methods for determining ESR (Zhang and Pan, 2015): (1) Measure the *IR* drop at the initiation of a constant current discharge curve and (2) EIS measurement.

2.4 Electrode of Ni(OH)₂ on 3D conductive scaffold

Ni(OH)₂ is a promising candidate as electrode material for supercapacitor applications, because of its low cost, abundant reserve and high theoretical specific capacitance (Dong et al., 2017; Yang et al., 2008). However, due to its poor electrical conductivity, it has poor cyclic stability and poor density, which jeopardize its practical applications (B. Li et al., 2016). To achieve high electrochemical performance, an attractive method is to grow nanostructured Ni(OH)₂ on 3D conductive scaffolds without using polymer binder and conductive additive (Kang et al., 2017; Pourjavadi et al., 2018). The Ni(OH)₂ on 3D conductive scaffolds showed significant improved electrochemical performance, due to the structure advantages of good electrical conductivity and short pathways for the diffusion of electrolyte ions. The common used 3D conductive scaffolds are nickel foam, carbon cloth, 3D graphene and nanoporous metal. They have large surface area, high porosity, good electric conductivity, and excellent chemical stability in a wide variety of liquid electrolytes.

2.4.1 3D Ni(OH)₂ electrode based on nanoporous nickel

Due to the excellent electrical conductivity, large surface area and abundant channels, nanoporous metal is a kind of excellent 3D conductive scaffold (Jia et al., 2007). 3D nanoporous metal scaffold not only acts as a current collector for efficient charge transfer, but also provides a large surface area for the deposition of active materials, enabling good conductivity and making the conductive additive and binder completely unnecessary. Meanwhile, the bicontinuous channels allow the rapid ion diffusion. Nanoporous gold, nanoporous nickel (NPN) and nanoporous copper fabricated by dealloying method have been widely studied as 3D conductive backbones for pseudocapacitor applications (Kang et al., 2017). Au and Ag are valuable metals, and metallic copper is not stable in electrolyte. Due to the low-cost and chemical stability, NPN is the most promising candidate for supercapacitor applications.

NPN with oxidized surface is expected to achieve high specific capacitance, rate capability and long cycle life. The NPN with pore size less than 10 nm fabricated by dealloying Ni₃₀Mn₇₀ showed high rate performance and excellent cycling stability (Qiu et al., 2014b). However, due to the small pore size and limited porosity, the NPN electrode only exhibited an areal capacitance of 1.7 F cm⁻². In order to increase the areal capacitance by improving the pore structure, a Mn₇₀Cu₁₅Ni₁₅ alloy was used to fabricate NPN with hierarchical pore structure in the range of several to a few hundred nanometers by two-step dealloying process: Mn dealloying, high temperature annealing, and Cu dealloying (Qiu et al., 2014a). However, the as-prepared NPN with an average pore size of 250 nm showed a reduced areal capacitance of 1.11 F cm⁻². It should be noted that even though the average pore size is only 250 nm, the fusion of small pores during high temperature annealing resulted in the formation of a great quantity of large pores with diameter more than 1 μm, which seriously decreased the specific surface area. The NPN fabricated from Ni₁₅Al₈₅ alloy with pore size in the range of several to a few hundred nanometers exhibited a high areal capacitance of 4.76 F cm⁻² (Qiu et al., 2015). Therefore, the appropriate pore size of porous Ni for supercapacitor application is a few hundred nanometers, which not only can provide enough inner space for the formation of porously active materials, but also can facilitate the fast diffusion of electrolyte ions at high current densities. However, it is difficult to control pore structure of porous Ni fabricated by dealloying process. In addition, so far the alloys used to fabricate NPN are usually prepared by a high-energy consumption and time-consuming process, which involves melting mixed metal particles at high temperature, followed by annealing under the protection of inert gas atmosphere over ten hours (Jia et al., 2007). The chemical/electrochemical dealloying process to produce nanoporous also takes a long time. Therefore, the fabrication cost of NPN is too high for commercial-scale production. Therefore, it is meaningful to develop a cost-effective method for fabricating NPN with rational pore structure for supercapacitor applications.

2.4.2 3D Ni(OH)₂ core-shell hybrid electrode

The direct growth of nanostructured Ni(OH)₂ on a 3D conductive scaffold can overcome the drawbacks of slurry-coating method. However, the mass of Ni(OH)₂ on the conductive scaffold is low, resulting in a low energy density. Construction core-shell Ni(OH)₂ nanosheet/nanowire array on the 3D conductive scaffold is an effective strategy to increase the loading mass (Jiang et al., 2016; Liu et al., 2011). The core-shell nanowires/nanosheets are well separated and electrically connected to the conductive scaffold. The core material loading the shell material is immobilized to the scaffold providing electronic pathways for efficient charge transport. The space between the nanowires/nanosheets offers short ion transport pathways resulting in high rate performance, and accommodates the volume change avoiding the damage of electrode structure. The transitional metal-based materials with better electrical conductivity than Ni(OH)₂ are used as core materials directly grown on conductive scaffold.

Co(OH)₂ delivers better electrochemical performance than Ni(OH)₂, indicating that Co(OH)₂ can serve as a good core material to construct Ni(OH)₂@Co(OH)₂ hybrid electrode (Y. Wang et al., 2019). Ni(OH)₂@Co(OH)₂ core-shell nanosheets have been successfully grown on nickel foam as 3D self-supported electrode for electrochemical capacitors via an electrodeposition process. The 3D conductive framework combined with the unique core-shell heterostructure endows the Ni(OH)₂@Co(OH)₂ hybrid electrode good electrochemical performances. It exhibited a capacitance of 1520.6 F g⁻¹ at a current density of 1 A g⁻¹ and still kept 1376.6 F g⁻¹ at a current density of 10 A g⁻¹, exhibiting excellent rate performance. Moreover, after 1500 charge/discharge cycles at a current density of 5 A g⁻¹, the capacitance retained ~71.4 %, demonstrating good cycling stability.

Complex hydroxides exhibit richer redox reactions and higher electronic conductivities than their corresponding mono-component hydroxides. CoAl layered double hydroxide (CoAl-LDH), MnCo-LDH and NiCo-LDH have been used as core materials (Hong et al., 2014; Liang et al., 2018; Liu et al., 2017). The heterostructure with Ni(OH)₂ nanosheets as shell and NiCo-LDH nanowire as core on carbon fiber

cloth was successfully fabricated by two step hydrothermal processes (Liang et al., 2018). The resultant Ni(OH)₂@NiCo-LDH exhibited a high specific capacitance of about 2622 F g⁻¹ at a current density of 1 A g⁻¹ and good cycling stability (88.5 % remain after 10000 cycles). The enhanced electrochemical performance is benefit from the synergistic effect of the core-shell structure supplying more electrochemical active sites for redox reactions, and pathways to accelerate electron and ion transport. Furthermore, the asymmetric supercapacitor of Ni(OH)₂@NiCo-LDH//AC device displayed a high energy density of 51.7 Wh kg⁻¹ at a power density of 599 W kg⁻¹ and presented a satisfying cycling performance.

Because of good electric conductivity, high chemical stability and mechanical flexibility, ZnO can be utilized as conducting pathways for electrons and as supports for attachment of the transitional metal oxides/hydroxides. ZnO with various morphologies has been used to fabricate hybrid electrodes for SCs such as MnO₂@ZnO (Radhamani et al., 2016), NiO@ZnO (Ouyang et al., 2018), and Co₃O₄@ZnO (Cai et al., 2014). Due to the synergistic effect between two individual components, enhanced electrochemical performance have been achieved. Ni(OH)₂@ZnO on Ni foam exhibited a high specific capacitance of 2028 F g⁻¹ at a current density of 10 A g⁻¹ with good cycling stability (Niu et al., 2015). Meanwhile, the array also showed a high specific capacitance of 1059 F g⁻¹ even at an extremely high current density of 100 A g⁻¹, indicating a superb rate capability.

Cobalt oxide is also an excellent core material. The Ni(OH)₂@Co₃O₄ nanosheets grown on nickel foam substrate showed enhanced electrochemical properties (Bai et al., 2017). Ni(OH)₂ anchored on Co₃O₄ nanosheets effectively facilitated the ion diffusion and increased the active surface. The Ni(OH)₂@Co₃O₄ displayed a high specific capacitance of 1306 F g⁻¹, high charge/discharge rate and excellent cycling stability. Furthermore, the solid-state asymmetric supercapacitor of Co₃O₄@Ni(OH)₂//AC exhibited a high energy density of 40 Wh kg⁻¹, high power density of 3455 W kg⁻¹ as well as good cycling stability (90.5 % capacitance retention after 5000 cycles). Microporous hydrogenated CoO_x (H-CoO_x) nanowires has good electrical conductivity (Zhu et al., 2014). Benefiting from the synergistic effects of the core-shell heterostructure, the Ni(OH)₂@H-CoO_x nanowire achieved a specific

capacitance of 2196 F g^{-1} , which is approximately 1.4 times higher than the $\text{Ni(OH)}_2@ \text{Co}_3\text{O}_4$ core-shell nanowires. The ASC device of $\text{Ni(OH)}_2@ \text{H-CoOx//Fe}_3\text{O}_4@ \text{rGO}$ nanocomposite achieved high energy densities of 45.3, 23.4 Wh kg^{-1} at power densities of 1010 and 7080 W kg^{-1} respectively, and high cycling stability.

As the electrical conductivity and electrochemical activity of multi-metal oxide are higher than that of the monometal oxide/hydroxide, ZnCo_2O_4 (Pan et al., 2017), NiCo_2O_4 (Yin et al., 2016), MnCo_2O_4 (Zhao et al., 2016) are suitable as skeletons to support Ni(OH)_2 . The hierarchical $\text{Ni(OH)}_2@ \text{ZnCo}_2\text{O}_4$ sheet composite on nickel foam showed an ultrahigh areal capacitance of 4.6 F cm^{-2} at a current density of 2 mA cm^{-2} (Pan et al., 2017). The ASC device of $\text{Ni(OH)}_2@ \text{ZnCo}_2\text{O}_4// \text{carbonized fiber paper}$ achieved a high energy density of 49 Wh kg^{-1} at a power density of 428 W kg^{-1} . The binder-free hybrid composite electrode with nanoarchitecture $\text{Ni(OH)}_2@ \text{NiCo}_2\text{O}_4$ directly grown on carbon fiber paper demonstrated a high areal capacitance of 5.2 F cm^{-2} at a current density of 2 mA cm^{-2} , with a capacitance retention of 79 % as the current density increased from 2 to 50 mA cm^{-2} (Huang et al., 2013). However, because of the lower conductivity of Co_3O_4 than that of NiCo_2O_4 , when the NiCo_2O_4 nanosheets are replaced by Co_3O_4 nanosheets, the energy density, power density and the rate capability of the electrodes significantly decreased. The $\text{Ni(OH)}_2@ \text{MnCo}_2\text{O}_4$ multicomponent core-shell hybrid on nickel foam fabricated through a facile hydrothermal approach not only ensured the synergetic effect of the two pseudocapacitive materials, but also promoted the diffusion of electrolyte ions during the rapid charge/discharge process (Zhao et al., 2016). It exhibited an ultrahigh specific capacitance of 2154 F g^{-1} at a current density of 5 A g^{-1} , and its ASC device also displayed excellent electrochemical performance of high energy densities of 48 Wh kg^{-1} at 1.4 kW kg^{-1} , and long cycling lifespan (90 % capacitance retention after 2500 cycles).

Cobalt sulfides has been extensively studied as core materials. Similar to bimetallic oxides, bimetallic sulfides (NiCoS , ZnCoS) exhibit two orders of electrical conductivity in magnitude larger than their monometallic sulfides, and possess superior electrochemical characteristics over their monometallic sulfides (T. Wang

et al., 2019). A novel hierarchical Ni(OH)₂@Co₉S₈ nanotube arrays on carbon fibers have been synthesized for supercapacitor application (Zhu et al., 2017). The one-dimensional Co₉S₈ nanotubes served as an ideal backbone to improve the electrical conductivity of Ni(OH)₂ nanosheets, whereas the ultrathin Ni(OH)₂ nanosheets electrodeposited on the Co₉S₈ nanotubes greatly enhanced the surface area and provided more electroactive sites for faradaic reaction. The 3D Ni(OH)₂@CoS nanocomposite demonstrated the synergistic advantages of CoS and Ni(OH)₂ (S. Li et al., 2016). The composite of CoS and the Ni(OH)₂ with high specific capacitance on Ni foam showed high specific capacitance is 1837 F g⁻¹ at a scan rate of 1 mV s⁻¹, which is higher than both the bare CoS electrode and Ni(OH)₂ electrode. It exhibited an excellent cycle stability of 95.8 % retention of the initial capacitance after 5000 cycles. The remarkable performance can be attributed to the unique 3D nanoporous structure of Ni(OH)₂@CoS.

The hierarchical zinc cobalt sulfide (ZCS) hollow nanotube arrays wrapped with interlaced ultrathin Ni(OH)₂ nanoflakes (Ni(OH)₂@ZCS) on nickel foam has been successfully prepared by a complicated process of hydrothermal growth, anion exchange and an electrodeposition (Syed et al., 2017). The ZCS as the core has a unique pentagonal cross-section and a rough surface, which facilitates the deposition of Ni(OH)₂ nanoflakes. Due to enhanced redox reactions, the superhighway for electron transport and the increased availability of electrochemical active sites of Ni(OH)₂ flakes, the Ni(OH)₂@ZCS hierarchical electrode exhibited a high specific capacitance of 2156 F g⁻¹ and excellent cyclic stability with 94 % retention over 3000 cycles. The ASC achieved a high energy density of 74.93 Wh kg⁻¹ and superior cyclic stability of 78 % retention with 81 % columbic efficiency over 10000 cycles. The Ni(OH)₂@NiCo₂S₄ on carbon fabric as high-performance supercapacitor electrodes with a core-shell has been rationally designed (Zhang et al., 2015). The NiCo₂S₄ nanotube core has a diameter of about 120 nm and a thickness of about 25 nm. The Ni(OH)₂ shell is made up of ultrathin sheets. Due to the synergistic effect, the Ni(OH)₂@NiCo₂S₄ showed a high specific capacitance of 2700 F g⁻¹ at a current density of 1 mA cm⁻² and good cycle stability with 78 % capacitance retention after 2000 cycles.

Although the 3D core-shell electrodes of Ni(OH)₂ grown on conductive scaffolds have achieved improved electrochemical performance, the specific capacitance of Ni(OH)₂ is still much lower than the theoretical value. In addition, there still exists some deficiencies in the structure of electrodes, which seriously restrict the further improvements in electrochemical performance. First, even though the core materials have better conductivities than Ni(OH)₂, the electrical conductivity of core materials is still poor due to the limited conductivity of semiconductor materials, which limits the rate performance at high current densities. Secondly, the 3D core-shell electrode always requires additional conductive scaffold to keep self-supported structure ensuring good electrical conductivity. However, the 3D conductive scaffolds normally possess large pores, large fibers or wires, such as 3D graphene with a large pore size distribution from a few tens to several hundred micrometers, carbon fabric with fiber diameters more than tens of micrometers, and nickel foam with wire diameters of 60 micrometers and pore sizes of several hundred micrometers. The large pores, large fiber/wire diameters, and the unwanted weight of conductive scaffolds often lead to relative low volumetric/gravimetric energy densities, making the 3D core-shell electrodes inadequate for practical applications (Kang et al., 2017). Therefore, to further improve the electrochemical performance of 3D Ni(OH)₂ electrodes with core-shell structure through reasonable structure and material design is still a great challenge.

References

- Augustyn, V., Simon, P., Dunn, B., 2014. Pseudocapacitive oxide materials for high-rate electrochemical energy storage. *Energy Environ. Sci.* 7, 1597–1614.
- Bai, X., Liu, Q., Liu, J., Zhang, H., Li, Z., Jing, X., Liu, P., Wang, J., Li, R., 2017. Hierarchical Co₃O₄@Ni(OH)₂ core-shell nanosheet arrays for isolated all-solid state supercapacitor electrodes with superior electrochemical performance. *Chem. Eng. J.* 315, 35–45.
- Bakker, M.G., Frazier, R.M., Burkett, S., Bara, J.E., Chopra, N., Spear, S., Pan, S., Xu, C., 2011. Perspectives on supercapacitors, pseudocapacitors and batteries. *Nanomater. Energy* 1, 136–158.

- Borenstein, A., Hanna, O., Attias, R., Luski, S., 2017. Carbon-based composite materials for supercapacitor electrodes: a review. *J. Mater. Chem. A* 5, 12653–12672.
- Cai, D., Huang, H., Wang, D., Liu, B., Wang, L., Liu, Y., Li, Q., Wang, T., 2014. High-performance supercapacitor electrode based on the unique ZnO@Co₃O₄ core/shell heterostructures on nickel foam. *ACS Appl. Mater. Interfaces* 6, 15905–15912.
- Cao, J., Li, X., Wang, Y., Walsh, F.C., Ouyang, J.H., Jia, D., Zhou, Y., 2015. Materials and fabrication of electrode scaffolds for deposition of MnO₂ and their true performance in supercapacitors. *J. Power Sources* 293, 657–674.
- Chen, J., Li, C., Shi, G., 2013. Graphene Materials for Electrochemical Capacitors. *J. Phys. Chem. Lett.* 4, 1244–1253.
- Chen, T., Dai, L., 2013. Carbon nanomaterials for high-performance supercapacitors. *Biochem. Pharmacol.* 16, 272–280.
- Cheng, J.P., Zhang, J., Liu, F., 2014. Recent development of metal hydroxides as electrode material of electrochemical capacitors. *RSC Adv.* 4, 38893–38917.
- Dong, B., Li, M., Chen, S., Ding, D., Wei, W., Gao, G., Ding, S., 2017. Formation of g-C₃N₄@Ni(OH)₂ Honeycomb Nanostructure and Asymmetric Supercapacitor with High Energy and Power Density. *ACS Appl. Mater. Interfaces* 9, 17890–17896.
- Faraji, S., Ani, F.N., 2015. The development supercapacitor from activated carbon by electroless plating - A review. *Renew. Sustain. Energy Rev.* 42, 823–834.
- Hong, W., Wang, J., Niu, L., Sun, J., Gong, P., Yang, S., 2014. Controllable synthesis of CoAl-LDH@Ni(OH)₂ nanosheet arrays as binder-free electrode for supercapacitor applications. *J. Alloys Compd.* 608, 297–303.
- Huang, L., Chen, D., Ding, Y., Wang, Z.L., Zeng, Z., Liu, M., 2013. Hybrid composite Ni(OH)₂@NiCo₂O₄ grown on carbon fiber paper for high-performance supercapacitors. *ACS Appl. Mater. Interfaces* 5, 11159–11162.
- Jia, F., Yu, C., Deng, K., Zhang, L., 2007. Nanoporous metal (Cu, Ag, Au) films with high surface area: General fabrication and preliminary electrochemical performance. *J. Phys. Chem. C* 111, 8424–8431.
- Jiang, L. bo, Yuan, X. zhong, Liang, J., Zhang, J., Wang, H., Zeng, G. ming, 2016. Nanostructured core-shell electrode materials for electrochemical capacitors. *J. Power Sources* 331, 408–425.
- Kang, J., Zhang, S., Zhang, Z., 2017. Three-Dimensional Binder-Free Nanoarchitectures for Advanced Pseudocapacitors 1700515, 1–12.
- Ke, Q., Wang, J., 2016. Graphene-based materials for supercapacitor electrodes-A review. *J Mater.* 2, 37–54.
- Li, B., Zheng, M., Xue, H., Pang, H., 2016. High performance electrochemical capacitor materials focusing on nickel based materials. *Inorg. Chem. Front.* 3, 175–202.

- Li, S., Wen, J., Chen, T., Xiong, L., Wang, J., Fang, G., 2016. In situ synthesis of 3D CoS nanoflake/Ni(OH)₂ nanosheet nanocomposite structure as a candidate supercapacitor electrode. *Nanotechnology* 27.
- Liang, H., Lin, J., Jia, H., Chen, S., Qi, J., Cao, J., Lin, T., Fei, W., Feng, J., 2018. Hierarchical NiCo-LDH@NiOOH core-shell heterostructure on carbon fiber cloth as battery-like electrode for supercapacitor. *J. Power Sources* 378, 248–254.
- Liu, R., Duay, J., Lee, S.B., 2011. Heterogeneous nanostructured electrode materials for electrochemical energy storage. *Chem. Commun.* 47, 1384–1404.
- Liu, S., Lee, S.C., Patil, U., Shackery, I., Kang, S., Zhang, K., Park, J.H., Chung, K.Y., Chan Jun, S., 2017. Hierarchical MnCo-layered double hydroxides@Ni(OH)₂ core-shell heterostructures as advanced electrodes for supercapacitors. *J. Mater. Chem. A* 5, 1043–1049.
- Niu, H., Zhou, D., Yang, X., Li, X., Wang, Q., Qu, F., 2015. Towards three-dimensional hierarchical ZnO nanofiber@Ni(OH)₂ nanoflake core-shell heterostructures for high-performance asymmetric supercapacitors. *J. Mater. Chem. A* 3, 18413–18421.
- Ouyang, Y., Xia, X., Ye, H., Wang, L., Jiao, X., Lei, W., Hao, Q., 2018. Three-Dimensional Hierarchical Structure ZnO@C@NiO on Carbon Cloth for Asymmetric Supercapacitor with Enhanced Cycle Stability. *ACS Appl. Mater. Interfaces* 10, 3549–3561.
- Pan, Y., Gao, H., Zhang, M., Li, L., Wang, G., Shan, X., 2017. Three-dimensional porous ZnCo₂O₄ sheet array coated with Ni(OH)₂ for high-performance asymmetric supercapacitor. *J. Colloid Interface Sci.* 497, 50–56.
- Pourjavadi, A., Doroudian, M., Ahadpour, A., Pourbadiei, B., 2018. Preparation of flexible and free-standing graphene-based current collector via a new and facile self-assembly approach: Leading to a high performance porous graphene/polyaniline supercapacitor. *Energy* 152, 178–189.
- Qiu, H.J., Ito, Y., Chen, M.W., 2014. Hierarchical nanoporous nickel alloy as three-dimensional electrodes for high-efficiency energy storage. *Scr. Mater.* 89, 69–72.
- Qiu, H.J., Kang, J.L., Liu, P., Hirata, A., Fujita, T., Chen, M.W., 2014. Fabrication of large-scale nanoporous nickel with a tunable pore size for energy storage. *J. Power Sources* 247, 896–905.
- Qiu, H.J., Peng, L., Li, X., Wang, Y., 2015. Enhanced supercapacitor performance by fabricating hierarchical nanoporous nickel/nickel hydroxide structure. *Mater. Lett.* 158, 366–369.
- Radhamani, A. V., Shareef, K.M., Rao, M.S.R., 2016. ZnO@MnO₂ Core-Shell Nanofiber Cathodes for High Performance Asymmetric Supercapacitors. *ACS Appl. Mater. Interfaces* 8, 30531–30542.

- Raza, W., Ali, F., Raza, N., Luo, Y., Kim, K.H., Yang, J., Kumar, S., Mehmood, A., Kwon, E.E., 2018. Recent advancements in supercapacitor technology. *Nano Energy* 52, 441–473.
- Shao, Y., El-Kady, M.F., Sun, J., Li, Y., Zhang, Q., Zhu, M., Wang, H., Dunn, B., Kaner, R.B., 2018. Design and Mechanisms of Asymmetric Supercapacitors. *Chem. Rev.* 118, 9233–9280.
- Syed, J.A., Ma, J., Zhu, B., Tang, S., Meng, X., 2017. Hierarchical Multicomponent Electrode with Interlaced Ni(OH)₂ Nanoflakes Wrapped Zinc Cobalt Sulfide Nanotube Arrays for Sustainable High-Performance Supercapacitors. *Adv. Energy Mater.* 7, 1–12.
- Wang, T., Chen, H.C., Yu, F., Zhao, X.S., Wang, H., 2019. Boosting the cycling stability of transition metal compounds-based supercapacitors. *Energy Storage Mater.* 16, 545–573.
- Wang, Y., Song, Y., Xia, Y., 2016. Electrochemical capacitors: Mechanism, materials, systems, characterization and applications. *Chem. Soc. Rev.* 45, 5925–5950.
- Wang, Y., Yin, Z., Wang, Z., Li, X., Guo, H., Wang, J., Zhang, D., 2019. Facile construction of Co(OH)₂@Ni(OH)₂ core-shell nanosheets on nickel foam as three dimensional free-standing electrode for supercapacitors. *Electrochim. Acta* 293, 40–46.
- Wu, Y., Cao, C., 2018. The way to improve the energy density of supercapacitors: Progress and perspective. *Sci. China Mater.* 1–10.
- Yan, J., Liu, J., Fan, Z., 2012. High-performance supercapacitor electrodes based on highly corrugated graphene sheets. *Carbon N. Y.* 50, 2179–2188.
- Yan, J., Wang, Q., Wei, T., Fan, Z., 2014. Recent Advances in Design and Fabrication of Electrochemical Supercapacitors with High Energy Densities.
- Yang, G.W., Xu, C.L., Li, H.L., 2008. Electrodeposited nickel hydroxide on nickel foam with ultrahigh capacitance. *Chem. Commun.* 6537–6539.
- Yin, X., Tang, C., Zhang, L., Yu, Z.G., Gong, H., 2016. Chemical insights into the roles of nanowire cores on the growth and supercapacitor performances of Ni-Co-O/Ni(OH)₂ core/shell electrodes. *Sci. Rep.* 6, 1–12.
- Yu, K., Pan, X., Zhang, G., Liao, X., Zhou, X., Yan, M., Xu, L., Mai, L., 2018. Nanowires in Energy Storage Devices: Structures, Synthesis, and Applications. *Adv. Energy Mater.* 1802369, 1802369.
- Yu, L., Chen, G.Z., 2016. Redox electrode materials for supercapatteries. *J. Power Sources* 326, 604–612.
- Zhang, J., Gao, H., Zhang, M.Y., Yang, Q., Chuo, H.X., 2015. NiCo₂S₄/Ni(OH)₂ core-shell heterostructured nanotube arrays on carbon-fabric as high-performance pseudocapacitor electrodes. *Appl. Surf. Sci.* 349, 870–875.
- Zhang, S., Pan, N., 2015. Supercapacitors performance evaluation. *Adv. Energy Mater.* 5, 1–19.

- Zhang, Y., Feng, H., Wu, X., Wang, L., Zhang, A., Xia, T., Dong, H., Li, X., Zhang, L., 2009. Progress of electrochemical capacitor electrode materials: A review. *Int. J. Hydrogen Energy* 34, 4889–4899.
- Zhao, Y., Hu, L., Zhao, S., Wu, L., 2016. Preparation of $\text{MnCo}_2\text{O}_4@ \text{Ni}(\text{OH})_2$ Core–Shell Flowers for Asymmetric Supercapacitor Materials with Ultrahigh Specific Capacitance. *Adv. Funct. Mater.* 26, 4085–4093.
- Zhu, F., Yan, M., Liu, Y., Shen, H., Lei, Y., Shi, W., 2017. Hexagonal prism-like hierarchical $\text{Co}_9\text{S}_8@ \text{Ni}(\text{OH})_2$ core-shell nanotubes on carbon fibers for high-performance asymmetric supercapacitors. *J. Mater. Chem. A* 5, 22782–22789.
- Zhu, J., Huang, L., Xiao, Y., Shen, L., Chen, Q., Shi, W., 2014. Hydrogenated CoO_x nanowire@ $\text{Ni}(\text{OH})_2$ nanosheet core-shell nanostructures for high-performance asymmetric supercapacitors. *Nanoscale* 6, 6772–6781.

Chapter III. Experimental

3.1 Materials

Nickel sulfate ($\text{NiSO}_4 \cdot 6\text{H}_2\text{O}$), nickel chloride ($\text{NiCl}_2 \cdot 6\text{H}_2\text{O}$), Sodium hydroxide (NaOH) and ammonium persulphate ($(\text{NH}_4)_2\text{S}_2\text{O}_8$) with analytical grade were obtained from Sigma-Aldrich. Gallium-Indium eutectic (Ga-In alloy) with purity of 99.99 % was obtained from Sigma-Aldrich. Boric acid (H_3BO_4) with analytical grade was bought from J.T.Baker.

N, N-Dimethylformamide and dichloromethane (CH_2Cl_2) with analytical grade were obtained from Fermont. Porous nitrocellulose (NC) membrane with pore diameter of $0.45 \mu\text{m}$ and thickness of $150 \mu\text{m}$ was obtained from Whatman, United Kingdom. Polyester (PETE) membrane with pore diameter of 200 nm , pore density of $3 \times 10^8 \text{ pore cm}^{-2}$ and thickness of $10 \mu\text{m}$ was obtained from Sterlitech Corporation, America. Polycarbonate (PC) membrane with porosity (P) of 13.8 %, pore diameter (d) of $0.2 \mu\text{m}$, and thickness of $10 \mu\text{m}$ was obtained from Isopore, Ireland. The pore density and average pore spacing are $4 \times 10^8 \text{ pore cm}^{-2}$ and 280 nm , respectively, which were calculated according to the following equations of $P = \frac{\pi d^2}{4} \rho$ and $\rho = \frac{\pi}{2\sqrt{3}} \left(\frac{d}{D}\right)^2$ used for 2D hexagonal array, where P , d , ρ , and D are the pore porosity, pore diameter, pore density and average pore distance, respectively.

3.2 Preparation method

3.2.1 Preparation of nanoporous and nickel nanowire arrays.

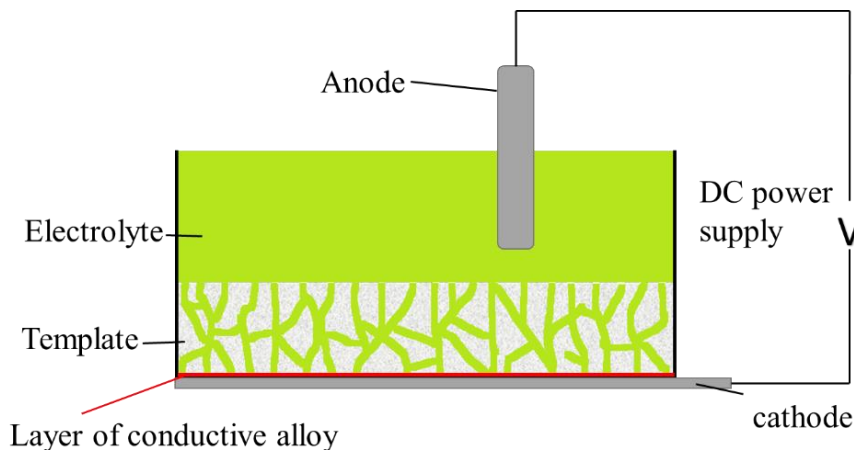


Fig. 3. 1 Schematic diagram of electrodeposition device.

The NC membrane, PETE membrane and PC membrane were used as templates for the electrodeposition of nanoporous nickel metal (NPN), upright self-supported nickel nanowire array (USNWA) and interconnected nickel nanowire array, respectively (INWA). The electrodeposition device is shown in Fig. 3.1. One side of the template was coated with Ga-In alloy to provide electrical connection to the negative pole of power supply. The electrodeposition process was carried out using a 130 g L^{-1} NiSO_4 , 20 g L^{-1} NiCl_2 and 30 g L^{-1} H_3BO_3 electrolyte. The applied DC voltage was 1.5 V for the electrodeposition of NPN, and the process lasted for 40 min. For PETE membrane, the applied voltage was 1.3 V and lasted for 30 min. For PC membrane, the applied voltage was kept at 1.3 V. When the nickel metal reached the membrane surface and formed a thin nickel film, the electrodeposition process was stopped. After the electrodeposition process, all the templates were dissolved to obtain NPN, USNWA and INWA, respectively. The NC membrane was dissolved by DMF solution, the PC membrane was dissolved by dichloromethane, the PETE membrane was dissolved by hexafluoroisopropanol.

3.2.2 Preparation of amorphous Ni(OH)₂@NPN/USNWA/INWA

The amorphous Ni(OH)₂ coating on the surfaces of NPN and nanowires was prepared by an oxidation treatment (Xiong et al., 2015). First the NPN and nanowire arrays were kept in a damp environment for 24 h and then immersed in a mixed solution of 3 M NaOH and 6 M ammonium persulphate ((NH₄)₂S₂O₈) for 6 h. After the oxidation process, the Ni(OH)₂@NPN, Ni(OH)₂@USNWA and Ni(OH)₂@INWA were obtained.

3.3 Material characterization

The material crystal structures were investigated by powder X-ray diffraction (XRD) (D8 Advance, Bruker, Germany) equipped with a Cu K α radiation source ($\lambda=0.15406$ nm) operated at 40 kV, and the chemical compositions of materials were investigated by X-ray photoelectron spectroscopy (XPS, Thermo ESCALAB, 250Xi). The microstructure and morphology of nickel nanowire array and Ni(OH)₂ were analyzed using a field-emission scanning electron microscope (FESEM Helios Nanolab 600, FEI, Holand) with an accelerating voltage of 15 kV, transmission electron microscopy (TEM, FEI Tecnai G2 F20, 200 kV).

3.4 Electrochemical measurements

The Ni(OH)₂@NPN, Ni(OH)₂@USNWA and Ni(OH)₂@INWA can be used as working electrodes directly. All the electrochemical measurements were conducted on an electrochemical workstation (EC-lab VSP-300, France) using 6 M KOH aqueous solution. The electrochemical performance of single electrode was tested using a three-electrode system with a saturated calomel reference electrode (SCE) and a Pt foil counter electrode.

Cyclic voltammetry (CV) curves were measured at different scan rates from 5 to 200 mV s⁻¹. Galvanostatic charge/discharge (GCD) measurements were tested at different current densities. The electrochemical impedance spectroscopy (EIS) measurements were performed in the frequency range from 10⁵ to 10⁻² Hz at an open

circuit potential with an AC perturbation of 5 mV. The specific capacitances (C_s , F g⁻¹) were calculated from the following equation (Dubal et al., 2015):

$$C_s = \frac{I \times \Delta t}{m \times (\Delta V)} \quad (3-1)$$

where I (A), Δt (s), ΔV (V), and m (g) are the discharge current, discharge time, total potential range, and mass of Ni(OH)₂ on the surface of nickel nanowire, respectively. The mass of NPN, USNWA and INWA before and after oxidation were weighted by a microbalance (METTLER TOLEDO, XS 105) with a minimum measurement increment of 0.01 mg. According to the material transformation of Ni to Ni(OH)₂, the mass of Ni(OH)₂ was calculated from the change of mass before and after oxidation. The loading mass of Ni(OH)₂ was about of 1.59 mg cm⁻² (thickness: 90 μm).

Graphene oxide (GO) was initially prepared from natural graphite by a modified Hummers' method. GO suspension was prepared by dispersing 140 mg of GO in 70 mL of deionized water with ultrasonic treatment for 30 min. The obtained GO suspension was transferred into a 100 mL Teflon lined autoclave and maintained at 180 °C for 12 h. The autoclave was cooled to room temperature naturally. Then, the obtained reduced graphene oxide (rGO) was washed with deionized water, and dried by freeze vacuum drier for 24 h.

An asymmetric supercapacitor (Ni(OH)₂@INWA//rGO) was assembled with Ni(OH)₂@INWA as positive material, reduced graphene oxide (rGO) as negative material, and a piece of polypropylene paper as a separator in a 6 M KOH solution. The negative electrode was prepared by mixing the rGO, acetylene black and polytetrafluorene-ethylene (PTFE) binder with a weight ratio of 8:1:1, followed by kneading and rolling mixtures into nickel foam. The optimal mass ratio between the positive and negative electrode was obtained based on the following equation (Wang et al., 2016):

$$\frac{m_+}{m_-} = \frac{C_- \times \Delta V_-}{C_+ \times \Delta V_+} \quad (3-2)$$

where m_+ and m_- are the mass of positive and negative active materials, C_+ and C_- are the specific capacitance of positive and negative electrodes, and ΔV_+ and ΔV_- are the potential window of positive and negative electrodes. The ratio of the positive and negative active materials is 0.12. For the two-electrode system, the specific capacitance, energy and power densities of Ni(OH)₂@INWA//rGO were calculated from the GCD curves according to the following equations (Wang et al., 2016):

$$C_s = \frac{I \times \Delta t}{m \times (\Delta V)} \quad (3-3)$$

$$E = \frac{C_{sp} \times (\Delta V)^2}{2 \times 3.6} \quad (3-4)$$

$$P = \frac{3600 \times E}{\Delta t} \quad (3-5)$$

where m (g) is the total mass of electroactive materials in the positive and negative electrodes, ΔV (V) is the cell voltage excluding the IR drop, Δt is the discharge time, E (Wh, kg⁻¹) is the energy density, and P (W, kg⁻¹) is the average power density.

References

- Dubal, D.P., Gomez-Romero, P., Sankapal, B.R., Holze, R., 2015. Nickel cobaltite as an emerging material for supercapacitors: An overview. *Nano Energy* 11, 377–399.
- Wang, J., Zhang, X., Wei, Q., Lv, H., Tian, Y., Tong, Z., Liu, X., Hao, J., Qu, H., Zhao, J., Li, Y., Mai, L., 2016. 3D self-supported nanopine forest-like Co₃O₄@CoMoO₄ core-shell architectures for high-energy solid state supercapacitors. *Nano Energy* 19, 222–233.
- Xiong, X., Ding, D., Chen, D., Waller, G., Bu, Y., Wang, Z., Liu, M., 2015. Three-dimensional ultrathin Ni(OH)₂ nanosheets grown on nickel foam for high-performance supercapacitors. *Nano Energy* 11, 154–161.

Chapter IV. Facile fabrication of amorphous $\text{Ni}(\text{OH})_2$ @nanoporous nickel with rational pore structure

4.1 Material characterization

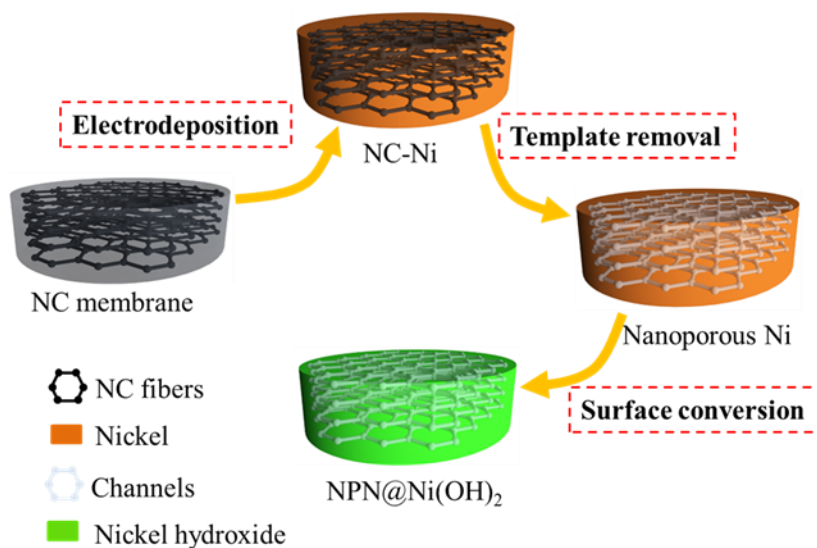
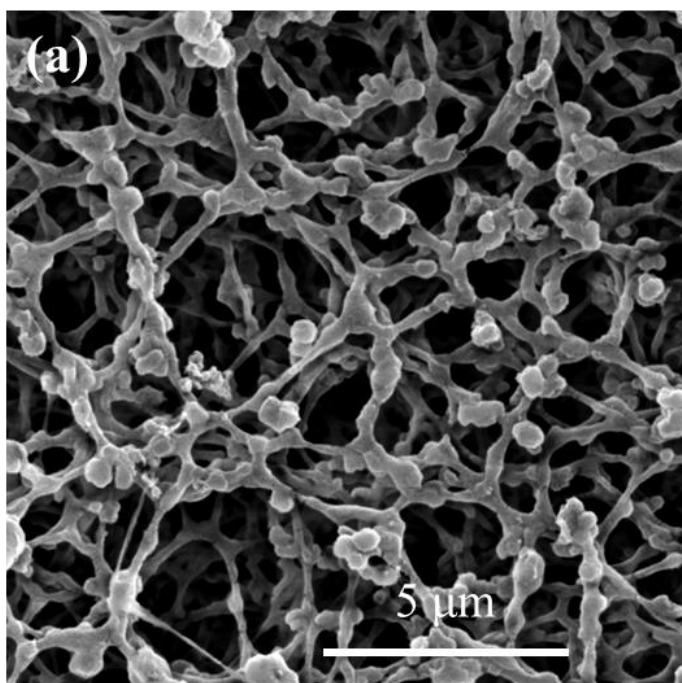


Fig. 4. 1 Schematic illustration of the fabrication of $\text{Ni}(\text{OH})_2$ @NPN through a template-directed electrodeposition and surface conversion process.



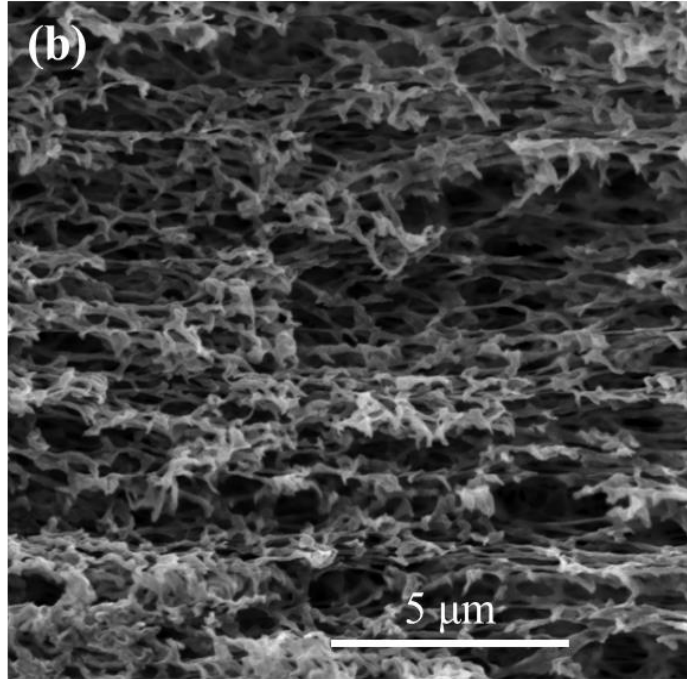


Fig. 4. 2 Micrographs of the NC membrane: (a) Surface morphology; (b) Cross-section morphology.

The facile fabrication process of $\text{Ni}(\text{OH})_2@\text{NPN}$ is schematically illustrated in Fig. 4.1. Firstly, template-directed electrodeposition was carried out to deposit metallic nickel into the porous NC membrane. After the electrodeposition process, the NC membrane was dissolved to obtain NPN. Finally, the $\text{Ni}(\text{OH})_2@\text{NPN}$ was prepared by directly converting the surface metallic Ni of NPN into $\text{Ni}(\text{OH})_2$ through surface oxidation treatment.

NC membrane was selected as the template to control the pore structure of porous Ni in the electrodeposition process. The microstructure of the NC membrane is shown in Fig. 4.2. The surface morphology presented in Fig. 4.2(a) shows that the NC fibers have a diameter of a few hundred nanometers, and connect with each other forming a network. The network structure of the NC template with fiber diameter of a few hundred nanometers indicates that the NPN fabricated with this template can have network-like pore channels with diameter of a few hundred nanometers. The cross-section morphology of the NC membrane is shown in Fig. 4.2(b). A large number of networks stack together forming a layered-like structure in

the thickness direction. Therefore, the NC membrane has a network structure in the horizontal direction and a layered structure in the thickness direction.

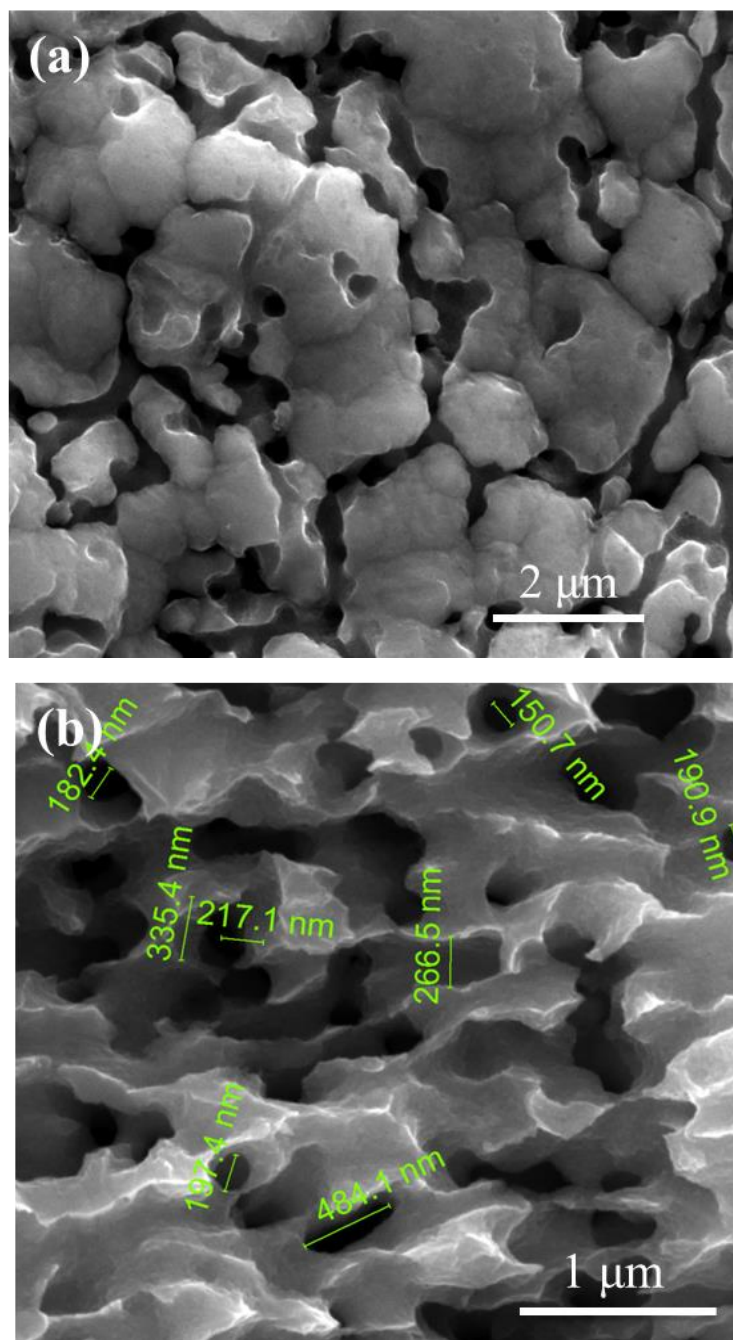
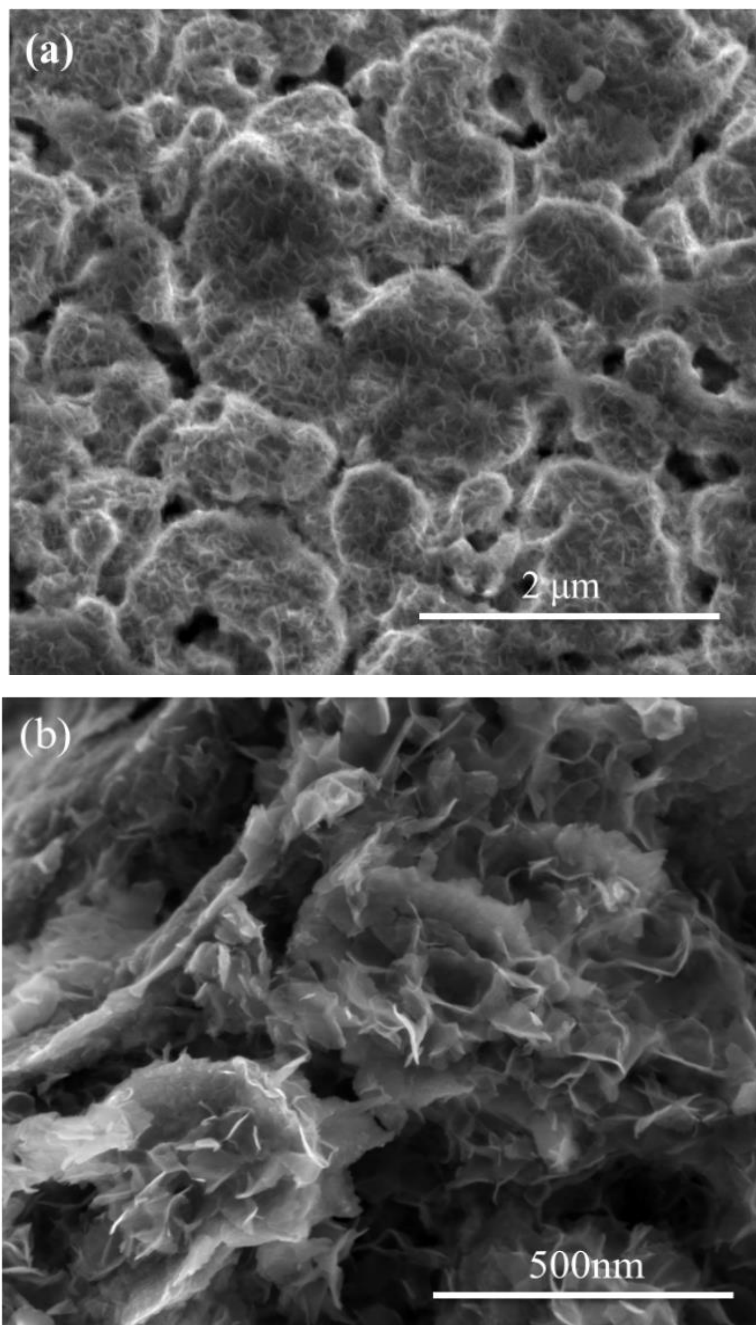


Fig. 4. 3 SEM images of the NPN: (a) Surface morphology; (b) Cross-section morphology.

Fig. 4.3 shows the microstructure of the NPN. Abundant pores and interconnected channels are observed on the surface of the NPN confirming the formation of network-like pore channels, as shown in Fig. 4.3(a). From the cross-

section morphology, as shown in Fig. 4.3(b), abundant pores can be observed inside the NPN, and the pore diameters are in the range of 150 to 300 nm. Since the pore structure of the NPN is determined by the fiber structure of the NC membrane, the inner pores of the NPN interconnect with each other forming a network of channels. The interconnected channels inside the NPN can provide short pathways for rapid diffusion of the electrolyte ions.



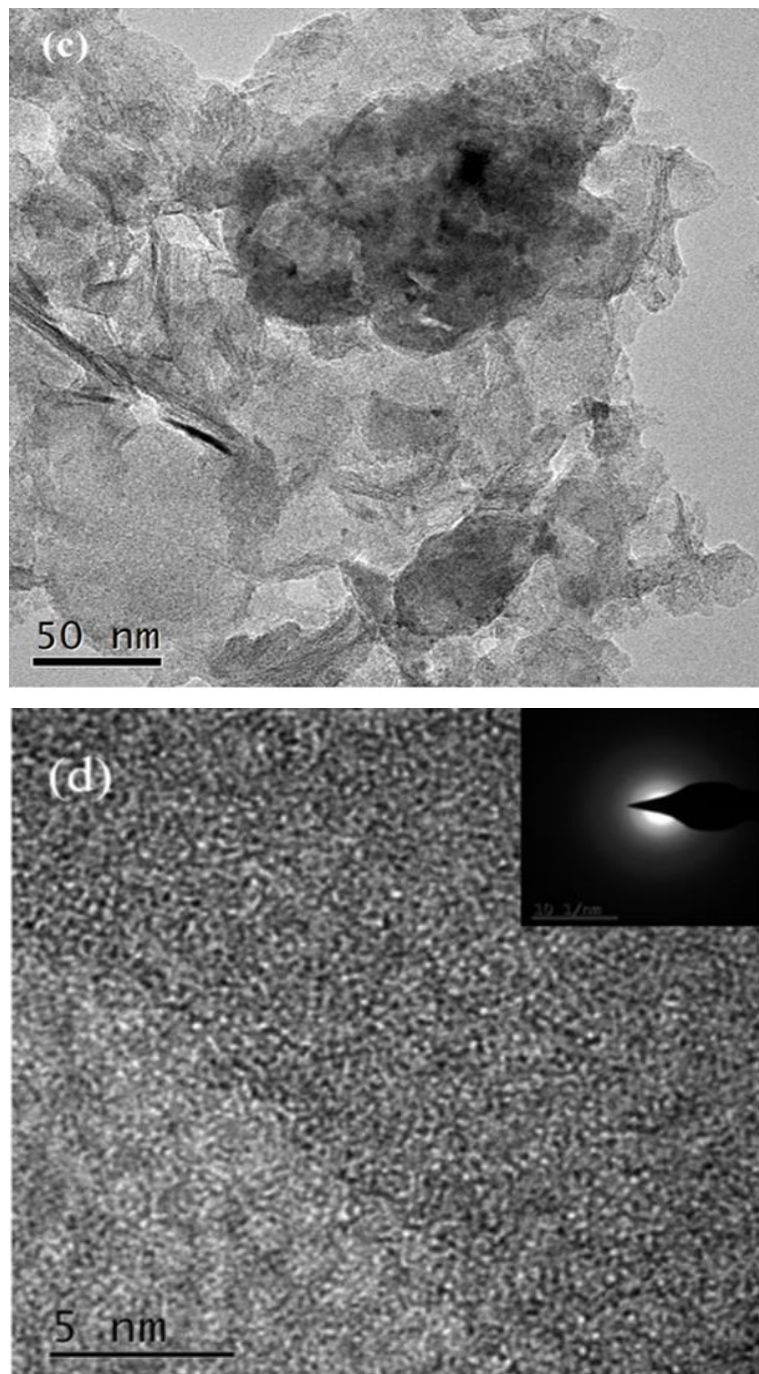
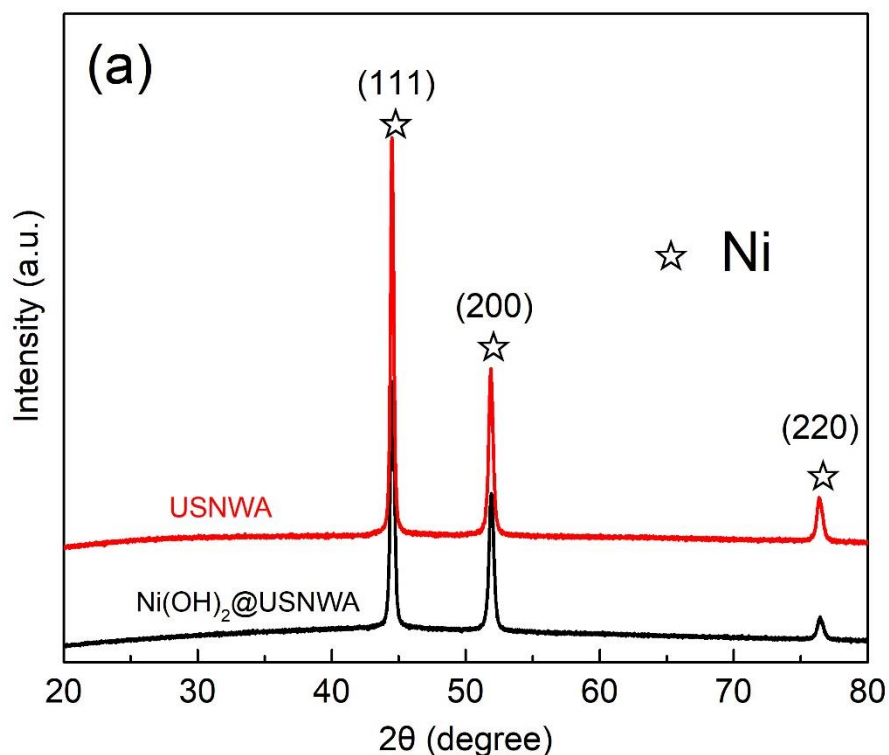


Fig. 4. 4 SEM and TEM images of Ni(OH)₂@NPN: (a) Surface morphology; (b) Cross-section morphology; (c) TEM image of Ni(OH)₂; (d) HRTEM image of Ni(OH)₂ and the corresponding SAED pattern.

As shown in Fig. 4.4(a), abundant Ni(OH)₂ nanosheets coat the outer surface of the NPN after surface oxidation treatment. In the inner channels of NPN, as shown in Fig. 4.4(b), a homogeneous distribution of Ni(OH)₂ nanosheets are observed, and

almost completely fill the inner space. It also can be seen that the $\text{Ni}(\text{OH})_2$ has large nanosheets and highly porous structure. The $\text{Ni}(\text{OH})_2$ nanosheets formed by direct conversion of the surface metallic nickel are in stable contact with the nickel scaffold. The seamless interface of $\text{Ni}(\text{OH})_2$ and nickel scaffold results in a low interfacial resistance for fast electron transfer through the interface. The TEM image of $\text{Ni}(\text{OH})_2$ scraped from the surface of $\text{Ni}(\text{OH})_2$ @NPN is shown in Fig. 4.4(c). It can be seen that the nanosheets with multi-layers exhibit a high degree of transparency, which indicates that the nanosheets are ultrathin. The ultrathin and porous structure of $\text{Ni}(\text{OH})_2$ nanosheets can provide a large number of electroactive sites exposed to the electrolyte, and significantly increase the utilization of $\text{Ni}(\text{OH})_2$. The HRTEM image of $\text{Ni}(\text{OH})_2$ shown in Fig. 4.4(d) displays an amorphous phase without any lattice structure (Li et al., 2013). The corresponding selected area electron diffraction (SAED) pattern, inset of Fig. 4.4(d), shows a broad and diffused halo ring, which indicates that the $\text{Ni}(\text{OH})_2$ is amorphous (Su et al., 2014).



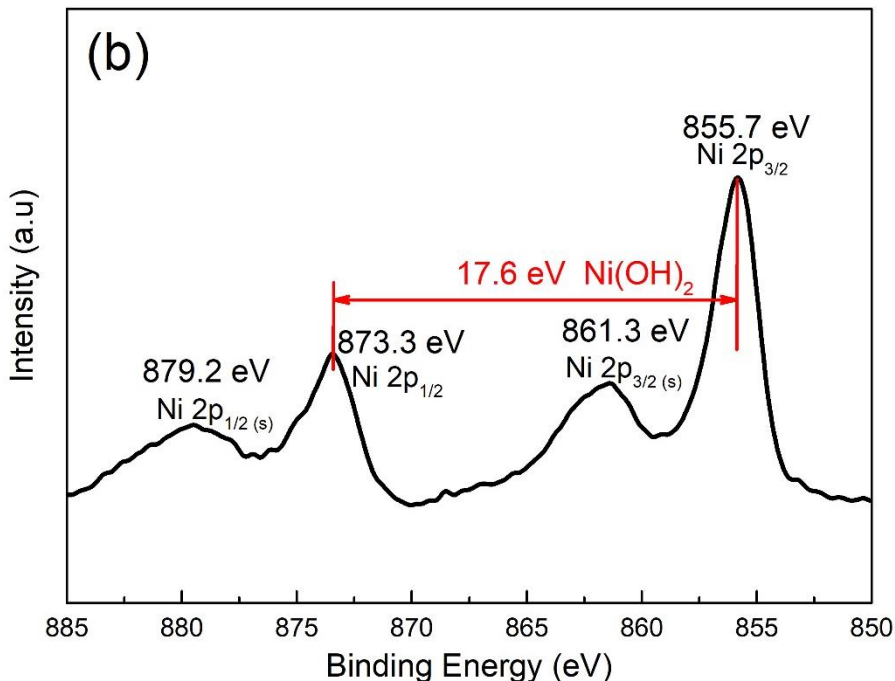
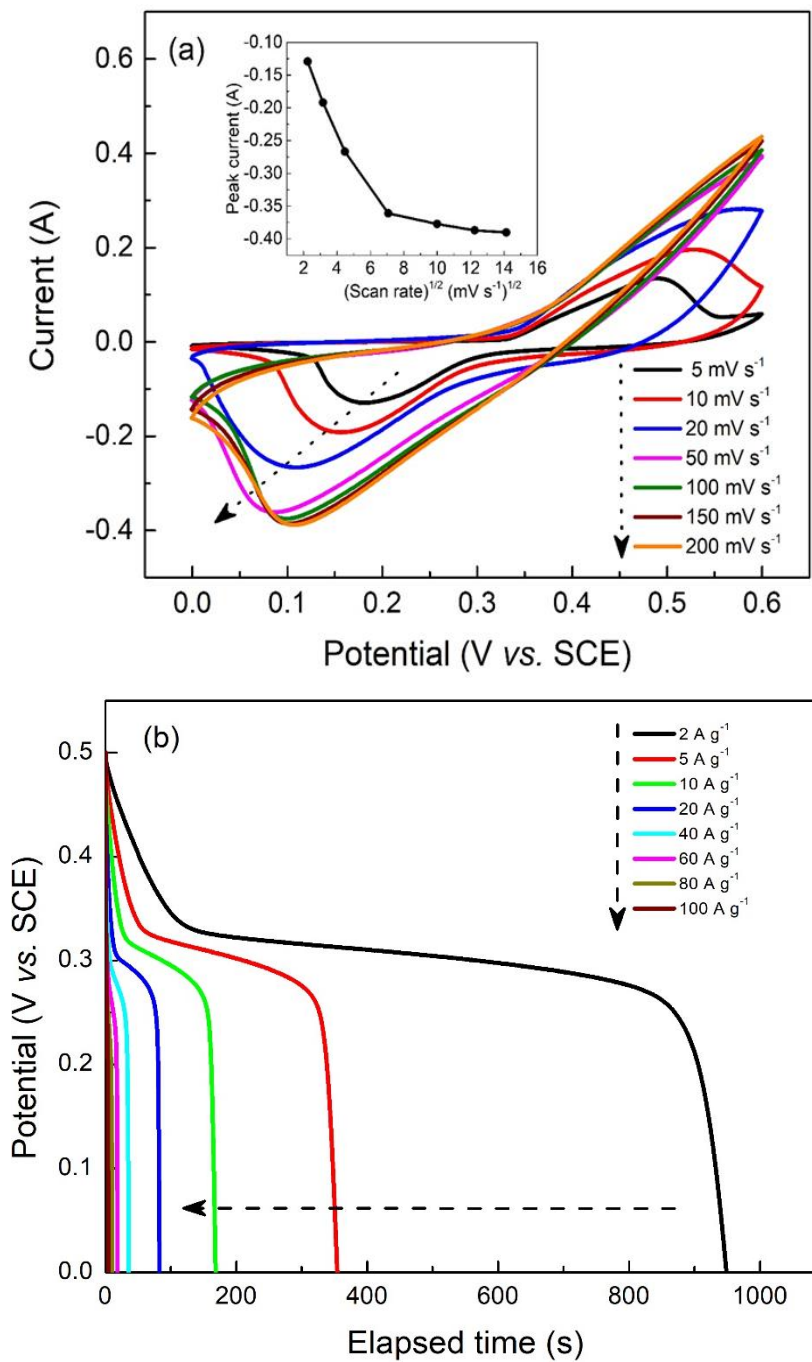


Fig. 4. 5 (a) XRD patterns of NPN and Ni(OH)₂@NPN; (b) Ni 2p XPS spectrum of Ni(OH)₂@NPN.

The crystallographic structure and chemical composition of Ni(OH)₂@NPN were characterized by XRD and XPS, respectively. The XRD patterns of NPN and Ni(OH)₂@NPN are presented in Fig. 4.5(a). It can be seen that the XRD pattern of Ni(OH)₂@NPN with lower intensity has the same characteristic peaks as that of the NPN. The diffraction angles located at 44.80°, 52.75°, and 77.52° can be assigned to the (111), (200) and (220) Bragg's reflections of monoclinic Ni (JCPDS 04-850) (Xu et al., 2016). There is no Ni(OH)₂ characteristic peaks on the XRD pattern of Ni(OH)₂@NPN. Therefore, the XRD results further demonstrate that the Ni(OH)₂ on the surface of NPN is amorphous, which is in agreement with the result of HRTEM. The Ni 2p XPS spectrum, as shown in Fig. 4.5(b), shows two peaks located at around 855.7 and 873.3 eV that correspond to Ni 2p_{3/2} and Ni 2p_{1/2}, respectively (Li et al., 2018). The other two peaks located at 879.2 and 861.3 eV correspond to the Ni 2p_{1/2} and Ni 2p_{3/2} satellites, respectively. The spin-orbit splitting energy value of Ni 2p_{1/2} and Ni 2p_{3/2} is 17.6 eV, which is the characteristic of Ni(OH)₂ phase (Xi et al., 2017).

4.2 Electrochemical characterization



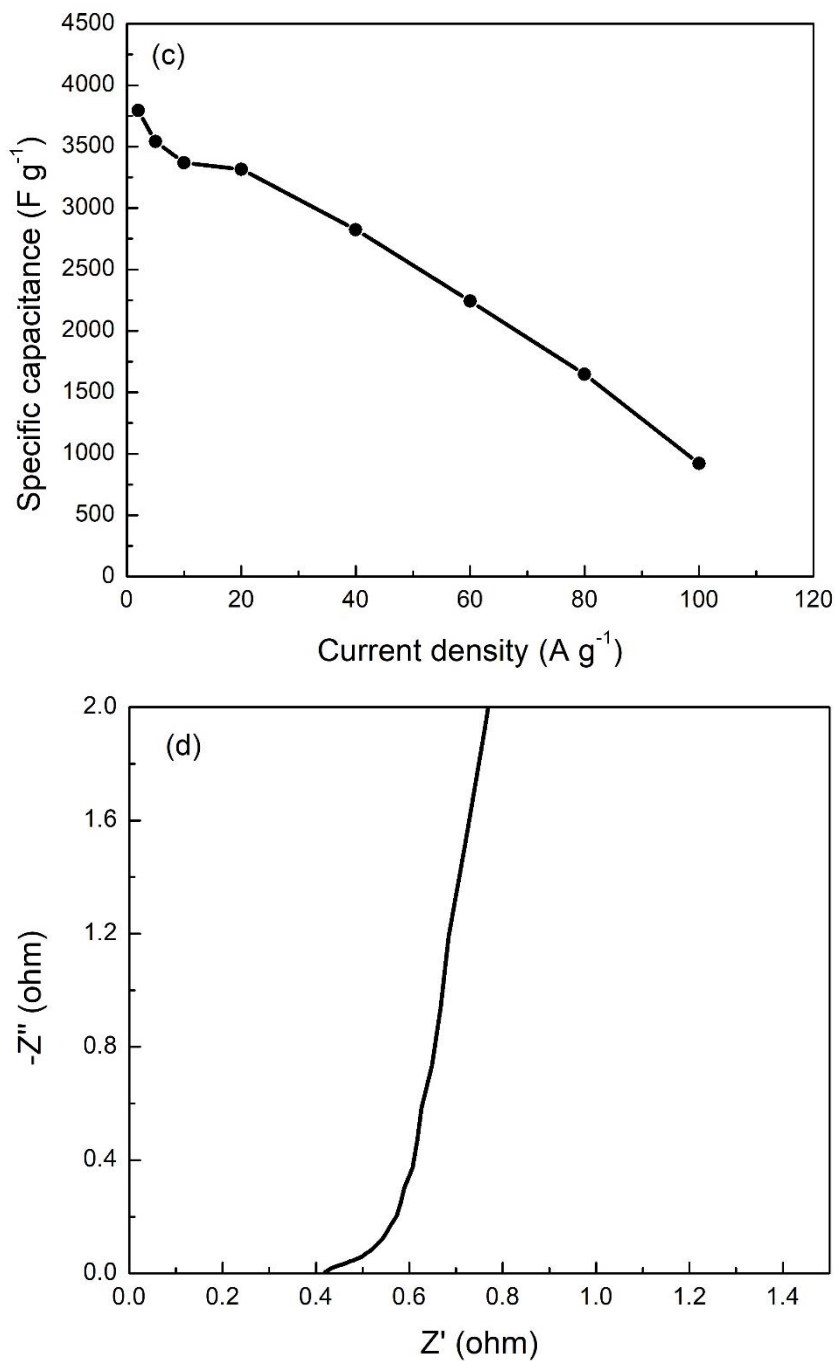


Fig. 4. 6 (a) CV curves of Ni(OH)₂@NPN at different scan rates from 5 to 200 mV s⁻¹; (b) Discharge curves at different current densities; (c) Specific capacitance of Ni(OH)₂@NPN as a function of current density; (d) Electrochemical impedance spectroscopy of Ni(OH)₂@NPN.

To evaluate the electrochemical performance of the Ni(OH)₂@NPN, the electrochemical measurements of cyclic voltammetry (CV), galvanostatic

charge/discharge (GCD) and electrochemical impedance spectroscopy (EIS) were carried out.

The CV curves of Ni(OH)₂@NPN measured in the potential window of 0 to 0.6 V at scan rates from 5 to 200 mV s⁻¹ are shown in Fig. 4.6(a). A pair of redox peaks are observed on each CV curve, which corresponds to the reversible redox reaction between Ni²⁺/Ni³⁺ and OH⁻¹ anions (Wang et al., 2013). The significant redox peaks demonstrate that the energy-storage mechanism is mainly ascribed to the Faradic redox reaction. As shown in the insert of Fig. 4.6(a), the peak current increases linearly with the increase in square root of scan rate from 5 to 20 mV s⁻¹, indicating the diffusion-controlled process and high reversibility of the redox reactions (Peng et al., 2017). However, in the scan rate ranging from 50 to 200 mV s⁻¹, the peak currents remain almost constant. At high scan rates, the increase in ion diffusion rate might be limited by the pore structure of NPN that the pore channels in each layer are not well connected with the pore channels in adjacent layers in the vertical direction.

GCD measurements of Ni(OH)₂@NPN were carried out at current densities from 2 to 100 A g⁻¹. Fig. 4.6(b) shows the discharge curves within a potential range of 0-0.5 V. A distinct plateau region can be observed on each discharge curve, indicating that the capacitance mainly comes from Faradaic redox reaction, which is consistent with the results of the CV curves (Ge et al., 2019; Zhang et al., 2016; Zhu et al., 2014). The calculated specific capacitance according to the corresponding discharge curve as a function of discharge current density is shown in Fig. 4.6(c). At a current density of 2 A g⁻¹, the Ni(OH)₂@NPN shows an ultrahigh specific capacitance of 3790 F g⁻¹. The high specific capacitance may result from the hierarchical structure of the amorphous Ni(OH)₂, which leads to a high utilization of the Ni(OH)₂ during the charge/discharge process. With the increase in current density from 2 to 20 A g⁻¹, the specific capacitance slowly decreases to 3210 F g⁻¹. As the current density increases from 20 to 100 A g⁻¹, the specific capacitance also decreases slowly to 920 F g⁻¹. Therefore, the Ni(OH)₂@NPN shows excellent rate capability. This rate capability may result from the interconnected channels of Ni(OH)₂@NPN, and the seamless contact between the Ni(OH)₂ and the conductive

nickel scaffold, which not only ensures good electronic conductivity for charge transfer but also provide efficient pathways for rapid ion diffusion.

EIS was performed to further explore the electrochemical performance of the Ni(OH)₂@NPN in the frequency range of 10⁵-10⁻² Hz. As shown in Fig. 4.6(d), the Nyquist plot of Ni(OH)₂@NPN intersects the real axis (Z') in the high-frequency region and a nearly straight line in the low-frequency region. The intercept at the real axis represents the serial resistance (R_s), which is composed of the electrolyte solution resistance, the intrinsic resistance of the active material, and the contact resistance at the active material/current collector interface (Raza et al., 2018; Zhang et al., 2016). The Ni(OH)₂@NPN has a small serial resistance of $R_s=0.41 \Omega$, indicating its good electronic conductivity. The good conductivity can be attributed to the conductive nickel scaffold and the seamless contact between Ni(OH)₂ and nickel scaffold. The diameter of the semicircle is correlated to the interfacial charge-transfer resistance (R_{ct}) caused by Faradic redox reactions (Liang et al., 2018; Wan et al., 2017). However, on the Nyquist plot of Ni(OH)₂@NPN, no semicircle can be observed. The absence of the semicircle indicates the Ni(OH)₂@NPN has an ultralow charge transfer resistance.

The slope of the straight line in the low-frequency region corresponds to the Warburg impedance resistance (Z_w), resulting from the frequency dependence of ion diffusion of the electrolyte into the electrode surface (Du et al., 2018). The straight line of Ni(OH)₂@NPN is nearly vertical suggesting a low diffusion resistance. The low diffusion resistance can be attributed to the interconnected pore channels and highly porous Ni(OH)₂ nanosheets, which effectively shorten the transport distance for rapid diffusion of electrolyte ions onto the active material surface.

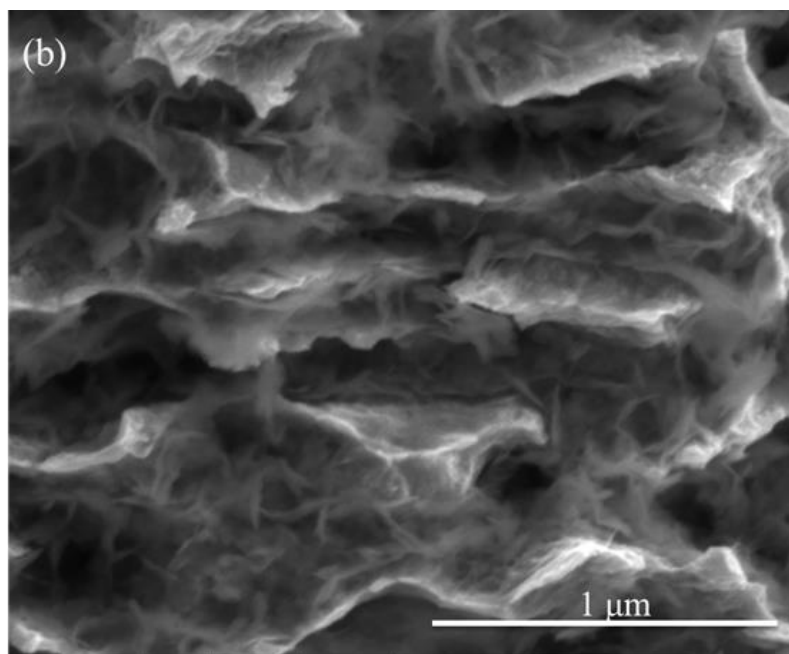
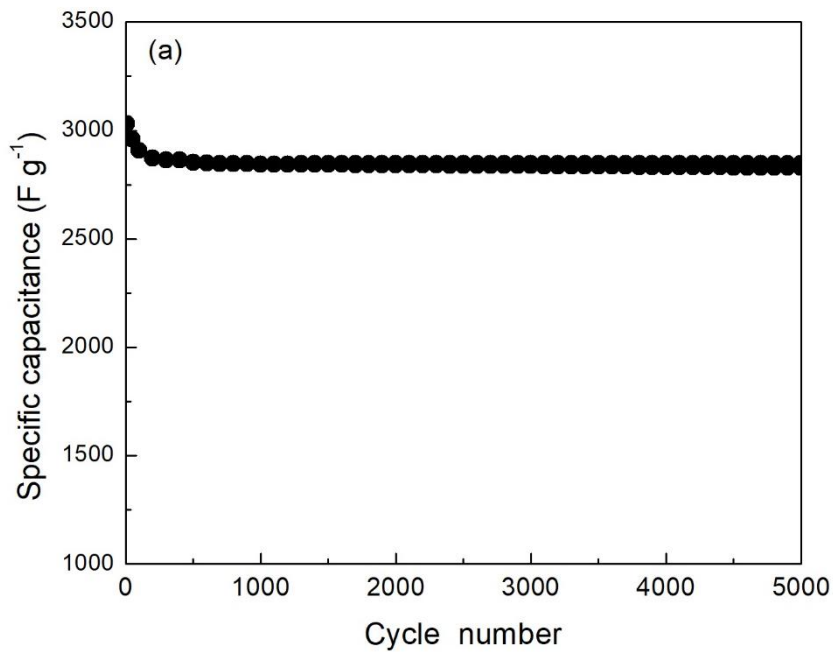


Fig. 4. 7 (a) Cyclic performance of Ni(OH)₂@NPN at a current density of 20 A g⁻¹; (b) Morphology of Ni(OH)₂@NPN after cycle test.

The cyclic stability of Ni(OH)₂@NPN was tested at a constant current density of 20 A g⁻¹ in the potential range of 0-0.5 V for 5000 cycles. As shown in Fig. 4.7(a), the specific capacitance gradually decreases from 3030 to 2860 F g⁻¹ during the first 300 cycles (94 % is retained). Finally, 92 % of the capacitance is retained after 5000

cycles, exhibiting a superior cycling stability during at a large current density. After the cycle test, the morphology of Ni(OH)₂@NPN is shown in Fig. 4.7(b). It can be seen that there still exists abundant Ni(OH)₂ nanosheets on the inner surface of NPN, further confirming the superior cycling stability.

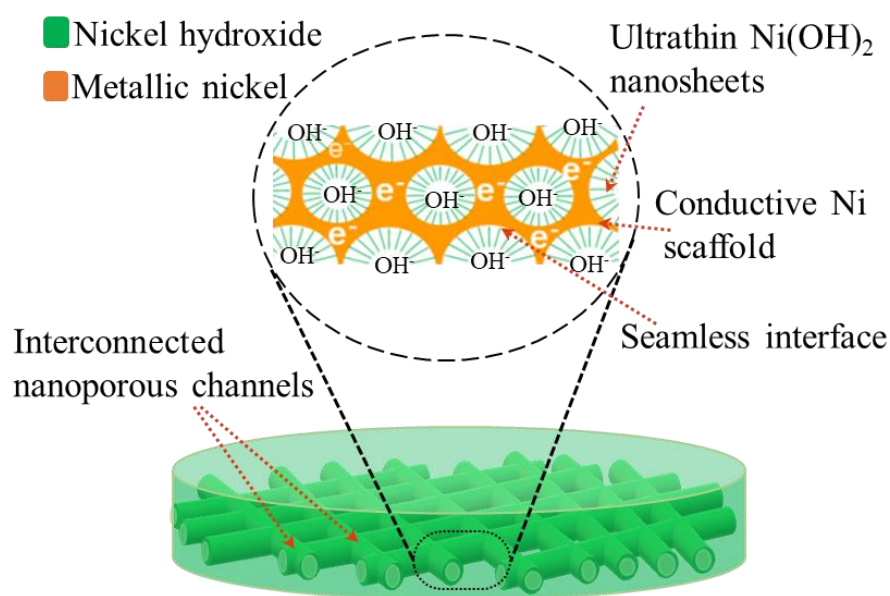


Fig. 4. 8 Schematic illustration of the structure and advantages of Ni(OH)₂@NPN.

The Ni(OH)₂@NPN electrode exhibits high specific capacitance, excellent rate capability and cycling stability, which can be attributed to the material and structural advantages of the Ni(OH)₂@NPN as shown in Fig. 4.8. Firstly, the abundant and amorphous Ni(OH)₂ nanosheets on both the inner and outer surface of NPN guarantee its high utilization during the charge/discharge process. Secondly, the Ni(OH)₂ prepared by surface conversion is in stable contact with the conductive Ni scaffold, which can guarantee the stable contact between Ni(OH)₂ and conductive Ni scaffold, and result in a interfacial; resistance. Thirdly, the NPN with interconnected pore channels not only provide inner space for the formation of Ni(OH)₂ with large nanosheets, but also offer good electrical conductivity for rapid electron transfer and short pathways for fast ion diffusion.

4.3 Conclusions

In summary, nanoporous nickel with rational pore structure coated with amorphous Ni(OH)₂ nanosheets have been successfully fabricated by a facile and low-cost process. The amorphous Ni(OH)₂@NPN has interconnected pore channels with diameters of a few hundred nanometers, and abundant Ni(OH)₂ with large and ultrathin nanosheets grown on the inner surface the pore channels. The porous Ni(OH)₂ are in stable contact with the metallic Ni of NPN. Due to its amorphous and structural features, the Ni(OH)₂@NPN exhibits an ultrahigh specific capacitance of 3790 F g⁻¹ at a current density of 2 A g⁻¹, remarkable rate capability (3210 F g⁻¹ at 20 A g⁻¹, 2244 F g⁻¹ at 60 A g⁻¹), and excellent cyclic stability of 94 % retention at a current density of 20 A g⁻¹ for 5000 cycles. The high electrochemical performance of Ni(OH)₂@NPN make it a promising candidate for supercapacitor electrode.

References

- Du, Q., Su, L., Hou, L., Sun, G., Feng, M., Yin, X., Ma, Z., Shao, G., Gao, W., 2018. Rationally designed ultrathin Ni-Al layered double hydroxide and graphene heterostructure for high-performance asymmetric supercapacitor. *J. Alloys Compd.* 740, 1051–1059.
- Ge, W., Peng, W., Encinas, A., Ruiz, M.F., Song, S., 2019. Preparation and characterization of flowerlike Al-doped Ni(OH)₂ for supercapacitor applications. *Chem. Phys.* 521.
- Li, H.B., Yu, M.H., Wang, F.X., Liu, P., Liang, Y., Xiao, J., Wang, C.X., Tong, Y.X., Yang, G.W., 2013. Amorphous nickel hydroxide nanospheres with ultrahigh capacitance and energy density as electrochemical pseudocapacitor materials. *Nat. Commun.* 4, 1894.
- Li, L., Liu, X., Liu, C., Wan, H., Zhang, J., Liang, P., Wang, Hanbin, Wang, Hao, 2018. Ultra-long life nickel nanowires@nickel-cobalt hydroxide nanoarrays composite pseudocapacitive electrode: Construction and activation mechanism. *Electrochim. Acta* 259, 303–312.
- Liang, H., Lin, J., Jia, H., Chen, S., Qi, J., Cao, J., Lin, T., Fei, W., Feng, J., 2018. Hierarchical NiCo-LDH@NiOOH core-shell heterostructure on carbon fiber cloth as battery-like electrode for supercapacitor. *J. Power Sources* 378, 248–254.
- Peng, W., Li, H., Song, S., 2017. Synthesis of Fluorinated Graphene/CoAl-Layered Double Hydroxide Composites as Electrode Materials for Supercapacitors. *ACS Appl. Mater. Interfaces* 9, 5204–5212.

- Raza, W., Ali, F., Raza, N., Luo, Y., Kim, K.H., Yang, J., Kumar, S., Mehmood, A., Kwon, E.E., 2018. Recent advancements in supercapacitor technology. *Nano Energy* 52, 441–473.
- Su, Y.Z., Xiao, K., Li, N., Liu, Z.Q., Qiao, S.Z., 2014. Amorphous Ni(OH)₂@three-dimensional Ni core-shell nanostructures for high capacitance pseudocapacitors and asymmetric supercapacitors. *J. Mater. Chem. A* 2, 13845–13853.
- Wan, C., Jiao, Y., Li, J., 2017. Multilayer core–shell structured composite paper electrode consisting of copper, cuprous oxide and graphite assembled on cellulose fibers for asymmetric supercapacitors. *J. Power Sources* 361, 122–132.
- Wang, Y., Gai, S., Niu, N., He, F., Yang, P., 2013. Fabrication and electrochemical performance of 3D hierarchical β -Ni(OH)₂ hollow microspheres wrapped in reduced graphene oxide. *J. Mater. Chem. A* 1, 9083.
- Xi, Y., Wei, G., Li, J., Liu, X., Pang, M., Yang, Y., Ji, Y., Izotov, V.Y., Guo, Q., Han, W., 2017. Facile synthesis of MnO₂-Ni(OH)₂ 3D Ridge-like Porous Electrode Materials by Seed-Induce Method for High-performance Asymmetric Supercapacitor. *Electrochim. Acta* 233, 26–35.
- Xu, S., Li, X., Yang, Z., Wang, T., Jiang, W., Yang, C., Wang, S., Hu, N., Wei, H., Zhang, Y., 2016. Nanofoaming to Boost the Electrochemical Performance of Ni@Ni(OH)₂ Nanowires for Ultrahigh Volumetric Supercapacitors. *ACS Appl. Mater. Interfaces* 8, 27868–27876.
- Zhang, L., Hui, K.N., Hui, K.S., Chen, X., Chen, R., Lee, H., 2016. Role of graphene on hierarchical flower-like NiAl layered double hydroxide-nickel foam-graphene as binder-free electrode for high-rate hybrid supercapacitor. *Int. J. Hydrogen Energy* 41, 9443–9453.
- Zhu, Y., Cao, C., Tao, S., Chu, W., Wu, Z., Li, Y., 2014. Ultrathin Nickel Hydroxide and Oxide Nanosheets: Synthesis, Characterizations and Excellent Supercapacitor Performances. *Sci. Rep.* 4, 1–7.

Chapter V. Fabrication of amorphous $\text{Ni}(\text{OH})_2$ @upright self-supported nickel nanowire array with rational architecture

5.1 Material characterization

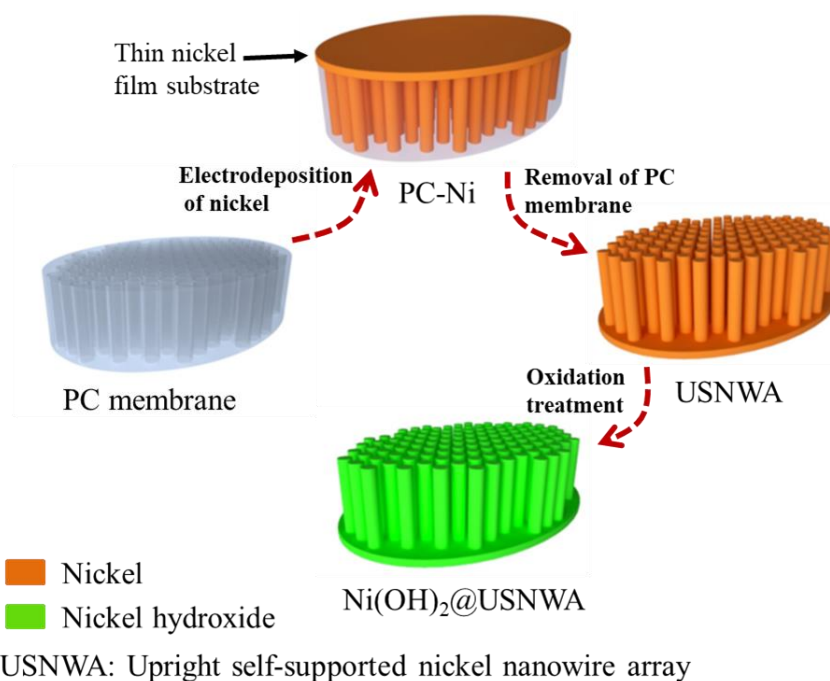


Fig. 5. 1 Schematic illustration of the fabrication process of $\text{Ni}(\text{OH})_2$ @USNWA.

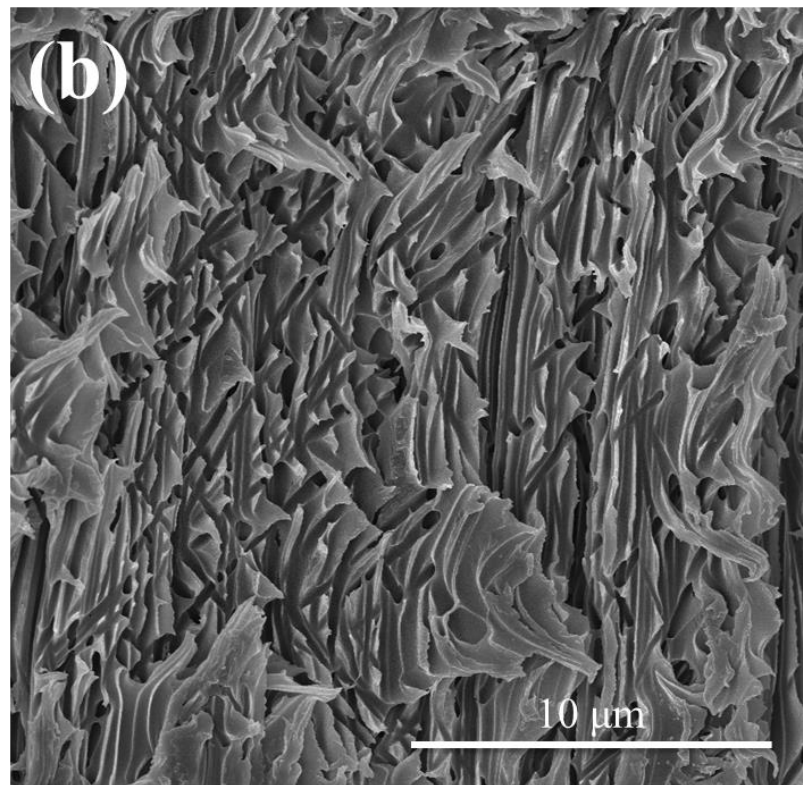
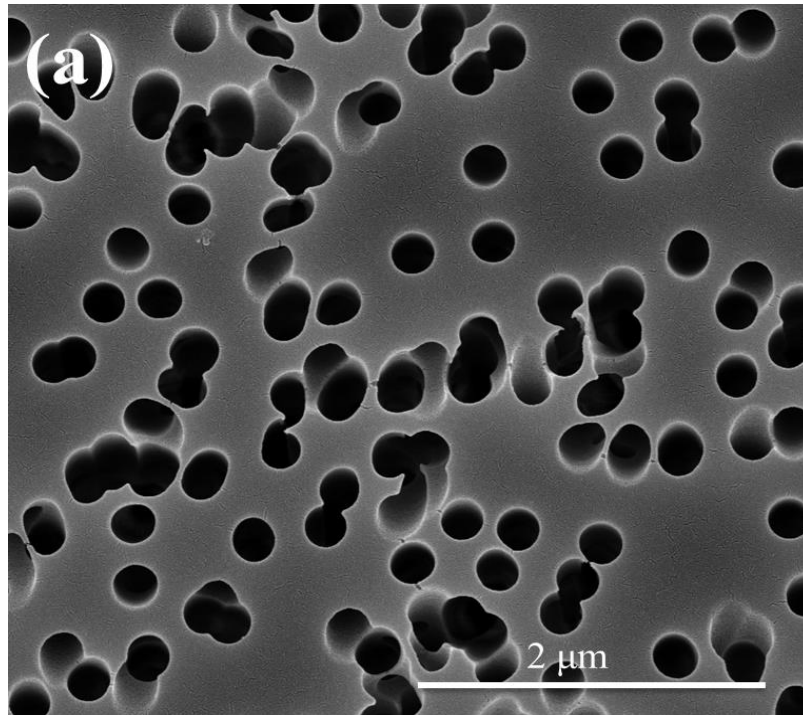
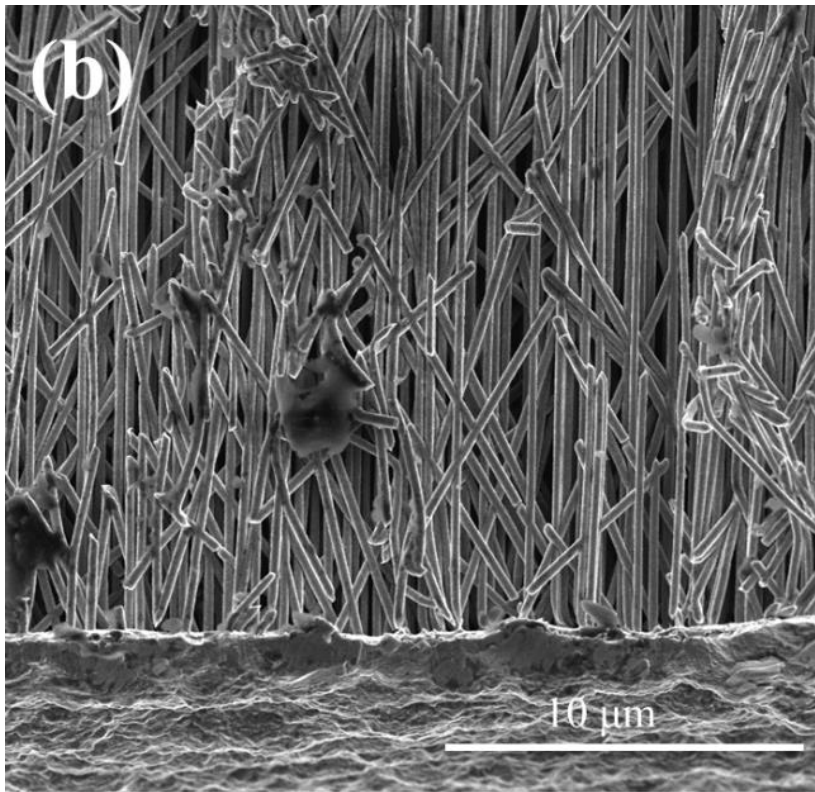
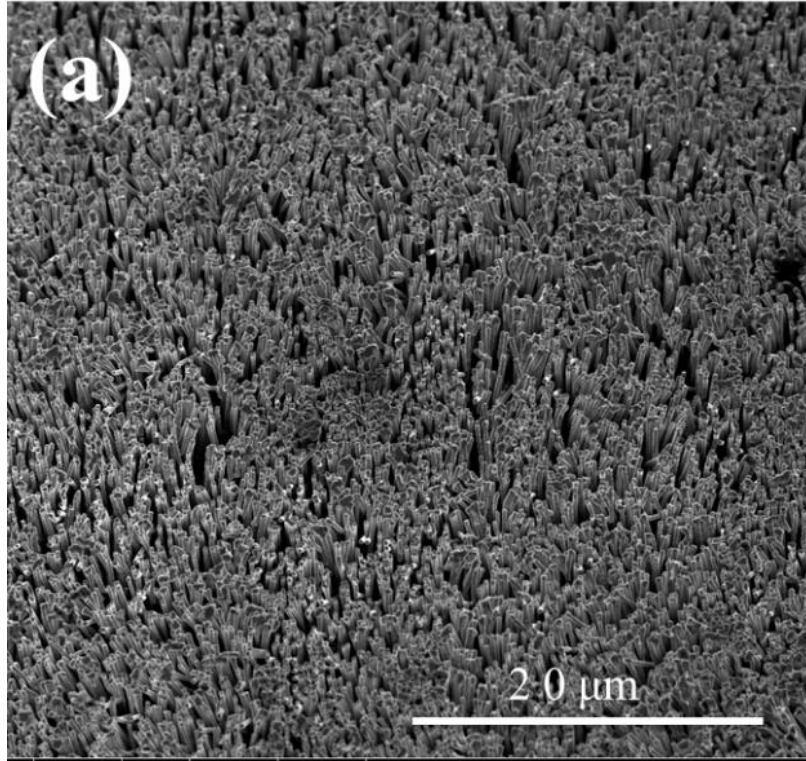
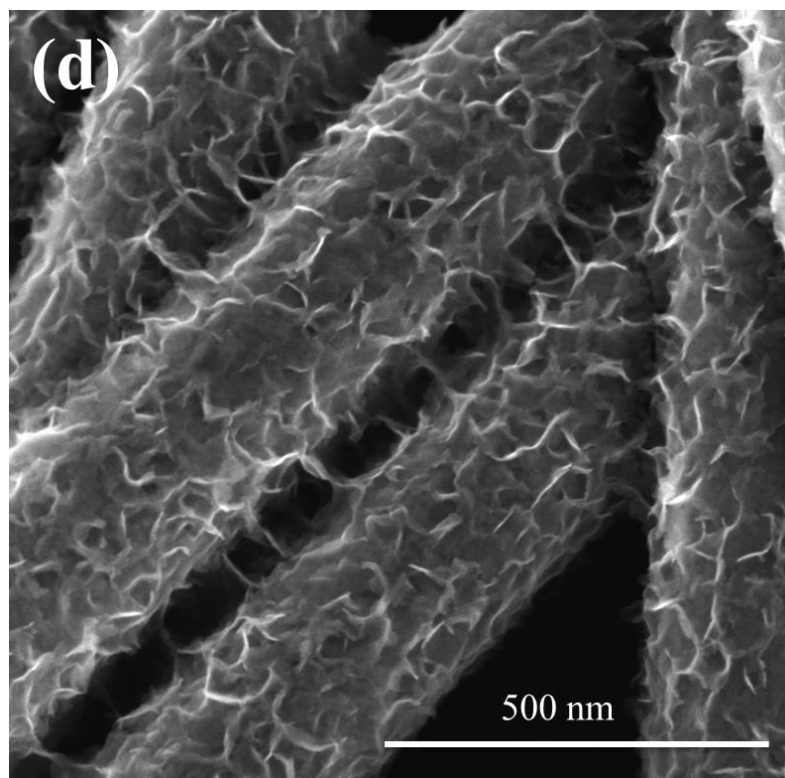
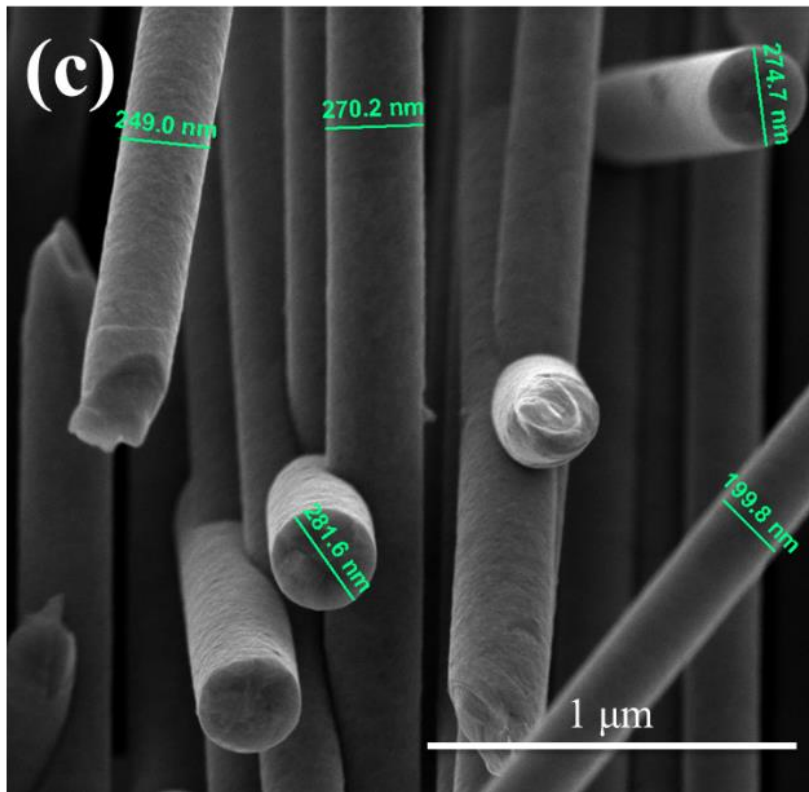


Fig. 5. 2 Micrographs of PC membrane: (a) Surface morphology; (b) Cross-section morphology.

The nanoporous PC membrane was selected as the template for the electrodeposition of nickel nanowire arrays because of its small pore diameter of 0.2 μm , high pore density of 4×10^8 pore cm^{-2} and average pore distance of 530 nm, which is suitable for preparing miniature conductive scaffold. Fig. 5.1 shows the fabrication process of $\text{Ni(OH)}_2@$ USNWA. In the electrodeposition process, metallic nickel grew in the pore from bottom to the top of PC membrane. When the nickel grew to the membrane surface, a thin film began to form on the PC membrane surface. The thin nickel film acts as a substrate to support all the nanowires to keep self-supported structure and ensures good electrical conductivity. After electrodeposition process, the PC membrane was dissolved to obtain USNWA. Then, the USNWA was oxidized to have Ni(OH)_2 on its surface.

Fig. 5.2 shows the microstructure of the PC template. As shown in Fig. 5.2(a), a large number of circular pores distribute on the membrane surface. From the cross-section morphology as shown in Fig. 5.2(b), a great quantity of straight pore channels with small diameters can be observed, which demonstrates the high pore density of PC template. Most of the pore channels are upright, only a small number of the pore channels are inclined and intersect with the upright pore channels.





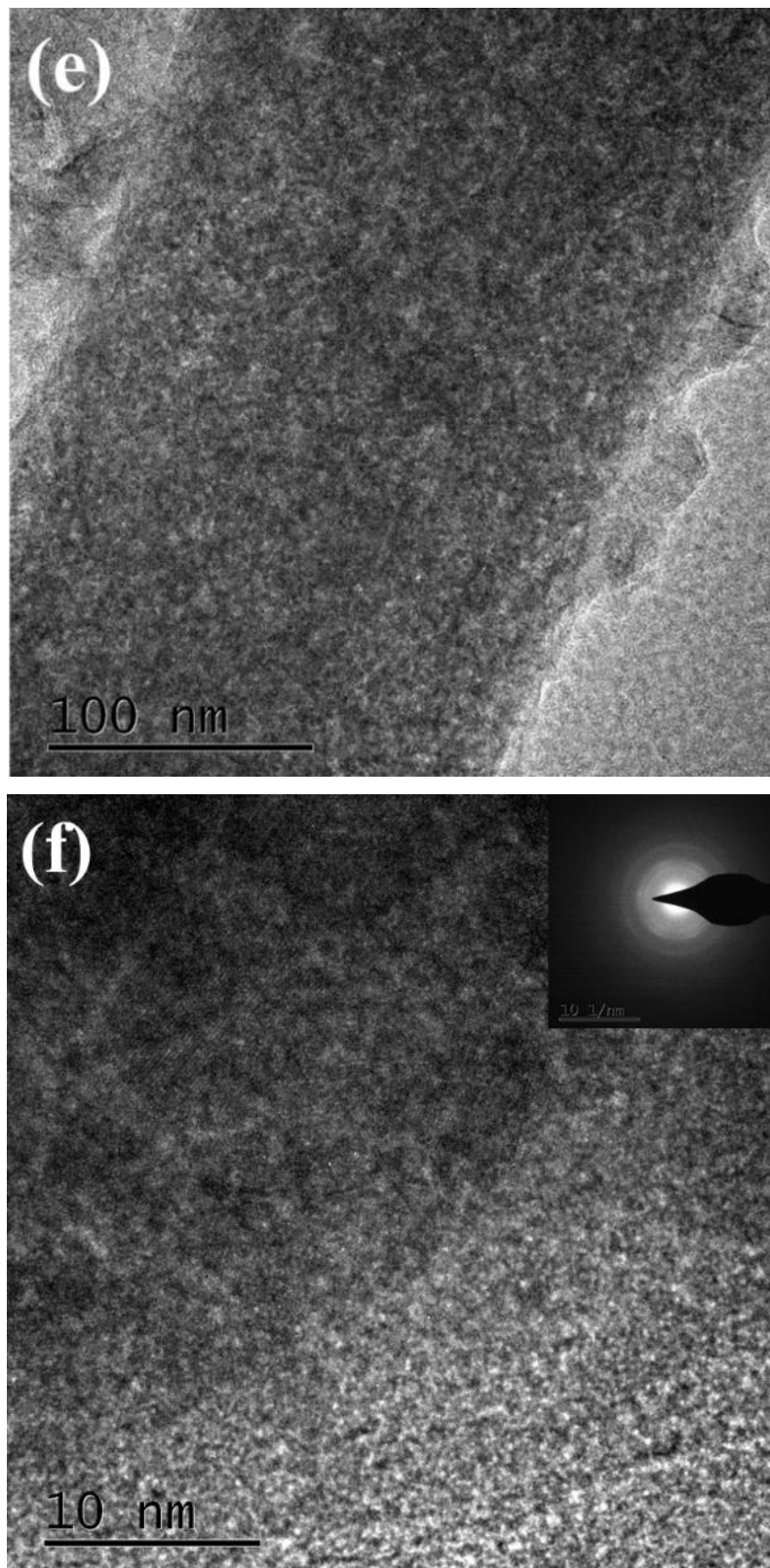


Fig. 5. 3 Microstructure of USNWA and $\text{Ni}(\text{OH})_2@USNWA$:(a) Surface morphology of USNWA, (b-c) Cross-section morphology of USNWA, (d) SEM image of $\text{Ni}(\text{OH})_2@USNWA$, (e) TEM image of $\text{Ni}(\text{OH})_2@USNWA$, (f) HRTEM image of $\text{Ni}(\text{OH})_2@USNWA$.

Fig. 5.3 shows the microstructure of the USNWA. From the surface morphology as shown in Fig. 5.3(a), a nickel nanowire array with a high wire density is observed. Because the wire density of USNWA corresponds to the pore density of the PC template, according to the pore parameters of the PC template, the wire density of the USNWA is 4×10^8 wire cm^{-2} . The 3D self-supported nickel nanowire array can be observed from the cross-section morphology as shown in Fig. 5.3(b). Most of the nanowires are upright, and a small number of nanowires are inclined, and interconnect with the upright nanowires, which is consistent with the pore structure of the PC template, shown in Fig. 5.2(b). At the bottom of the nickel nanowire array, a thin nickel film supports all the nanowires to maintain a self-supported structure, and makes all the nanowires form a 3D conductive scaffold. As shown in Fig. 5.3(c) the diameters of the nickel wires are about 250 nm. Therefore, according to the average pore distance and wire diameter, the average wire spacing is about 280 nm. The small wire diameter and wire spacing allow the USNWA to have a larger surface area per unit volume than that of the common 3D conductive scaffolds used in electrodes of supercapacitors. Fig. 5.3(d) shows the morphology of $\text{Ni}(\text{OH})_2$ @USNWA. It can be seen that nickel hydroxide uniformly covers all the surfaces of the nanowires after oxidation treatment, which demonstrates the core-shell structure of $\text{Ni}(\text{OH})_2$ @USNWA. Because it is converted from the metallic surface of USNWA, the $\text{Ni}(\text{OH})_2$ is in stable contact with the nickel nanowires, creating a stable core-shell structure and a low interfacial resistance. Fig. 5.3(e) shows the HRTEM image of $\text{Ni}(\text{OH})_2$ @USNWA, which further demonstrates that the wire diameters are about 250 nm. Fig. 5.3(f) presents the HR-TEM image of $\text{Ni}(\text{OH})_2$ @USNWA, and the corresponding selected-area electron diffraction (SAED) pattern in the inset exhibits a broad and diffused halo ring indicating that the $\text{Ni}(\text{OH})_2$ is amorphous (Liu and Li, 2009; Nguyen et al., 2017).

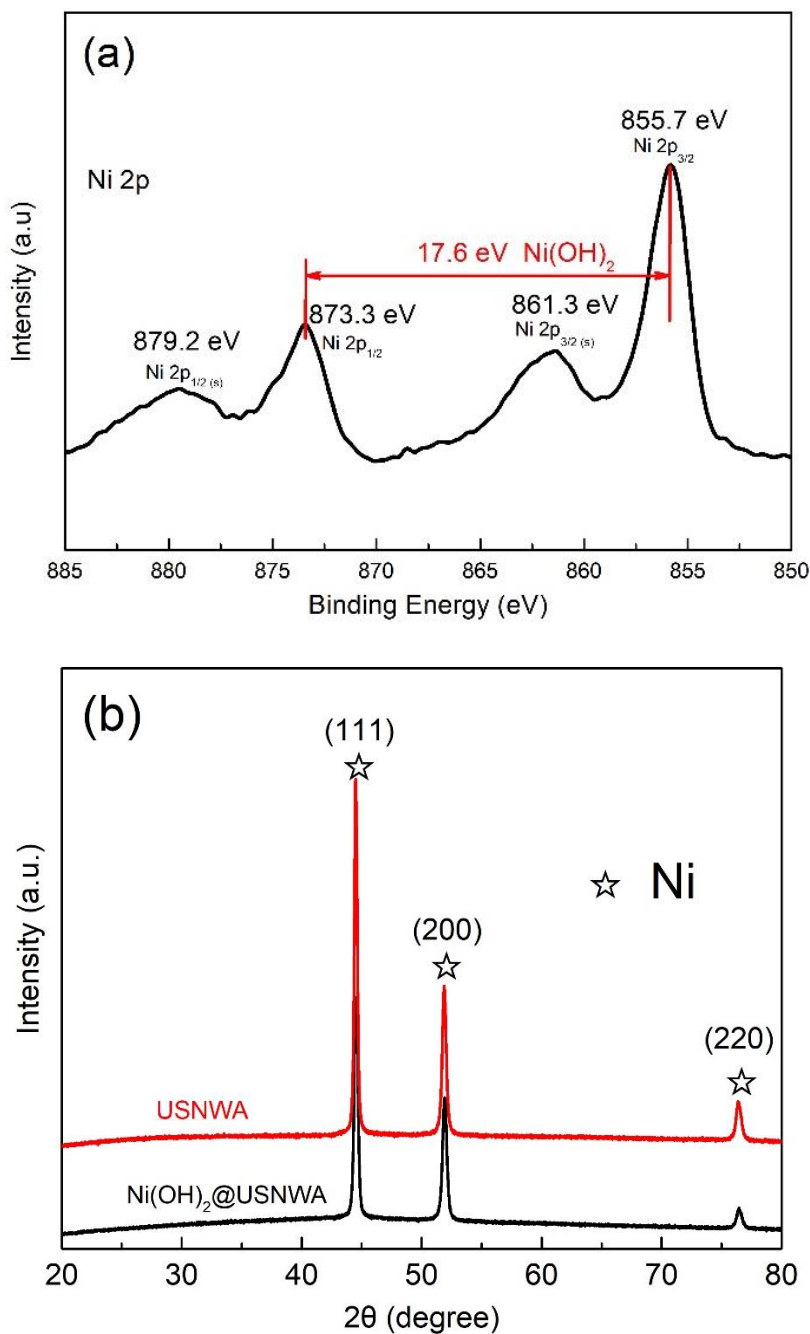
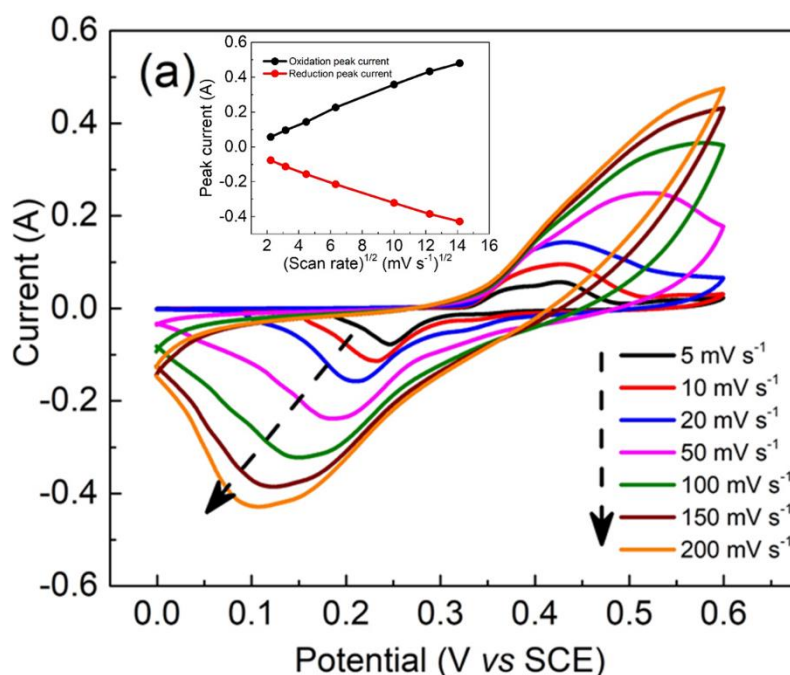


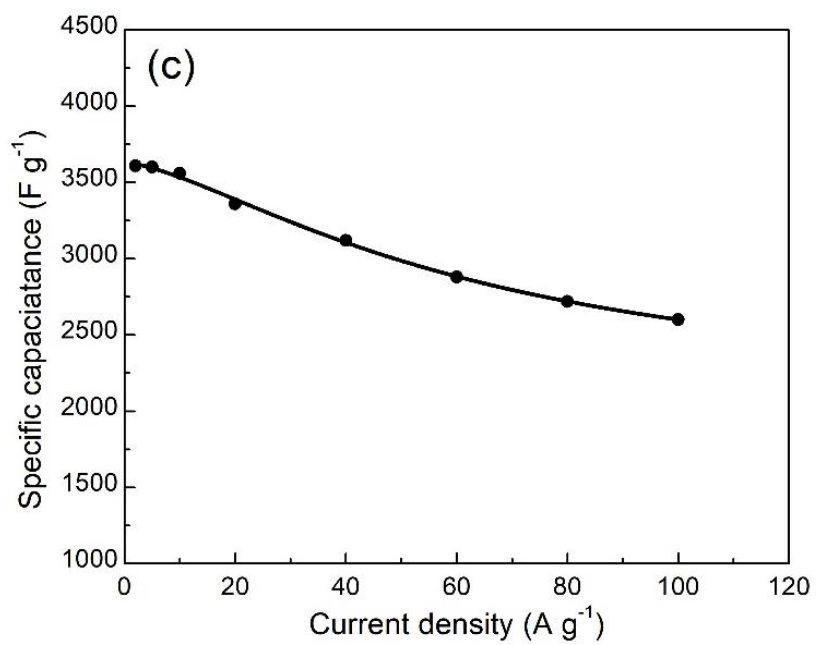
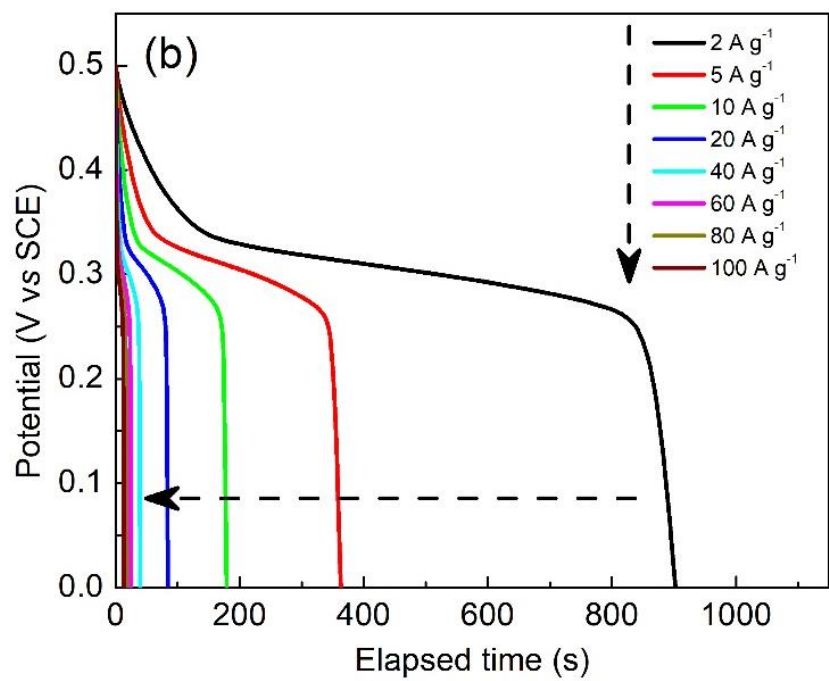
Fig. 5. 4 (a) Ni 2p XPS result of Ni(OH)₂@USNWA; (b) XRD patterns of USNWA and Ni(OH)₂@USNWA.

The crystallographic structure and chemical composition of Ni(OH)₂@USNWA were characterized by XRD and XPS, respectively. Fig 5.4(a) shows the Ni 2p XPS result. Two main peaks locate at around 855.7 and 873.3 eV corresponding to Ni 2p_{3/2} and Ni 2p_{1/2}, respectively (Li et al., 2013a). The other two peaks locate at 879.2

and 861.3 eV corresponding to the Ni 2p_{1/2} and Ni 2p_{3/2} satellites, respectively. The spin-orbit splitting energy value of Ni 2p_{1/2} and Ni 2p_{3/2} is 17.6 eV, which is the characteristic of Ni(OH)₂ phase (Li et al., 2016). Therefore, the XPS results demonstrate the formation of Ni(OH)₂ on the nickel nanowire surface. Fig. 5.4(b) exhibits the XRD patterns of USNWA and Ni(OH)₂@USNWA. On the pattern of USNWA, there are three main peaks at 44.80°, 52.75° and 77.52° corresponding to (111), (200) and (220) Bragg's reflections of monoclinic Ni phase (JCPDS 04-850), respectively (Guan et al., 2017; Kong et al., 2011). However, on the curves of Ni(OH)₂@USNWA, there are only three peaks locating at the same positions of nickel, which indicates that the Ni(OH)₂ generated by the oxidation treatment is amorphous.

5.2 Electrochemical characterization





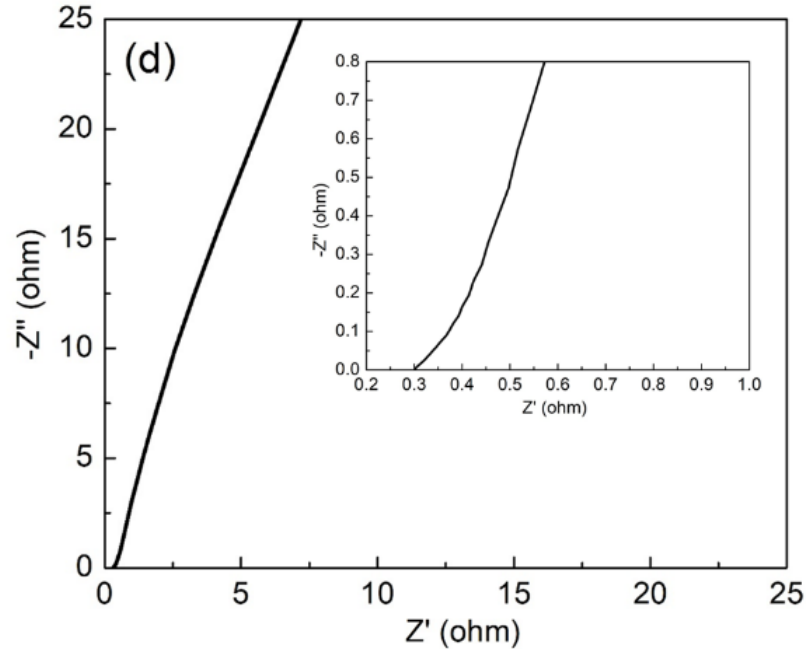


Fig. 5.5 Electrochemical performance of Ni(OH)₂@USNWA: (a) CV curves measured at different scan rates; (b) Discharge curves at different current densities; (c) Specific capacitance as a function of current density; (d) EIS result measured in the frequency range of 10⁵-10⁻² Hz.

Fig. 5.5(a) presents the CV curves of Ni(OH)₂@USNWA measured in the potential window of 0-0.6 V (vs SCE) at scan rates from 5 to 200 mV s⁻¹. On each curve, a pair of well-defined redox peaks are clearly observed, which corresponds to the reversible redox reaction between Ni²⁺/Ni³⁺ and OH⁻¹ anions (Xu et al., 2015). The strong redox peaks demonstrate that the energy-storage mechanism of Ni(OH)₂@USNWA is mainly attributed to the Faradic redox reactions. The peak current increases linearly with the increase in the square root of scan rate from 5 to 200 mV s⁻¹ suggesting the high reversibility of the redox reactions. Galvanostatic charge/discharge measurements were carried out at different current densities from 2 to 100 A g⁻¹, and the discharge curves in the potential range of 0-0.5 V are shown in Fig. 5.5(b). Each discharge curve has a slow potential decay, which is caused by the Faradic redox reactions (Chai et al., 2017; Peng et al., 2017). The calculated specific capacitance from the corresponding discharge curve as a function of discharge current density is shown in Fig. 5.5(c). At a current density of 2 A g⁻¹, the Ni(OH)₂@USNWA shows an ultrahigh specific capacitance of 3600 F g⁻¹. The high specific capacitance indicates the high utilization of amorphous Ni(OH)₂, which may

result from the amorphous structure that a large number of electroactive sites to the electrolyte (Inamdar et al., 2011; Li et al., 2013b; Wang et al., 2015; Xu et al., 2016). At the current densities of 20, 60, 80 and 100 A g⁻¹, the specific capacitances are 3360, 2880, 2720 and 2600 F g⁻¹, respectively. Therefore, as the current density increase sharply, the specific capacitance decreases slowly, which further demonstrates the excellent rate capability of Ni(OH)₂@USNWA at high current densities.

EIS was performed in the frequency range 10⁵-10⁻² Hz to study the charge and ion transport kinetics of Ni(OH)₂@USNWA, which are the two main factors affecting the rate capability (Zhang and Pan, 2015). Fig. 5.5(d) shows that the Nyquist plot of Ni(OH)₂@USNWA only contains a nearly straight line in the tested frequency range. At high frequencies, the intercept at real part (Z') is recognized as serial resistance (R_s) composed of the bulk electrolyte resistance, the intrinsic resistance of active material and the contact resistance between the nickel wire (core) and Ni(OH)₂ (shell) (Vidhyadharan et al., 2014). The Ni(OH)₂@USNWA has a small R_s of 0.3 Ω , indicating that the Ni(OH)₂@USNWA has superior electrical conductivity. The excellent electrical conductivity can be attributed to the self-supported nickel nanowire array as 3D conductive scaffold (core material) and the stable contact between Ni(OH)₂ and wire surface. Normally, the Nyquist plot of a supercapacitor electrode has a semicircle in the high-middle frequency region, and its diameter stands for the charge-transfer resistance (R_{ct}) caused by the Faradic redox reactions (Iqbal et al., 2018). The absence of the semicircle on the plot of Ni(OH)₂@USNWA suggests that the charge-transfer resistance is too low to detect. The slope of the straight line in the low-frequency region characterizes the Warburg impedance (Z_w), which is related to the diffusion of electrolyte ions (Zheng et al., 2016). The straight line with a slope of about 5 demonstrates that the Ni(OH)₂@USNWA has a low ion diffusion resistance, which may result from the advantages of amorphous Ni(OH)₂ and the nanowire array structure.

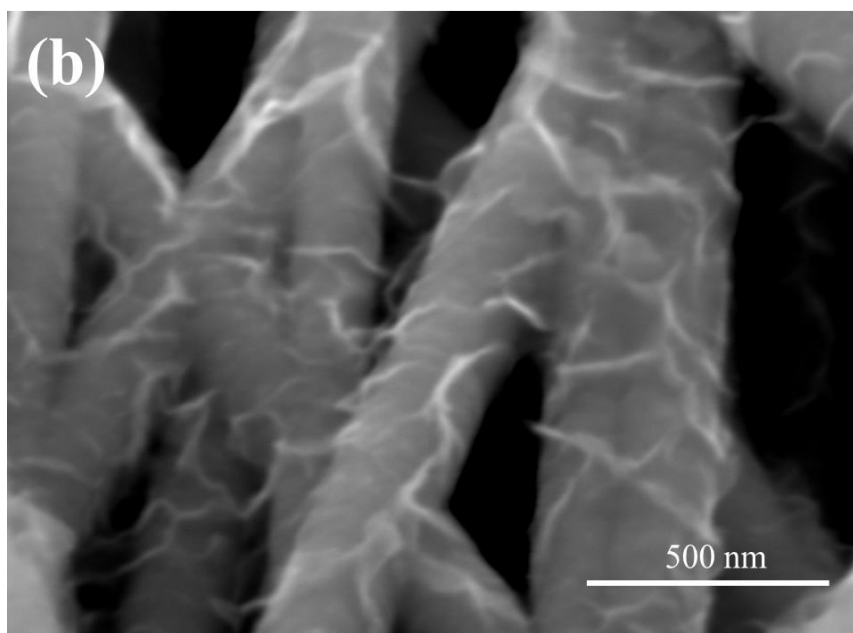
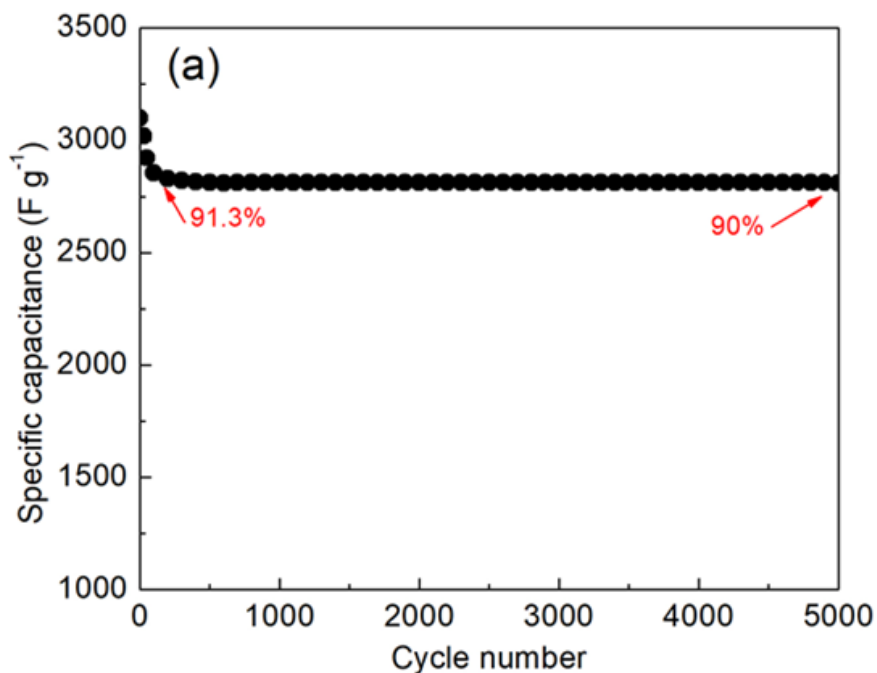


Fig. 5. 6 (a) Cyclic performance of Ni(OH)₂@USNWA at a current density of 20 A g⁻¹; (b) Morphology of Ni(OH)₂@USNWA after cycling test.

The cyclic stability of Ni(OH)₂@USNWA at high current density can precisely reflect the service life for practical applications. The cyclic stability was tested at a constant current density of 20 A g⁻¹ in the potential range of 0-0.5 V for 5000 cycles, and the results are shown in Fig. 5.6. The specific capacitance of Ni(OH)₂@USNWA gradually decreases from 3100 to 2830 F g⁻¹ during the first 200 cycles. Then, the

specific capacitance slowly decreases to 90 % of the initial capacitance in the subsequent cycles, exhibiting a remarkable electrochemical stability during the charge/discharge process at a high current density. After cycling test, the morphology of Ni(OH)₂@USNWA is shown in Fig. 5.6(b). It can be seen that the Ni(OH)₂ still covers the surface of the nickel nanowires after long cycling test, further confirming the superior cycling stability.

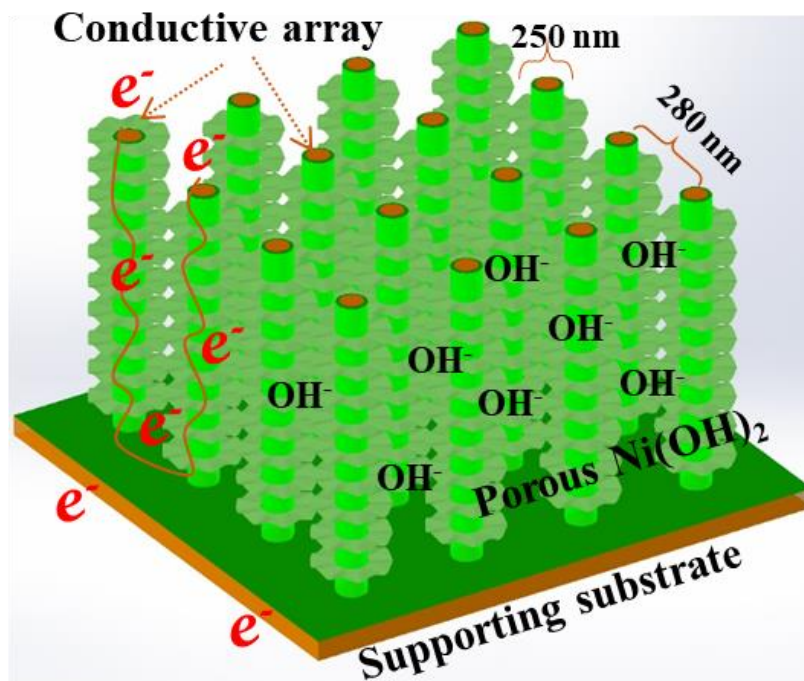


Fig. 5. 7 Schematic illustration of the structural advantages of Ni(OH)₂@USNWA.

The Ni(OH)₂@USNWA with a miniature conductive scaffold presents excellent electrochemical performance of a high specific capacitance, remarkable rate capability and superior cycling stability. The excellent electrochemical performance can be ascribed to the structural merits of amorphous Ni(OH)₂@USNWA, as illustrated in Fig. 5.7. The USNWA as a miniature conductive scaffold provides high electrical conductivity and short pathways for rapid charge transfer and fast diffusion of electrolyte ions, respectively. The amorphous Ni(OH)₂ has a high utilization for energy storage, and the stable contact between Ni(OH)₂ and nickel wire contributes to a low interfacial resistance.

5.3 Conclusions

In summary, Ni(OH)₂@self-supported nickel nanowire arrays with high wire density and stable core-shell structure were successfully fabricated by a simple process of template-directed electrodeposition and surface oxidation. The self-supported nickel nanowire array has small wire diameters about 250 nm and average wire spacing of 280 nm, which result in good electrical conductivity and a larger surface area per volume than that of common used conductive scaffolds in supercapacitors. The Ni(OH)₂ as shell material is in stable contact with the highly conductive nickel nanowires. Due to its self-supported and integrated core-shell structural advantages, the Ni(OH)₂@USNWA shows excellent electrochemical performance at high current densities, which make it promising for supercapacitor applications.

References

- Chai, H., Peng, X., Liu, T., Su, X., Jia, D., Zhou, W., 2017. High-performance supercapacitors based on conductive graphene combined with Ni(OH)₂ nanoflakes. *RSC Adv.* 7, 36617–36622.
- Guan, W., Tian, S., Cao, D., Chen, Y., Zhao, X., 2017. Electrooxidation of nickel-ammonia complexes and simultaneous electrodeposition recovery of nickel from practical nickel-electroplating rinse wastewater. *Electrochim. Acta* 246, 1230–1236.
- Inamdar, A.I., Sonavane, A.C., Pawar, S.M., Kim, Y., Kim, J.H., Patil, P.S., Jung, W., Im, H., Kim, D.Y., Kim, H., 2011. Electrochromic and electrochemical properties of amorphous porous nickel hydroxide thin films. *Appl. Surf. Sci.* 257, 9606–9611.
- Iqbal, M.F., Ashiq, M.N., Hassan, M.U., Nawaz, R., Masood, A., Razaq, A., 2018. Excellent electrochemical behavior of graphene oxide based aluminum sulfide nanowalls for supercapacitor applications. *Energy* 159, 151–159.
- Kong, D.S., Wang, J.M., Shao, H.B., Zhang, J.Q., Cao, C.N., 2011. Electrochemical fabrication of a porous nanostructured nickel hydroxide film electrode with superior pseudocapacitive performance. *J. Alloys Compd.* 509, 5611–5616.
- Li, H.B., Liu, P., Liang, Y., Xiao, J., Yang, G.W., 2013a. Amorphous nickel hydroxide nanospheres by a green electrochemistry technique: Structure, morphology and magnetism. *CrystEngComm* 15, 4054–4057.

- Li, H.B., Yu, M.H., Wang, F.X., Liu, P., Liang, Y., Xiao, J., Wang, C.X., Tong, Y.X., Yang, G.W., 2013b. Amorphous nickel hydroxide nanospheres with ultrahigh capacitance and energy density as electrochemical pseudocapacitor materials. *Nat. Commun.* 4, 1–7.
- Li, S., Wen, J., Chen, T., Xiong, L., Wang, J., Fang, G., 2016. In situ synthesis of 3D CoS nanoflake/Ni(OH)₂ nanosheet nanocomposite structure as a candidate supercapacitor electrode. *Nanotechnology* 27.
- Liu, C., Li, Y., 2009. Synthesis and characterization of amorphous α -nickel hydroxide. *J. Alloys Compd.* 478, 415–418.
- Nguyen, T., Boudard, M., João Carmezim, M., Fátima Montemor, M., 2017. Ni_xCo_{1-x}(OH)₂ nanosheets on carbon nanofoam paper as high areal capacity electrodes for hybrid supercapacitors. *Energy* 126, 208–216.
- Peng, W., Li, H., Song, S., 2017. Synthesis of Fluorinated Graphene/CoAl-Layered Double Hydroxide Composites as Electrode Materials for Supercapacitors. *ACS Appl. Mater. Interfaces* 9, 5204–5212.
- Vidhyadharan, B., Zain, N.K.M., Misnon, I.I., Aziz, R.A., Ismail, J., Yusoff, M.M., Jose, R., 2014. High performance supercapacitor electrodes from electrospun nickel oxide nanowires. *J. Alloys Compd.* 610, 143–150.
- Wang, D., Kong, L. Bin, Liu, M.C., Zhang, W. Bin, Luo, Y.C., Kang, L., 2015. Amorphous Ni-P materials for high performance pseudocapacitors. *J. Power Sources* 274, 1107–1113.
- Xu, S., Li, X., Yang, Z., Wang, T., Jiang, W., Yang, C., Wang, S., Hu, N., Wei, H., Zhang, Y., 2016. Nanofoaming to Boost the Electrochemical Performance of Ni@Ni(OH)₂ Nanowires for Ultrahigh Volumetric Supercapacitors. *ACS Appl. Mater. Interfaces* 8, 27868–27876.
- Xu, S., Li, X., Yang, Z., Wang, T., Xu, M., Zhang, L., Yang, C., Hu, N., He, D., Zhang, Y., 2015. A novel Ni@Ni(OH)₂ coaxial core-sheath nanowire membrane for electrochemical energy storage electrodes with high volumetric capacity and excellent rate capability. *Electrochim. Acta* 182, 464–473.
- Zhang, S., Pan, N., 2015. Supercapacitors performance evaluation. *Adv. Energy Mater.* 5, 1–19.
- Zheng, C.H., Yao, T., Xu, T.R., Wang, H.A., Huang, P.F., Yan, Y., Fang, D.L., 2016. Growth of ultrathin Ni-Co-Al layered double hydroxide on reduced graphene oxide and superb supercapacitive performance of the resulting composite. *J. Alloys Compd.* 678, 93–101.

Chapter VI. Fabrication of amorphous $\text{Ni}(\text{OH})_2$ @interconnected nickel nanowire array with rational architecture

6.1 Material characterization

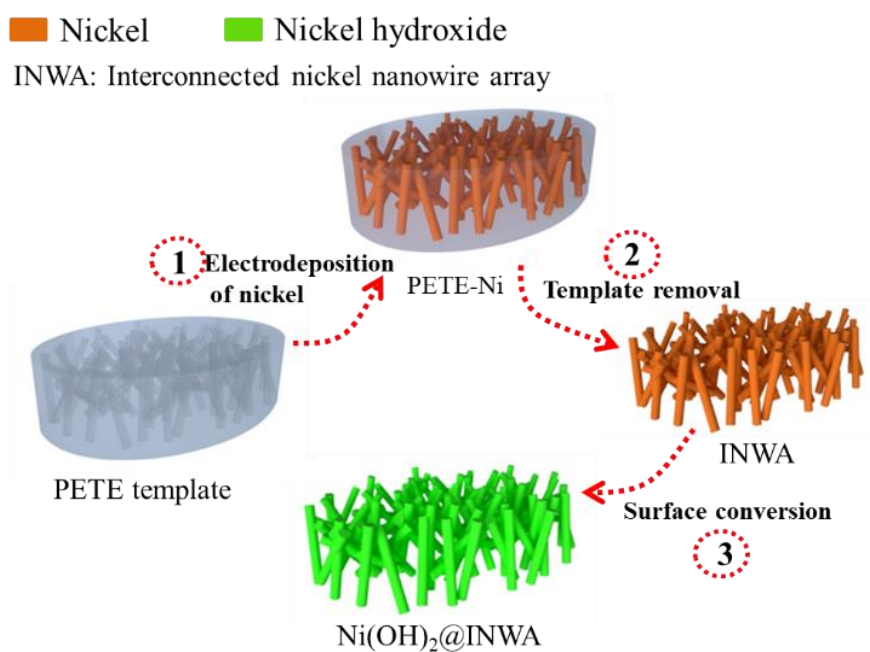


Fig. 6. 1 Schematic illustration of the fabrication process of $\text{Ni}(\text{OH})_2$ @INWA through template-directed electrodeposition and surface conversion.

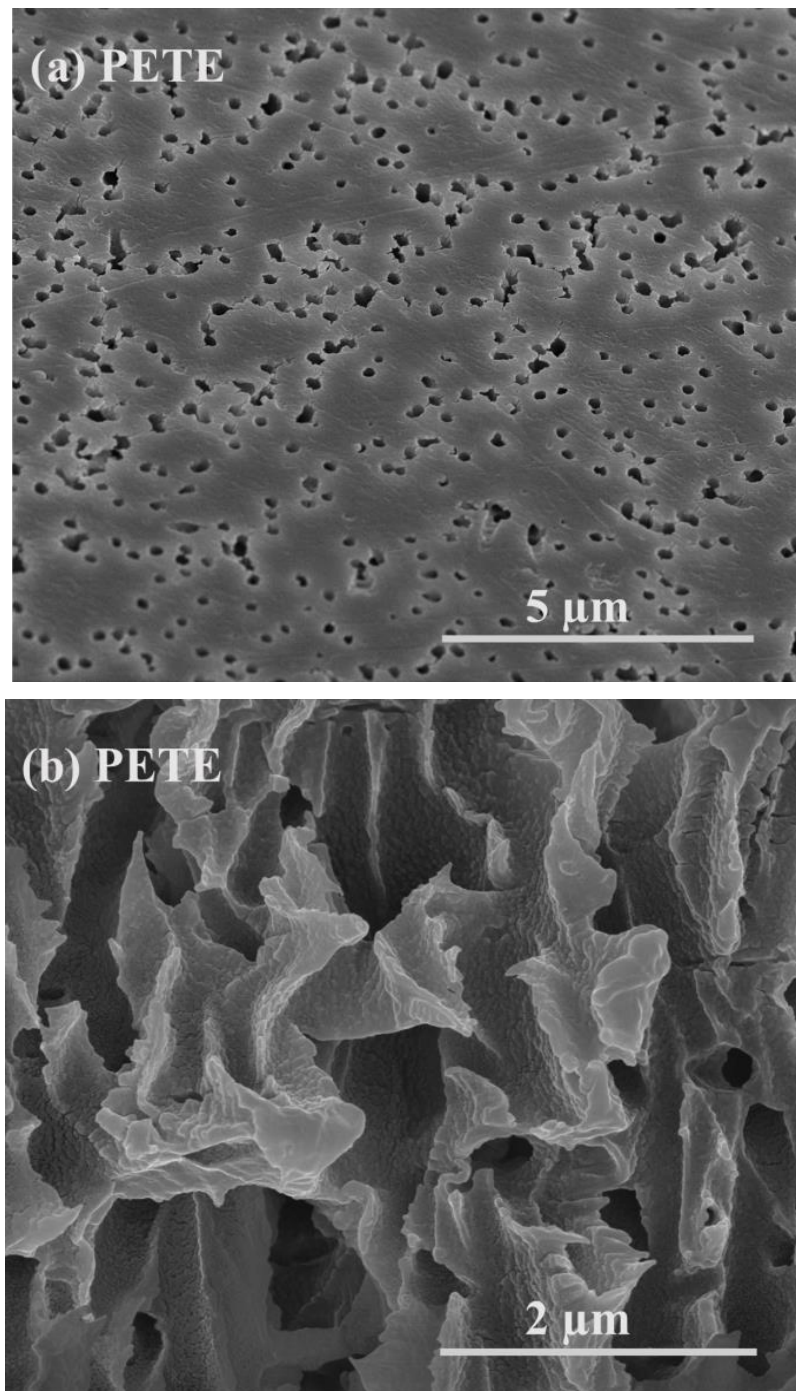
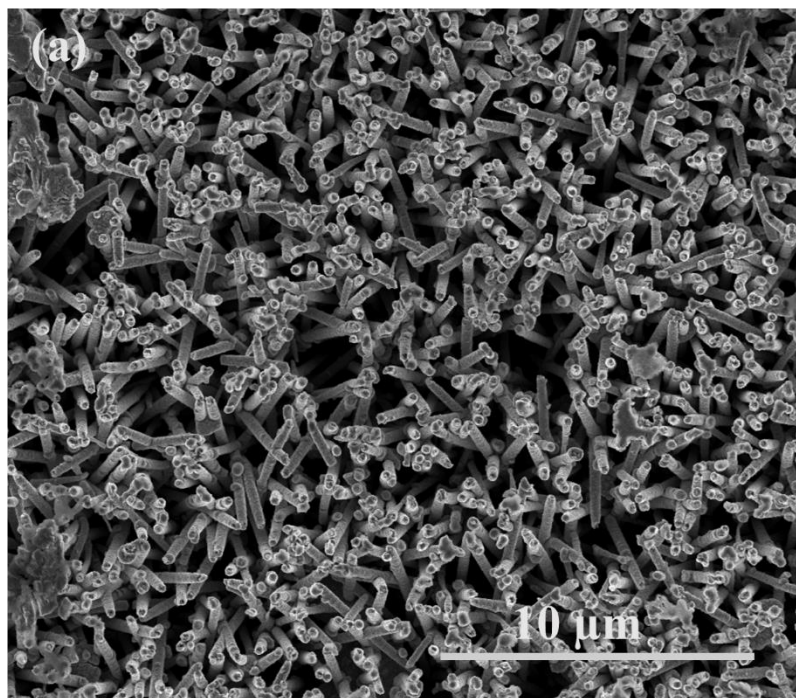
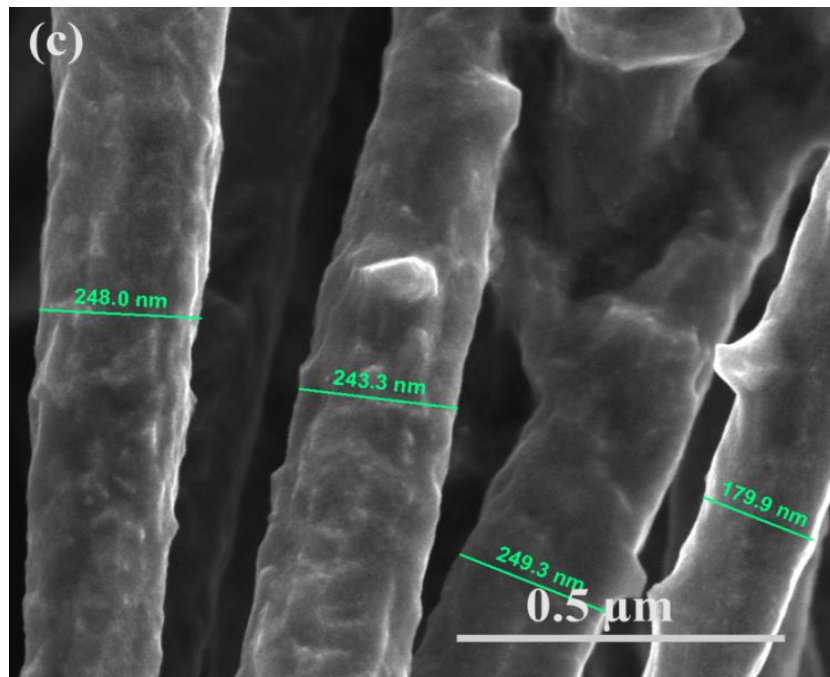
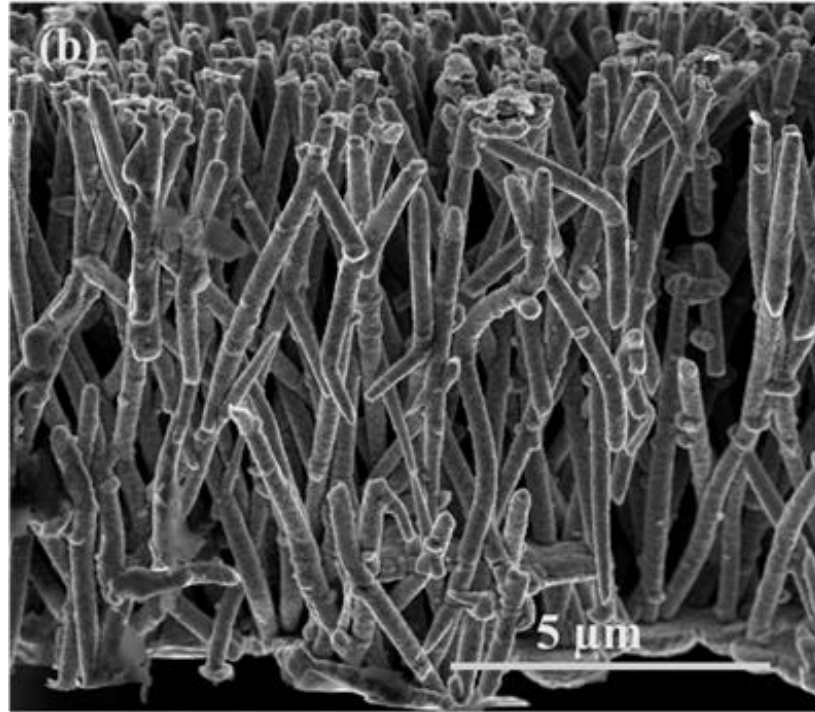


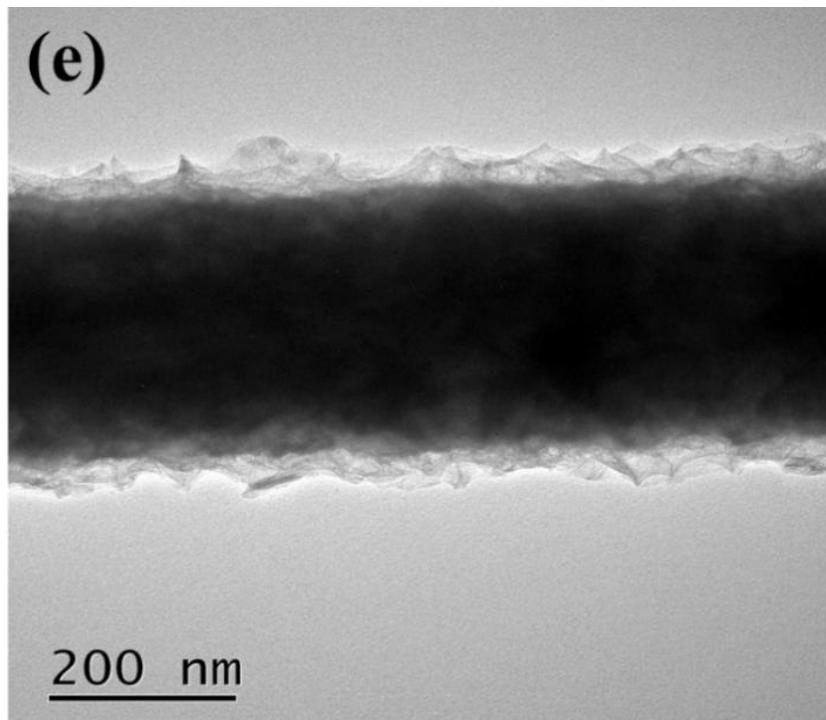
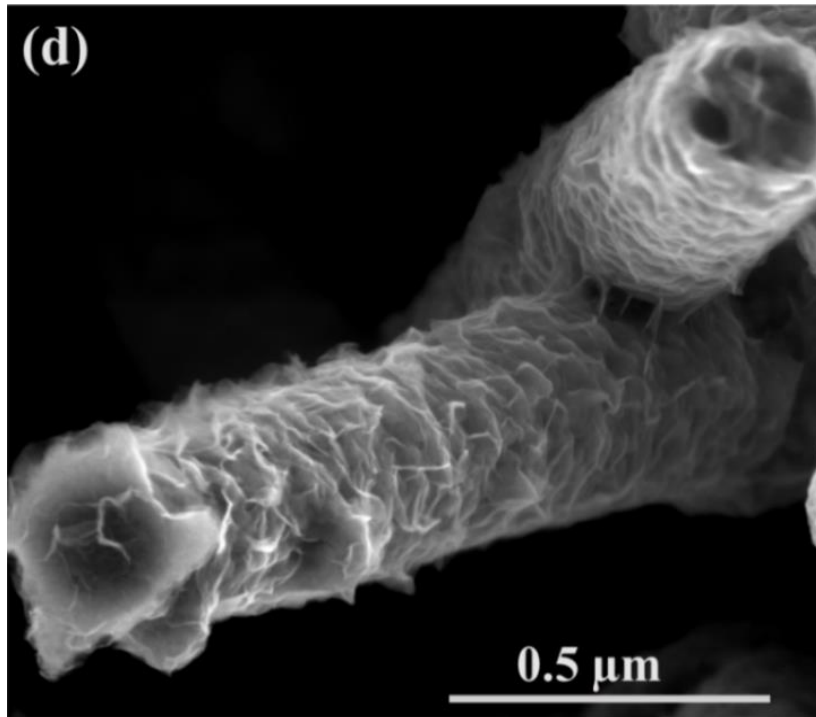
Fig. 6. 2 Micrographs of the PETE membrane: (a) Surface morphology; (b) Cross-section morphology.

Fig. 6.1 illustrates the fabrication process of $\text{Ni}(\text{OH})_2@$ INWA using the process of template-directed electrodeposition and surface conversion. First, the INWA was prepared by electrodepositing metallic nickel into the pores of PETE

membrane, then dissolving the membrane. Amorphous $\text{Ni}(\text{OH})_2$ coating on the wire surface of INWA was prepared by direct conversion of the metallic surface of INWA into $\text{Ni}(\text{OH})_2$ through an oxidation treatment. Porous PETE membrane was used as the template for electrodeposition because of its high pore density of 3×10^8 pore cm^{-2} and interconnected pore structure, which allows obtaining a self-supported array with a high wire density. Fig. 6.2 shows the surface and cross-section morphologies of PETE template. As shown in Fig. 6.2(a), a large number of pores randomly distribute on the surface of PETE membrane. From the cross-section morphology as shown in Fig. 6.2(b), abundant interconnected pores can be observed, which confirms the interconnected pore structure.







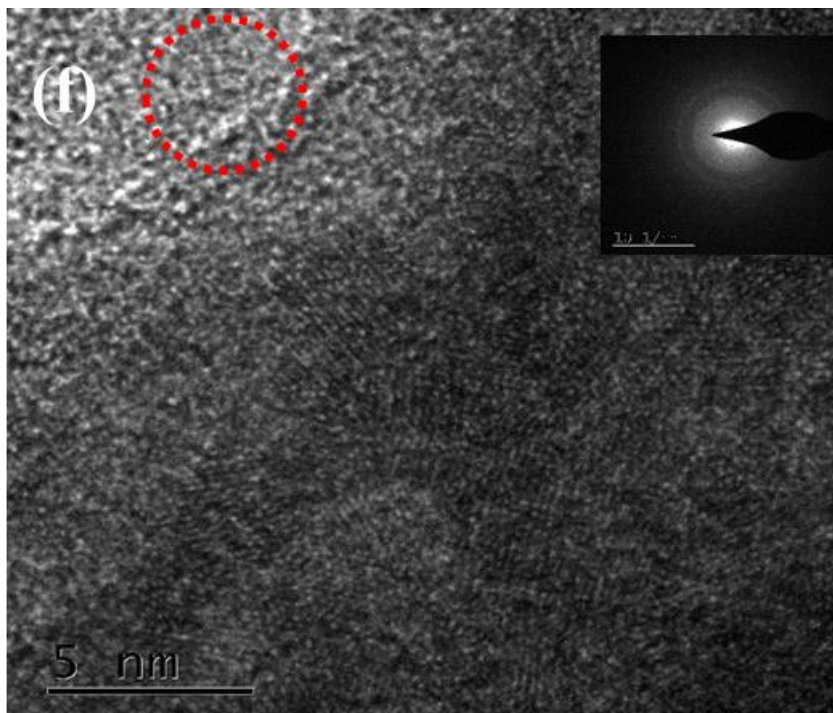
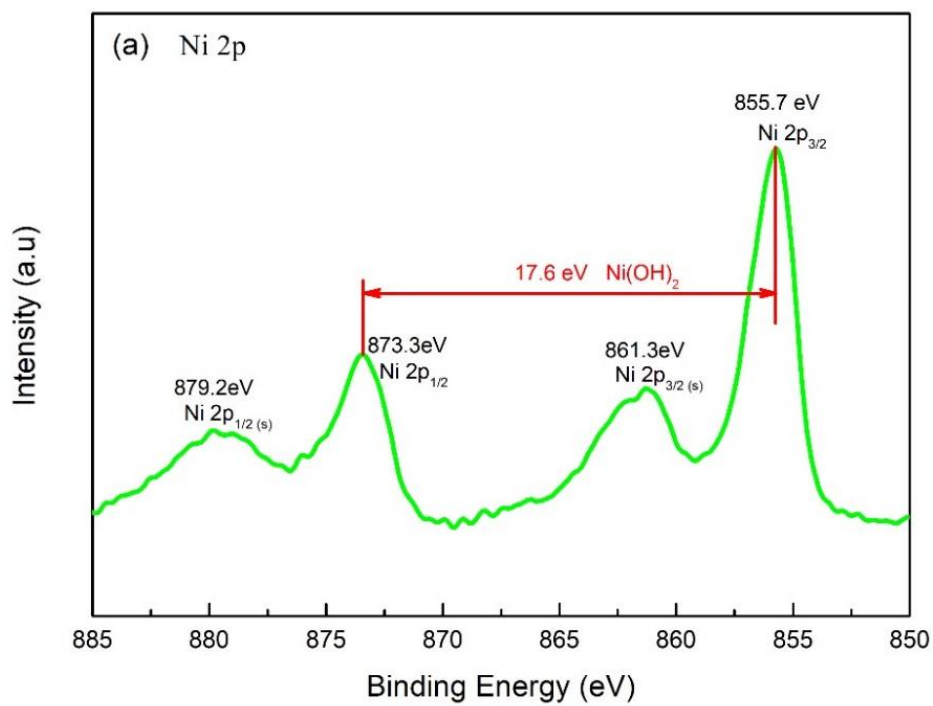


Fig. 6. 3 SEM images of INWA: (a) Surface morphology, (b-c) Cross-section morphology. (d) SEM image of Ni(OH)₂@INWA; (e) TEM image of Ni(OH)₂@INWA; (f) HRTEM image of Ni(OH)₂@INWA.



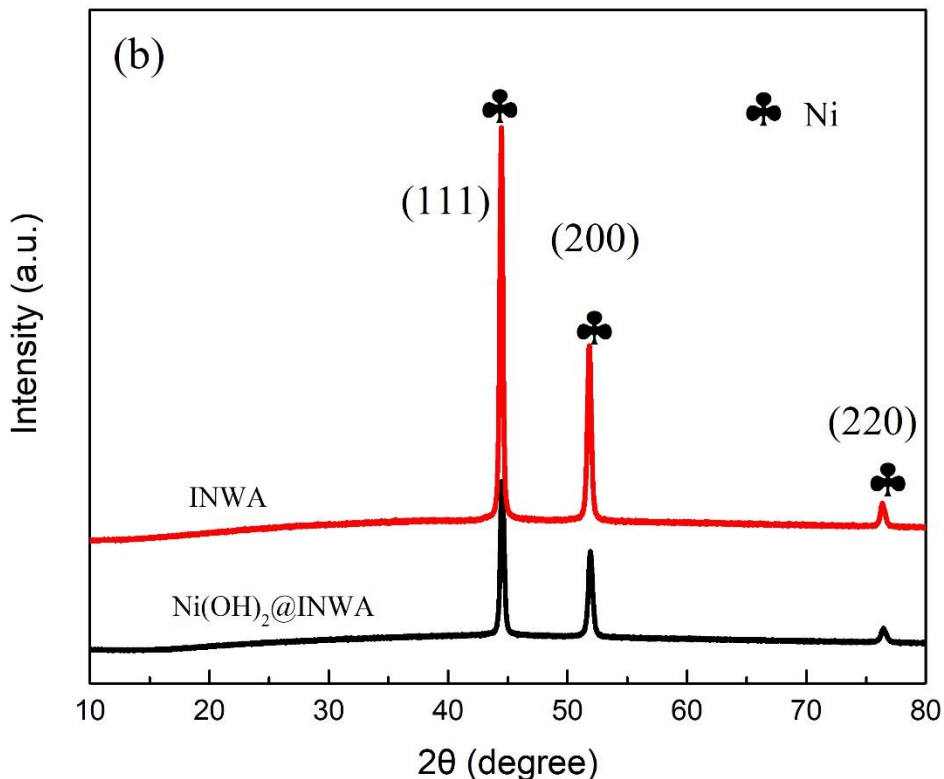


Fig. 6. 4 (a) Ni 2p XPS spectrum of Ni(OH)₂@INWA; (b) XRD patterns of INWA and Ni(OH)₂@INWA.

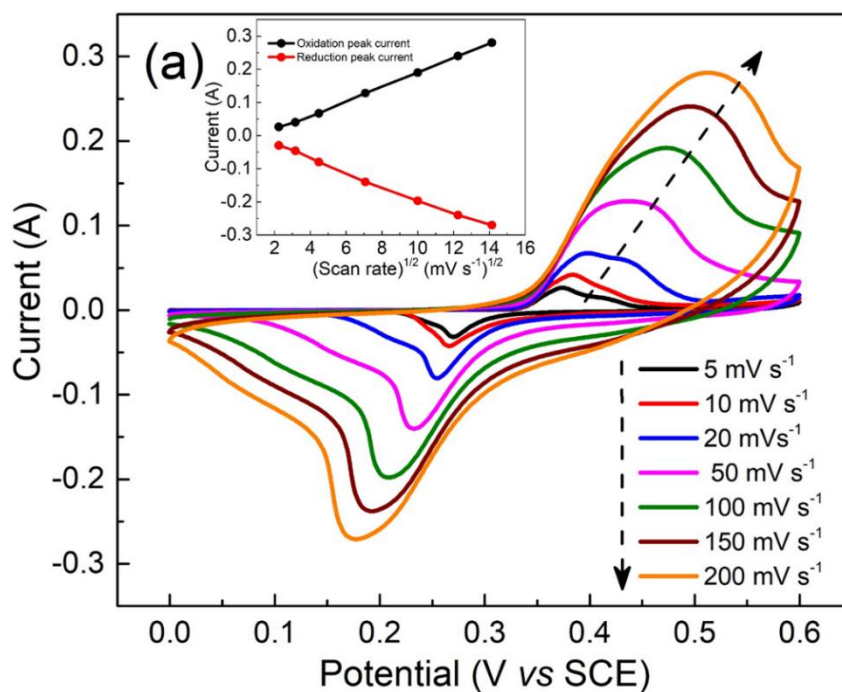
The microstructure of INWA is shown in Fig. 6.3(a-c). From the surface morphology of INWA as shown in Fig. 6.3(a), tilted nanowires with high density can be seen. Because the PETE template determines the microstructure of the electrodeposited INWA, according to the pore density of the PETE template, the INWA should have a high wire density of 3×10^8 wire cm^{-2} . Fig. 6.3(b) presents the cross-section morphology of INWA. The height of INWA is about 10 μm , which is consistent with the thickness of PETE template. The branched nickel nanowires interconnect with each other forming a stable self-supported structure, indicating that the INWA can be used as a 3D conductive scaffold. As shown in Fig. 6.3(c), it can be observed that the wire diameters are about 250 nm, and the wire spacing between the nanowires are less than 500 nm, which are much smaller than that of commonly used 3D conductive scaffolds, such as nickel foam, carbon cloths, and 3D graphene. Therefore, compared to the common conductive scaffolds used for SCs, the as-prepared INWA has a much higher surface area per volume to load active materials.

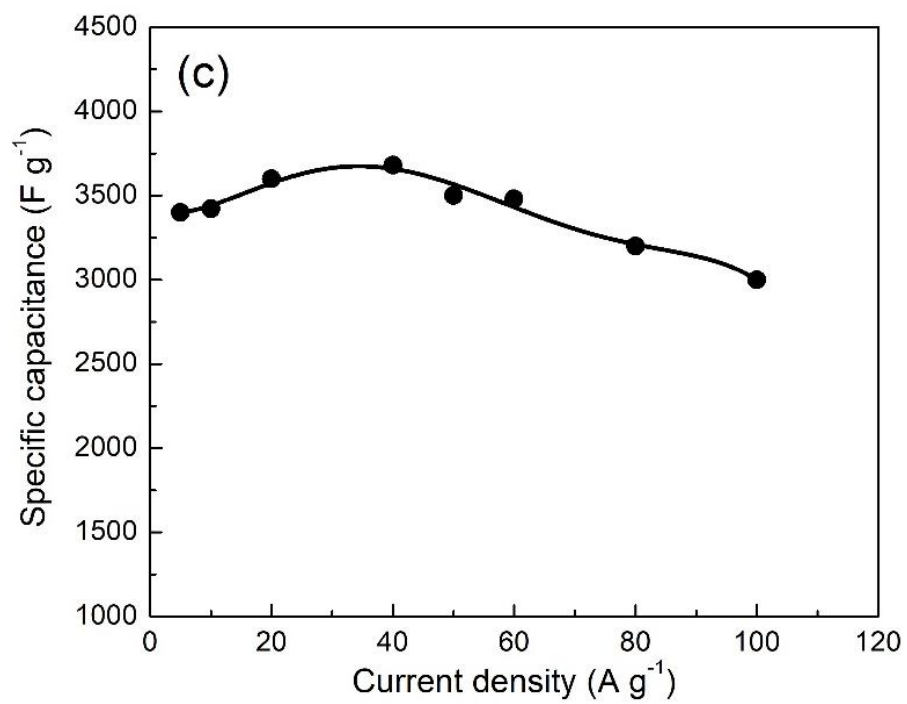
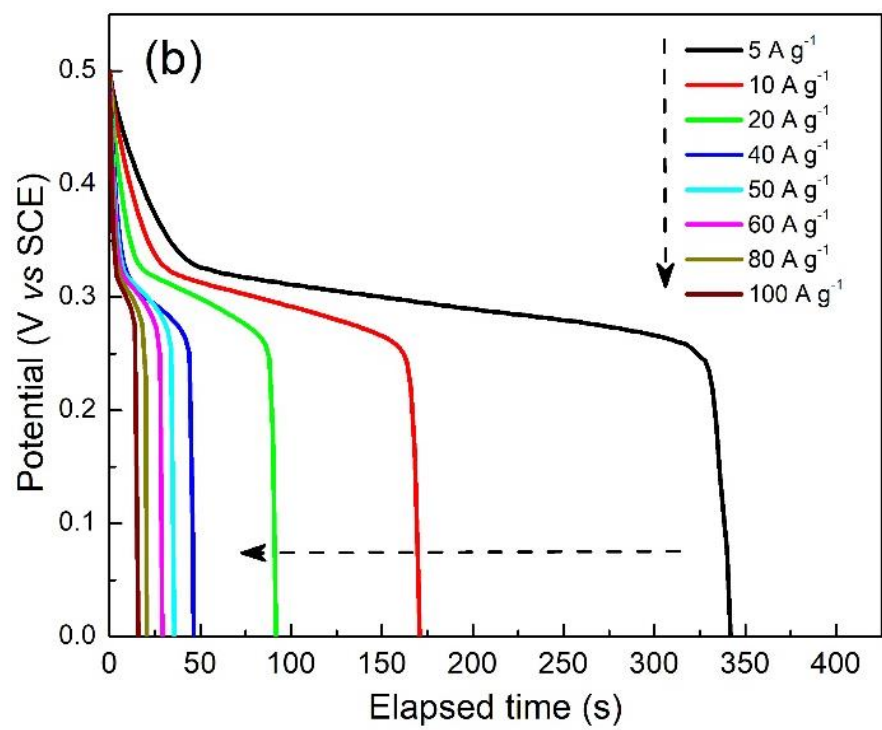
Fig. 6.3(d) shows the morphology of Ni(OH)₂@INWA. After oxidation treatment, significant change in morphology of nickel wire can be observed. Porous Ni(OH)₂ uniformly coats the entire surfaces of the nickel nanowires. Because of the direct conversion of the metallic surface of nickel nanowires, the Ni(OH)₂ is in stable contact with the metallic nickel of INWA, which results in a low charge transfer resistance. Also, owing to the surface conversion, the Ni(OH)₂ can have a high utilization for energy storage. Due to the self-supported structure of INWA, the Ni(OH)₂@INWA can be directly used as 3D electrode without using additional conductive scaffolds. The INWA of Ni(OH)₂@INWA serves as both a 3D conductive network and a core material to load Ni(OH)₂. Therefore, compared to the semiconducting core of the Ni(OH)₂ core-shell hybrid, the INWA has better electrical conductivity. Fig. 6.3(e) shows the TEM image of Ni(OH)₂@INWA. It can be seen that the edge of Ni(OH)₂@INWA exhibits foldaway silk-like morphology with a high degree of transparency, which indicates that the Ni(OH)₂ is composed of thin nanosheets, and demonstrates its porous structure. The Ni(OH)₂ with porous structure allows rich active sites to be exposed to the electrolyte, guaranteeing the efficient utilization of Ni(OH)₂ for energy storage. Fig. 6.3(f) shows a HRTEM image of Ni(OH)₂@INWA. The image displays a portion of amorphous phase without any lattice structure on the edge of Ni(OH)₂@INWA corresponding to amorphous Ni(OH)₂ (Xu et al., 2016). The corresponding selected-area electron diffraction (SAED) pattern in the inset shows a broad and diffused halo ring, suggesting that the Ni(OH)₂ is amorphous (Liu and Li, 2009; Su et al., 2014).

Fig. 6.4(a) exhibits the Ni 2p XPS spectrum of Ni(OH)₂@INWA. The two main peaks located at 855.7 and 873.3 eV correspond to Ni 2p_{3/2} and Ni 2p_{1/2}, respectively (Fu et al., 2018; Li et al., 2016). The binding energy difference of Ni 2p_{1/2} and Ni 2p_{3/2} is 17.6 eV, which is the characteristic of Ni(OH)₂ phase (Liu et al., 2017; Zhu et al., 2014). Therefore, the XPS result confirms the formation of Ni(OH)₂ produced by surface conversion on the nickel nanowire surface. The XRD patterns of INWA and Ni(OH)₂@INWA are shown in Fig. 6.4(b). The XRD pattern of INWA has three main peaks with strong intensities located at 44.80°, 52.75°, and 77.72°, which can be assigned to the (111), (200), and (220) Bragg's reflections of monoclinic Ni (JCPDS

04-850) (Guan et al., 2017; Shi et al., 2016). The XRD pattern of Ni(OH)₂@INWA only has the same three main peaks as that of INWA. Therefore, the XRD results further demonstrate that the Ni(OH)₂ is amorphous.

6.2 Electrochemical characterization





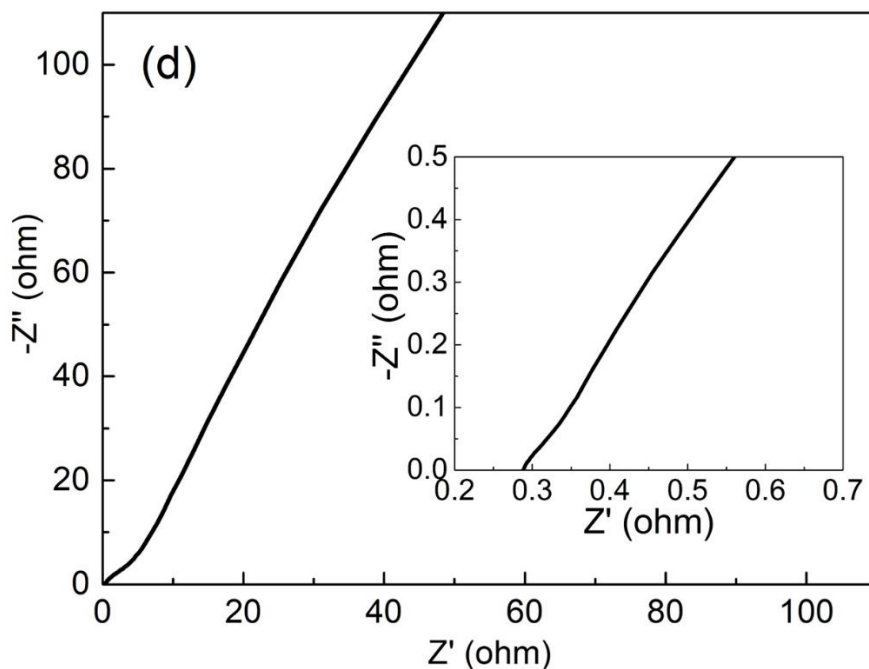
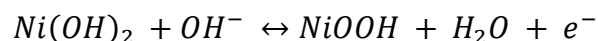


Fig. 6. 5 Electrochemical performance of Ni(OH)₂@INWA. (a) CV curves at different scan rates; (b) Discharge curves at different current densities; (c) Specific capacitance as a function of discharge current density; (d) EIS result measured in the frequency range of 10⁵-10⁻² Hz.

The electrochemical performance of Ni(OH)₂@INWA was evaluated using a three-electrode system. Fig. 6.5(a) shows the CV curves of Ni(OH)₂@INWA measured in the potential window of 0-0.6 V (vs SCE) at different scan rates from 5 to 200 mV s⁻¹. Each CV curve has a pair of strong redox peaks, which demonstrates that the capacitance primarily originates from the reversible Faradic redox reaction of Ni²⁺/Ni³⁺ in alkaline electrolyte (Ge et al., 2019):



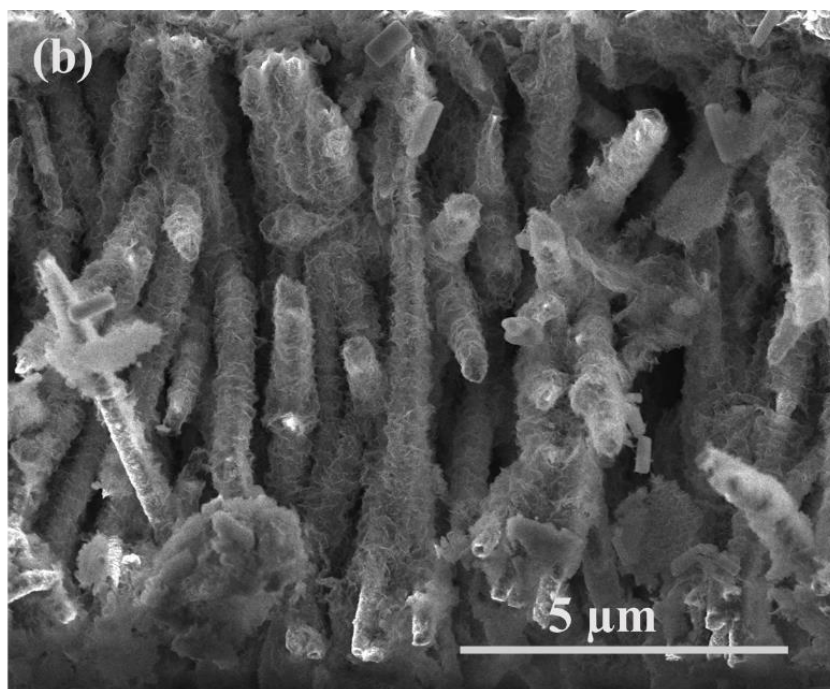
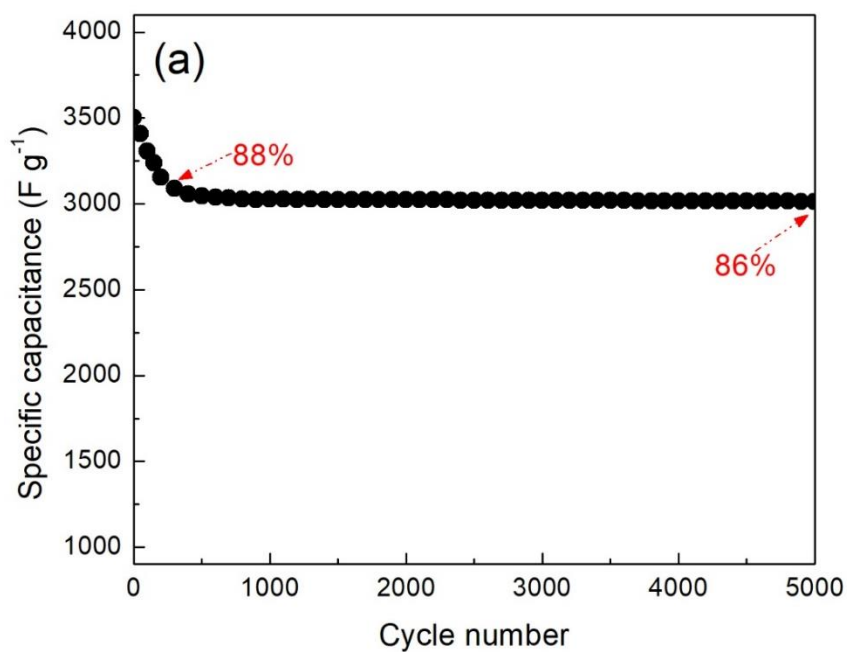
With the increase in scan rate, the oxidation peak shifts positively, and the reduction peak moves negatively, which is caused by the internal resistance of Ni(OH)₂@INWA. However, the peak currents increase linearly with the increase of square root of scan rate, indicating a high reversibility of the redox reactions.

The GCD results are shown in Fig. 6.5(b). Each discharge curve presents a plateau, which further demonstrates that the capacity mainly results from the Faradic redox reactions (Peng et al., 2017; Wang et al., 2013). Fig. 6.5(c) exhibits the results of the specific capacitance as a function of current density. The Ni(OH)₂@INWA

exhibits an ultrahigh specific capacitance of 3400 F g^{-1} at a current density of 5 A g^{-1} . With the increase in current density from 5 to 100 A g^{-1} , the specific capacitance first slowly increases to 3680 F g^{-1} , then gradually decreases to 3000 F g^{-1} (88 % retention of the initial specific capacitance), indicating an excellent rate capability at high current densities. The increase of the specific capacitance can be attributed to the activation process of Ni(OH)_2 . The ultrahigh specific capacitance of $\text{Ni(OH)}_2@INWA$ suggests the high utilization of amorphous Ni(OH)_2 . The excellent rate capability at high current densities demonstrates the excellent ionic/electronic conductivity of $\text{Ni(OH)}_2@INWA$.

EIS measurement was performed in the frequency range of 10^5 - 10^{-2} Hz, and the result is shown in Fig. 6.5(d). In general, the Nyquist plot of a supercapacitor electrode contains a semicircle in the high-middle frequency region and a straight line in the low frequency region (Zhang and Pan, 2015). The semicircle reflects the charge transfer resistance (R_{ct}) caused by the redox reactions and the double-layer capacitance. A smaller semicircle means a smaller charge transfer resistance (Wang et al., 2016). However, the Nyquist plot of $\text{Ni(OH)}_2@INWA$ exhibits almost a straight line in the entire frequency region. The absence of a semicircle on the EIS of $\text{Ni(OH)}_2@INWA$ suggests that the charge transfer resistance is extremely low. The extremely low charge transfer resistance can be attributed to the amorphous Ni(OH)_2 . The abundant structural defects in the amorphous Ni(OH)_2 can facilitate the diffusion of electrolyte ions and the Faradic reactions of active sites. The slope of the straight line in the low-frequency region corresponds to the Warburg impedance resistance (Z_w), which characterizes the ion diffusion resistance of the electrolyte (Du et al., 2018). The straight line of the $\text{Ni(OH)}_2@INWA$ with an angle larger than 60° to the real part (Z') suggests a low diffusion resistance. The low diffusion resistance of $\text{Ni(OH)}_2@INWA$ can be attributed to the porous structure of Ni(OH)_2 and the space between the nickel nanowires which provide short pathways for fast diffusion of electrolyte ions. The intercept at the real axis in high frequency is used to characterize the internal resistance (R_s) composed of electrolyte resistance, intrinsic resistance of the electrode active material, and the contact resistance between the active material and the current collector (Zhang et al., 2016). The R_s of

$\text{Ni(OH)}_2@INWA$ is as small as 0.29Ω , which indicates its good electronic conductivity. The good conductivity can be attributed to the nickel conductive network acting as core material and the stable contact between the nickel nanowire and the Ni(OH)_2 prepared by surface conversion.



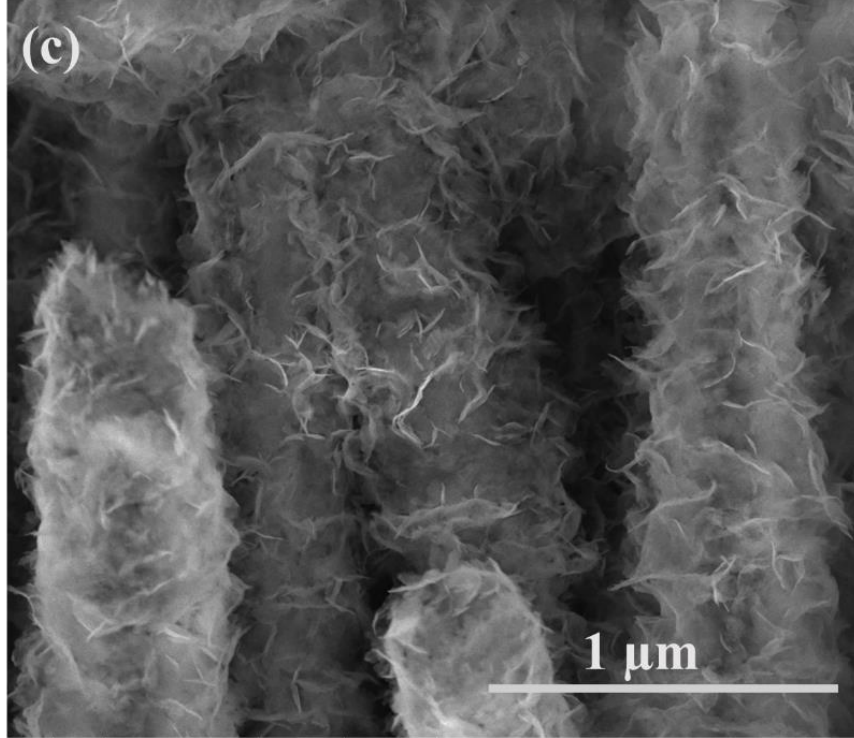


Fig. 6. 6 (a) Cyclic performance of Ni(OH)₂@INWA at a constant current density of 20 A g⁻¹; (b-c) SEM images of Ni(OH)₂@INWA after cycling test.

The cycling stability of Ni(OH)₂@INWA was investigated at a current density of 20 A g⁻¹ for 5000 cycles, and the corresponding result is shown in Fig. 6.6(a). In the first 400 cycles, the specific capacitance gradually decreases to 3050 F g⁻¹, which is 88 % of the initial specific capacitance of 3600 F g⁻¹. Then the specific capacitance slowly decreases to 86 % of the initial specific capacitance after 5000 cycles, indicating a remarkable long-term cycling stability at a high current density. After the cyclic stability test, the morphology of Ni(OH)₂@INWA is shown in Fig. 6.6(b-c). The Ni(OH)₂ nanosheets become larger and fill the space between the nanowires, but they still keep porous structure and good connection to the nanowire. The interspaces between the wires effectively avoid the overall volume expansion and structural damage of Ni(OH)₂@INWA.

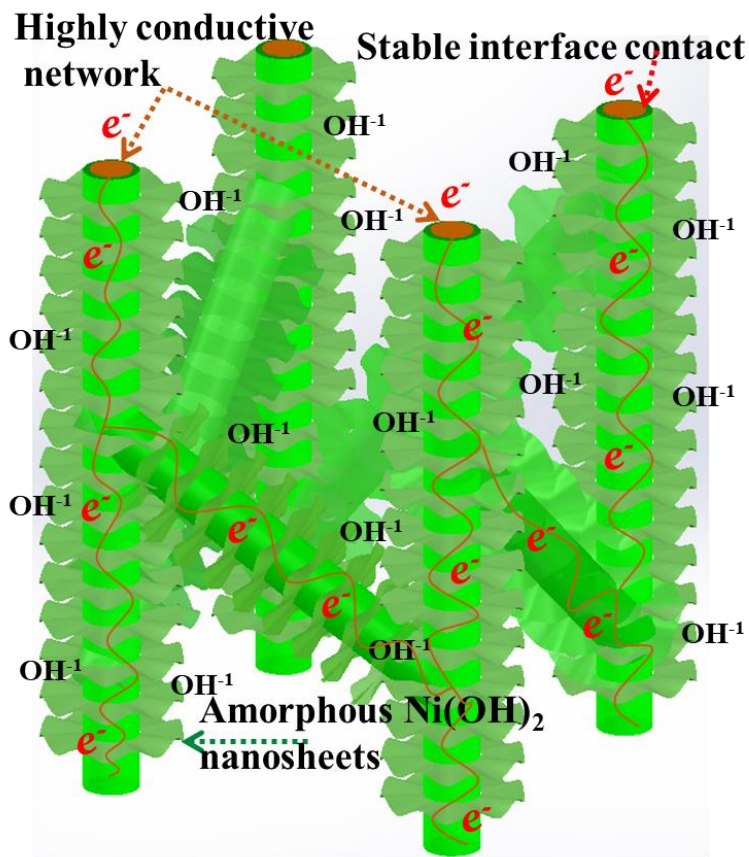
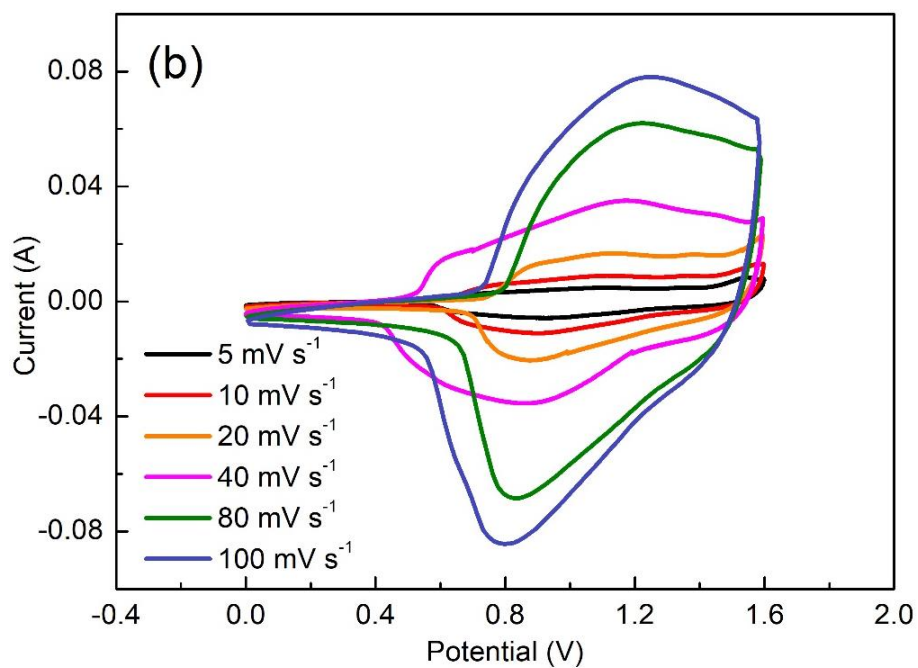
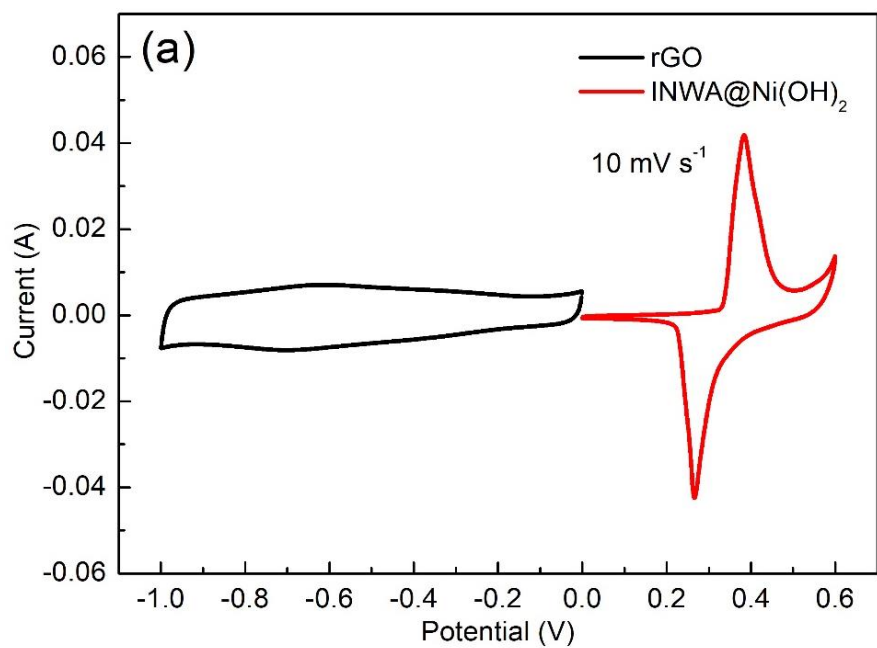
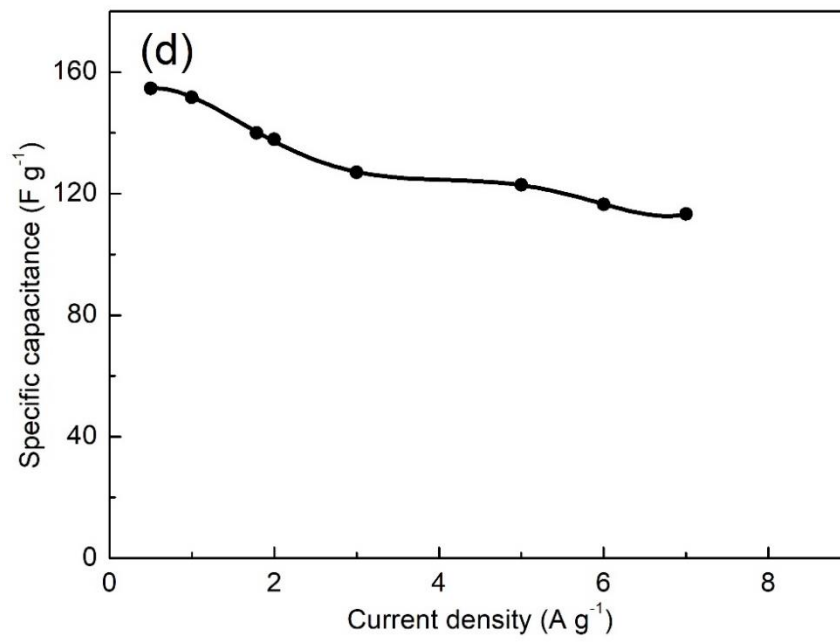
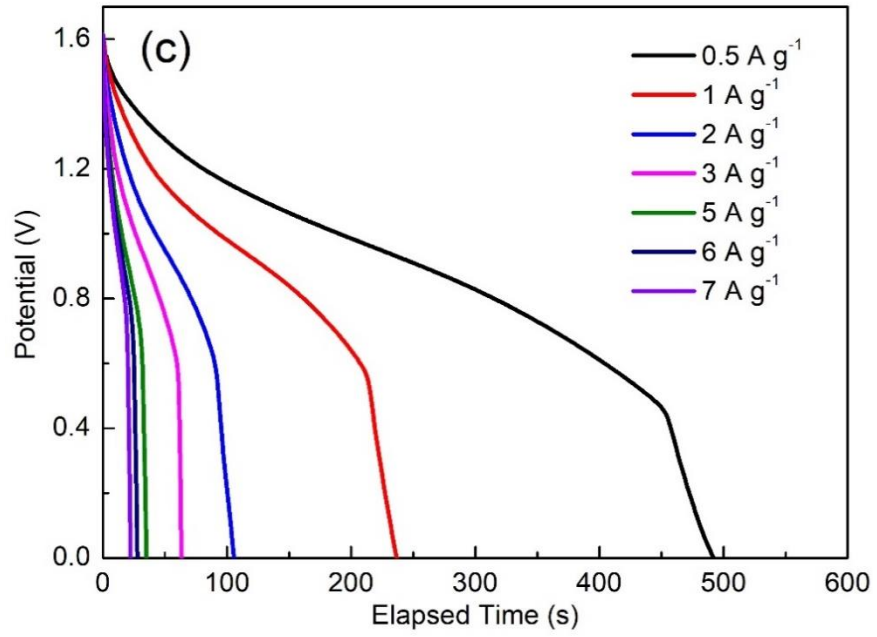
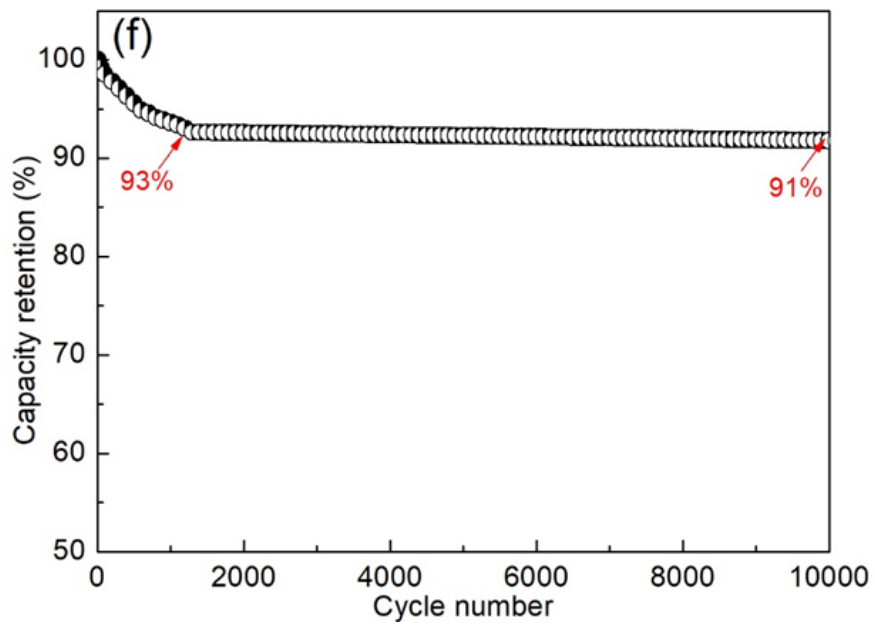
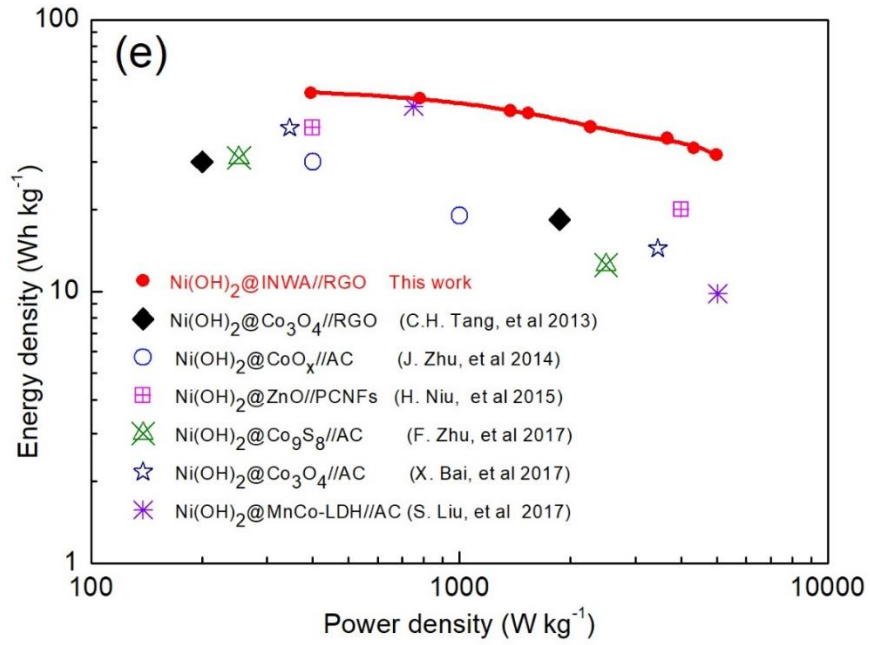


Fig. 6. 7 Schematic illustration of the material and structural advantages of Ni(OH)₂@INWA.

The electrochemical performance of supercapacitor electrode mainly depends on the active material and the electrode architecture. Fig. 6.7 schematically illustrates the material and structural advantages of Ni(OH)₂@INWA, which is closely related to the high specific capacitance, excellent rate capability and cycling stability. Firstly, the amorphous Ni(OH)₂ composed of nanosheets facilitates the process of faradic reaction and results in a high utilization. Secondly, the conversion of the nickel nanowire surface into am Finally, the INWA as conductive core offers large surface area to load the Ni(OH)₂ and provides efficient pathways to ensure high ionic/electronic conductivities at high current densities.







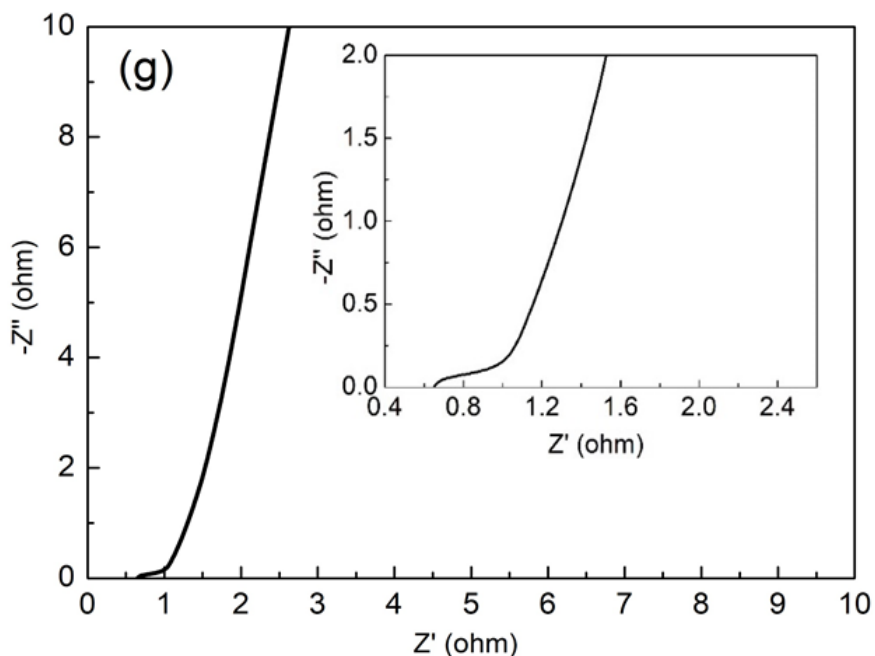


Fig. 6. 8 (a) CV curves of Ni(OH)₂@INWA and rGO electrodes. Electrochemical performance of Ni(OH)₂@INWA//rGO; (b) CV curves at different scan rates; (c) Discharge curves at different current densities; (d) Specific capacitance as a function of current density; (e) Ragone plot; (f) Cyclic stability at a current density of 2 A g⁻¹; (g) Nyquist plot.

To assess the potential application of Ni(OH)₂@INWA in supercapacitors, an ASC was fabricated using Ni(OH)₂@INWA and rGO as positive and negative electrodes, respectively, and a piece of polypropylene paper was used as a separator in a 6 M KOH solution. Fig. 6.8(a) presents the CV curves of positive and negative electrodes at a scan rate of 10 mV s⁻¹ in a three-electrode system. The rGO electrode can operate in a voltage window of -1.0-0 V, and the Ni(OH)₂@INWA electrode can work in a voltage window of 0-0.6 V. Therefore, the ASC can operate in the voltage window of 1.6 V. As shown in Fig. 6.8(b), the CV curves of Ni(OH)₂@INWA//rGO at scan rates from 10 to 100 mV s⁻¹ show the typical characteristic of electric double-layer capacitance and battery-type behavior in the potential range of 0-1.6 V without significant distortion of shape at high scan rates, indicating a high reversibility. Fig. 6.8(c) displays the GCD curves of Ni(OH)₂@INWA//rGO at different current densities in a voltage range of 0-1.6 V. The specific capacitances calculated from the discharge curves are shown in Fig. 6.8(d). Ni(OH)₂@INWA//rGO delivers specific capacitances of 154 151, 137 122,

and 113 F g^{-1} at current densities of 0.5, 1, 2, 5, and 7 A g^{-1} , respectively, suggesting excellent rate capability.

Energy and power densities are two crucial parameters for practical applications of SCs. The Ragone plot of $\text{Ni(OH)}_2@INWA/rGO$ is shown in Fig. 6.8(e). The energy density can reach to 53 Wh kg^{-1} at a power density of 395 W kg^{-1} , and an energy density of 31 Wh kg^{-1} can be maintained at a high power density of 4973 W kg^{-1} . These results are much better than other Ni(OH)_2 supercapacitors with core-shell structure reported recently, such as $\text{Ni(OH)}_2@Co_3O_4/rGO$ (30 Wh kg^{-1} at 200 W kg^{-1}) (Tang et al., 2013), $\text{Ni(OH)}_2@CoO_x/AC$ (30 Wh kg^{-1} at 400 W kg^{-1}) (Zhu et al., 2014), $\text{Ni(OH)}_2@ZnO/PCNFs$ (40 Wh kg^{-1} at 400 W kg^{-1}) (Niu et al., 2015), $\text{Ni(OH)}_2@Co_9S_8/AC$ (31 Wh kg^{-1} at 252 W kg^{-1}) (Zhu et al., 2017), $\text{Ni(OH)}_2@Co_3O_4/AC$ (40 Wh kg^{-1} at 346 W kg^{-1}) (Bai et al., 2017), $\text{Ni(OH)}_2@MnCo-LDH/AC$ (47.9 Wh kg^{-1} at 750 W kg^{-1} , 9.8 Wh kg^{-1} at 5020 W kg^{-1}) (Liu et al., 2017). Moreover, the $\text{Ni(OH)}_2@INWA/rGO$ exhibits excellent long-term stability, with 91 % retention of the initial capacitance after 10000 cycles at a current density of 2 A g^{-1} as shown in Fig. 8(f). The Nyquist plot of $\text{Ni(OH)}_2@INWA/rGO$ is shown in Fig. 6.8(g). The equivalent series resistance (R_s) is 0.53Ω , and the absence of semicircle on the plot demonstrates high electronic conductivity and electrochemical reactivity. These electrochemical performance shows that the $\text{Ni(OH)}_2@INWA$ has a great potential in practical applications for SCs.

6.3 Conclusions

In summary, an interconnected nickel nanowire arrays coated by amorphous Ni(OH)_2 with rational architecture has been successfully fabricated for supercapacitor applications. The $\text{Ni(OH)}_2@INWA$ can maintain self-supported structure without using additional 3D conductive scaffold, and has high electrical conductivity. The amorphous Ni(OH)_2 composed of nanosheets is in close contact with the INWA, and has porous structure. The $\text{Ni(OH)}_2@INWA$ shows enhanced electrochemical performance, in terms of ultrahigh specific capacitances of 3400 , 3000 F g^{-1} at current densities of 5, 100 A g^{-1} , respectively, indicating the high utilization and remarkable rate capability at high current densities, and long-term

cycling stability, because of the material and structural advantages. The asymmetric supercapacitor of Ni(OH)₂@INWA/rGO delivers a high energy density of 53 Wh kg⁻¹ at a power density of 395 W kg⁻¹, and an energy density of 31 Wh kg⁻¹ can be maintained at a high power density of 4973 W kg⁻¹. It also shows a long-term stability, with 91 % retention of the initial capacitance after 10000 cycles at a current density of 2 A g⁻¹. The excellent electrochemical performance suggests that the Ni(OH)₂@INWA has a great potential in practical supercapacitor applications.

References

- Bai, X., Liu, Q., Liu, J., Zhang, H., Li, Z., Jing, X., Liu, P., Wang, J., Li, R., 2017. Hierarchical Co₃O₄@Ni(OH)₂ core-shell nanosheet arrays for isolated all-solid state supercapacitor electrodes with superior electrochemical performance. *Chem. Eng. J.* 315, 35–45.
- Du, Q., Su, L., Hou, L., Sun, G., Feng, M., Yin, X., Ma, Z., Shao, G., Gao, W., 2018. Rationally designed ultrathin Ni-Al layered double hydroxide and graphene heterostructure for high-performance asymmetric supercapacitor. *J. Alloys Compd.* 740, 1051–1059.
- Fu, Y., Zhou, Y., Peng, Q., Yu, C., Wu, Z., Sun, J., Zhu, J., Wang, X., 2018. Hollow mesoporous carbon spheres wrapped by small-sized and ultrathin nickel hydroxide nanosheets for high-performance hybrid supercapacitors. *J. Power Sources* 402, 43–52.
- Ge, W., Peng, W., Encinas, A., Ruiz, M.F., Song, S., 2019. Preparation and characterization of flowerlike Al-doped Ni(OH)₂ for supercapacitor applications. *Chem. Phys.* 521.
- Guan, W., Tian, S., Cao, D., Chen, Y., Zhao, X., 2017. Electrooxidation of nickel-ammonia complexes and simultaneous electrodeposition recovery of nickel from practical nickel-electroplating rinse wastewater. *Electrochim. Acta* 246, 1230–1236.
- Li, S., Wen, J., Chen, T., Xiong, L., Wang, J., Fang, G., 2016. In situ synthesis of 3D CoS nanoflake/Ni(OH)₂ nanosheet nanocomposite structure as a candidate supercapacitor electrode. *Nanotechnology* 27.
- Liu, C., Li, Y., 2009. Synthesis and characterization of amorphous α -nickel hydroxide. *J. Alloys Compd.* 478, 415–418.
- Liu, S., Lee, S.C., Patil, U., Shackery, I., Kang, S., Zhang, K., Park, J.H., Chung, K.Y., Chan Jun, S., 2017. Hierarchical MnCo-layered double

- hydroxides@Ni(OH)₂ core-shell heterostructures as advanced electrodes for supercapacitors. *J. Mater. Chem. A* 5, 1043–1049.
- Niu, H., Zhou, D., Yang, X., Li, X., Wang, Q., Qu, F., 2015. Towards three-dimensional hierarchical ZnO nanofiber@Ni(OH)₂ nanoflake core-shell heterostructures for high-performance asymmetric supercapacitors. *J. Mater. Chem. A* 3, 18413–18421.
- Peng, W., Li, H., Song, S., 2017. Synthesis of Fluorinated Graphene/CoAl-Layered Double Hydroxide Composites as Electrode Materials for Supercapacitors. *ACS Appl. Mater. Interfaces* 9, 5204–5212.
- Shi, D., Zhang, L., Yin, X., Huang, T.J., Gong, H., 2016. A one step processed advanced interwoven architecture of Ni(OH)₂ and Cu nanosheets with ultrahigh supercapacitor performance. *J. Mater. Chem. A* 4, 12144–12151.
- Su, Y.Z., Xiao, K., Li, N., Liu, Z.Q., Qiao, S.Z., 2014. Amorphous Ni(OH)₂@three-dimensional Ni core-shell nanostructures for high capacitance pseudocapacitors and asymmetric supercapacitors. *J. Mater. Chem. A* 2, 13845–13853.
- Tang, C.H., Yin, X., Gong, H., 2013. Superior performance asymmetric supercapacitors based on a directly grown commercial mass 3D Co₃O₄@Ni(OH)₂ core-shell electrode. *ACS Appl. Mater. Interfaces* 5, 10574–10582.
- Wang, K., Zhang, Xialan, Zhang, Xinqi, Chen, D., Lin, Q., 2016. A novel Ni(OH)₂/graphene nanosheets electrode with high capacitance and excellent cycling stability for pseudocapacitors. *J. Power Sources* 333, 156–163.
- Wang, Y., Gai, S., Niu, N., He, F., Yang, P., 2013. Fabrication and electrochemical performance of 3D hierarchical β-Ni(OH)₂ hollow microspheres wrapped in reduced graphene oxide. *J. Mater. Chem. A* 1, 9083.
- Xu, S., Li, X., Yang, Z., Wang, T., Jiang, W., Yang, C., Wang, S., Hu, N., Wei, H., Zhang, Y., 2016. Nanofoaming to Boost the Electrochemical Performance of Ni@Ni(OH)₂ Nanowires for Ultrahigh Volumetric Supercapacitors. *ACS Appl. Mater. Interfaces* 8, 27868–27876.
- Zhang, L., Hui, K.N., Hui, K.S., Chen, X., Chen, R., Lee, H., 2016. Role of graphene on hierarchical flower-like NiAl layered double hydroxide-nickel foam-graphene as binder-free electrode for high-rate hybrid supercapacitor. *Int. J. Hydrogen Energy* 41, 9443–9453.
- Zhang, S., Pan, N., 2015. Supercapacitors performance evaluation. *Adv. Energy Mater.* 5, 1–19.

- Zhu, F., Yan, M., Liu, Y., Shen, H., Lei, Y., Shi, W., 2017. Hexagonal prism-like hierarchical $\text{Co}_9\text{S}_8@\text{Ni}(\text{OH})_2$ core-shell nanotubes on carbon fibers for high-performance asymmetric supercapacitors. *J. Mater. Chem. A* 5, 22782–22789.
- Zhu, J., Huang, L., Xiao, Y., Shen, L., Chen, Q., Shi, W., 2014. Hydrogenated CoOx nanowire@ $\text{Ni}(\text{OH})_2$ nanosheet core-shell nanostructures for high-performance asymmetric supercapacitors. *Nanoscale* 6, 6772–6781.

Chapter VII. Conclusions

- 1 Nanoporous metal with interconnected pore channels and pore diameter of a few hundred nanometers has been successfully fabricated with nitrocellulose membrane as template by a low cost method.
- 2 Upright self-supported nickel nanowire arrays and interconnected nickel nanowire array with small wire diameter and high wire density fabricated by template-directed electrodeposition are ideal conductive scaffolds and conductive cores for supercapacitor applications.
- 3 The amorphous $\text{Ni}(\text{OH})_2$ nanosheets converted from the metallic surface of nickel scaffold is in stable contact with the nickel scaffold surface, and have a high utilization of itself for energy storage.
- 4 Due to the amorphous $\text{Ni}(\text{OH})_2$ nanosheets, the excellent conductivity of nickel scaffold and the stable contact between $\text{Ni}(\text{OH})_2$ and nickel scaffold, the amorphous $\text{Ni}(\text{OH})_2$ on the scaffolds of NPN/USNWA/INWA show excellent electrochemical performance of ultrahigh specific capacitance, remarkable rate capability and high cycling stability.

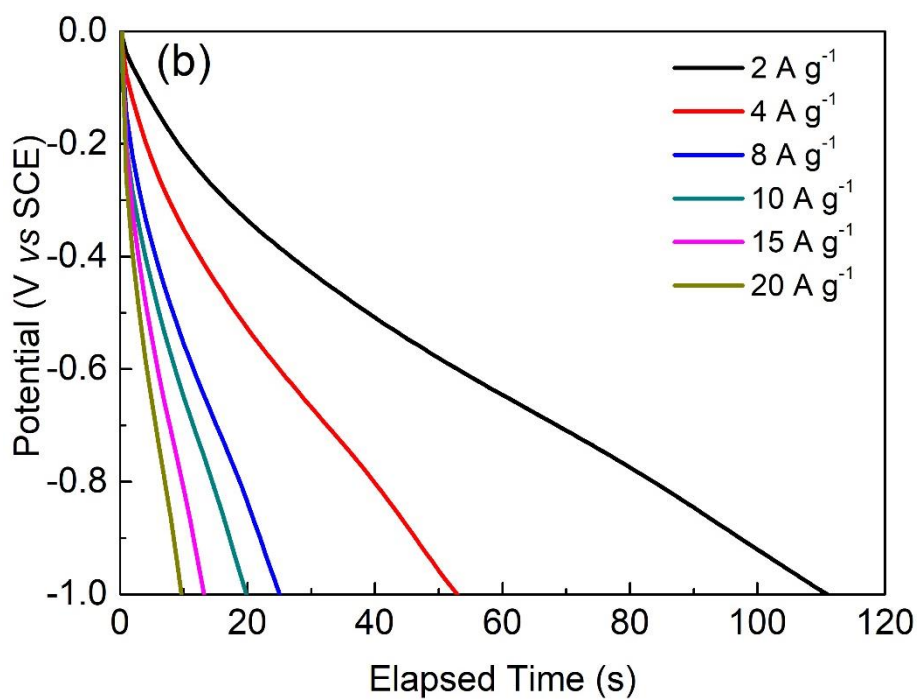
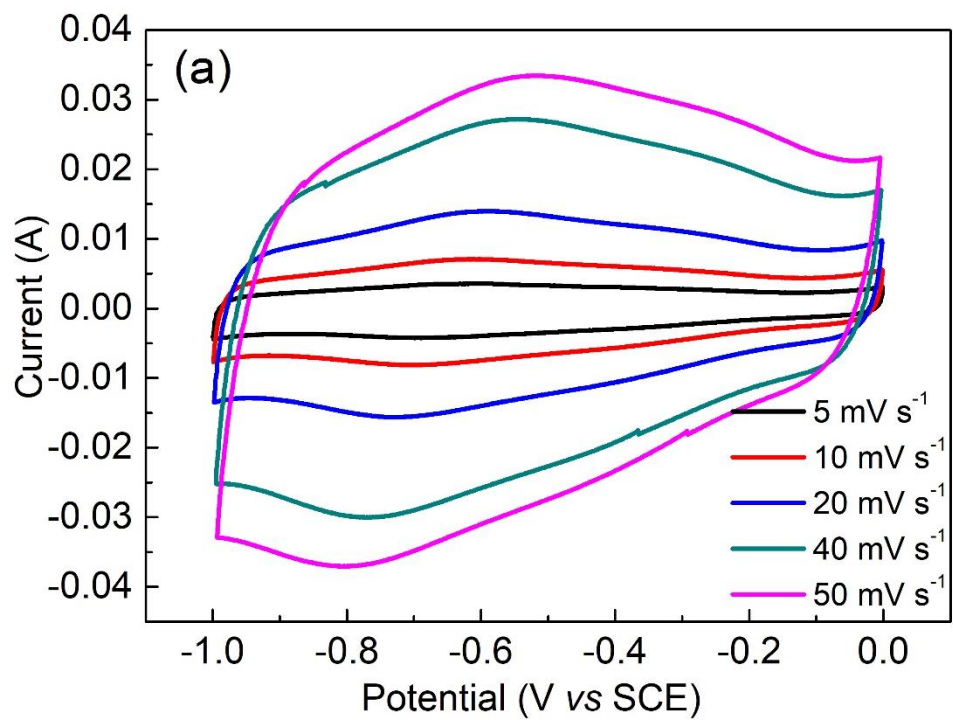
Appendix I

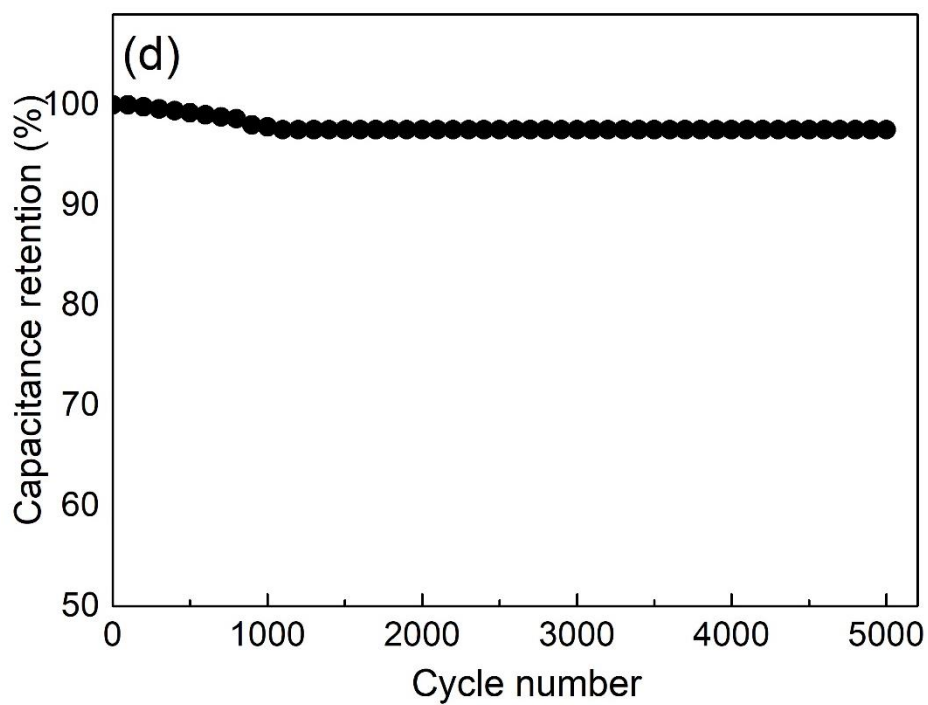
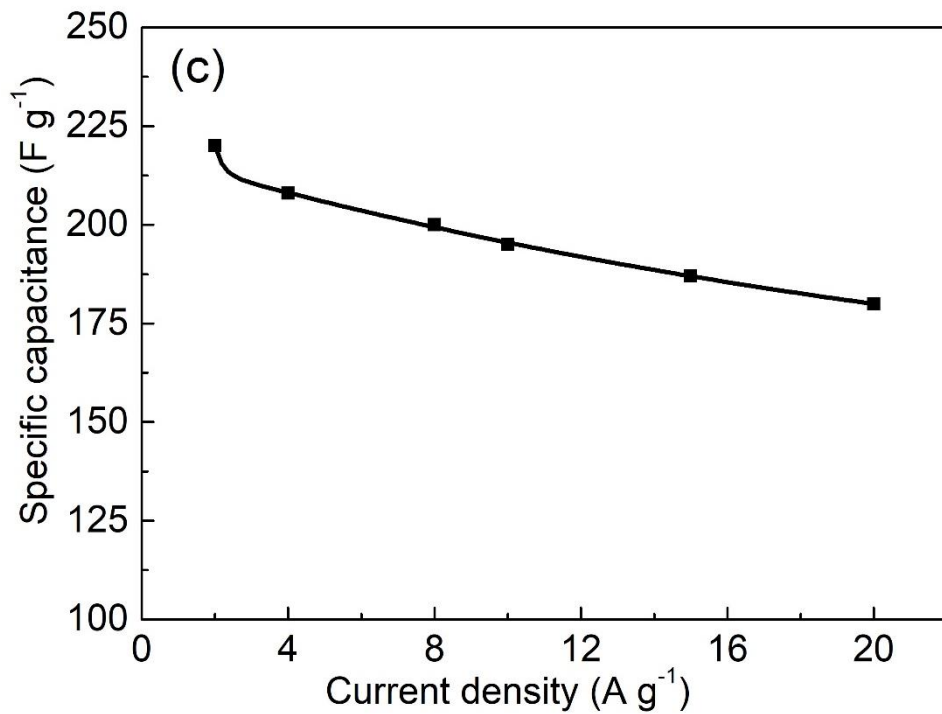
Articles published during the Ph.D study

- 1) **Ge, W.**, Encinas, A., Araujo, E., & Song, S. (2017). Magnetic matrices used in high gradient magnetic separation (HGMS): A review. *Results in physics*, 7, 4278-4286.
- 2) **Ge, W.**, Peng, W., Encinas, A., Ruiz, M. F., & Song, S. (2019). Preparation and characterization of flowerlike Al-doped Ni(OH)₂ for supercapacitor applications. *Chemical Physics*, 521, 55-60.

Appendix II

Experimental data of rGO





Electrochemical performance of rGO: (a) CV curves at different scan rates; (b) Discharge curves at different current densities; (c) Specific capacitance as a function of current density; (d) Cyclic stability test.